

Electronic Theses and Dissertations, 2020-

2020

Thin-film Lithium Niobate Integrated Photonics on Silicon for Electro- and Nonlinear-optic Applications

Amirmahdi Honardoost
University of Central Florida

 Part of the [Electrical and Electronics Commons](#)
Find similar works at: <https://stars.library.ucf.edu/etd2020>
University of Central Florida Libraries <http://library.ucf.edu>

This Doctoral Dissertation (Open Access) is brought to you for free and open access by STARS. It has been accepted for inclusion in Electronic Theses and Dissertations, 2020- by an authorized administrator of STARS. For more information, please contact STARS@ucf.edu.

STARS Citation

Honardoost, Amirmahdi, "Thin-film Lithium Niobate Integrated Photonics on Silicon for Electro- and Nonlinear-optic Applications" (2020). *Electronic Theses and Dissertations, 2020-*. 60.
<https://stars.library.ucf.edu/etd2020/60>

THIN-FILM LITHIUM NIOBATE INTEGRATED PHOTONICS ON SILICON FOR
ELECTRO- AND NONLINEAR-OPTIC APPLICATIONS

by

AMIRMAHDI HONARDOOST
M.S., University of Central Florida, 2016
B.S., Shahid Beheshti University, 2012

A dissertation submitted in partial fulfilment of the requirements
for the degree of Doctor of Philosophy in Electrical Engineering
in the Department of Electrical and Computer Engineering
in the College of Engineering and Computer Science
at the University of Central Florida
Orlando, Florida

Spring Term
2020

Major Professor: Sasan Fathpour

© 2020 Amirmahdi Honardoost

ABSTRACT

In order to overcome the drawbacks associated with conventional bulk lithium niobate photonic, thin-film lithium-niobate-on-silicon has been pursued recently. This work presents contributions made to electro-, and nonlinear-optic applications of this technology. For electrooptic applications, detailed modeling and design guidelines of optical and radio-frequency parameters of ultracompact modulators are developed and their accuracy in predicting the high-speed performance of such devices have been verified by comparison with experimental results. Novel design techniques and pathways for ultrahigh-speed (sub-terahertz) operation of such modulators, achieving up to 400 GHz modulation bandwidth, are also presented. For optical interconnect applications, novel structures for ultralow-power consumption modulators are designed and fabricated. Coherent modulation schemes, such as quadrature phase shift keying, is also pursued on the same thin-film platform for advanced optical communication systems. For nonlinear-optic applications, fabrication integrability of thin-film lithium niobate and chalcogenide glass waveguides on a single silicon chip for future directions, such as on-chip self-referenced optical frequency comb generation, is experimentally demonstrated. That is a pathway for both second- and third-order optical nonlinearity occurring on lithium niobate and chalcogenide, respectively, is designed and presented. An innovative and robust foundry-compatible back-end-of-line integration method is also proposed, in order to integrate thin-film lithium niobate devices with silicon or silicon-nitride photonic circuitry. Overall, this work extends the capabilities of the thin-film lithium niobate technology for novel electro- and nonlinear-optic applications. Finally, extensions of the aforementioned results suitable for future work are discussed.

Dedicated to my beloved parents, the greatest blessings in my life, who guided me to where I am today. Words are powerless to express how much I appreciate them.

ACKNOWLEDGMENTS

First and foremost, I would like to express my deepest gratitude to Prof. Sasan Fathpour, my dear Ph.D. advisor. It has been a privilege for me to have had the opportunity of joining his research group (Integrated Photonic Emerging Solutions, IPES), and being able to learn and grow under his amazing mentorship. I am forever grateful of his guidance, patience, trust, and tremendous support throughout my Ph.D. studies.

I want to thank my former colleagues at IPES, Dr. Jeff Chiles for introducing me into photonic simulation and fabrication world, Dr. Ashutosh Rao for patiently teaching me the ropes of it, Dr. Marcin Malinowski for always having time to respond to my theoretical questions, Dr. Saeed Khan for generously sharing his valuable knowledge and experience with me, Dr. Guillermo F. C. Gonzalez for our invaluable friendship and amazing time spent together in the lab, and Chih-Hao Li for our enjoyable conversations.

I also want to appreciate my current labmates, Tracy Sjaardema for our useful discussions and her support in maintenance of the cleanroom equipment, Kamal Abdelsalam for our long hours of fabrication, day and night, spent together in the cleanroom, and more recently, the younger generation of IPES members, Farzaneh A. Juneghani for helping me with the radio-frequency design and simulations, Ehsan Orduie for assisting me in the cleanroom fabrication, and Milad Gholipour for our fun time spent together in the lab.

I would like to express my appreciation for the support of Prof. Patrick L. LiKamWa, Dr. Ivan Divliansky, James D. Ross, and Nathan Aultman in the CREOL cleanrooms, and all of the CREOL, and ECE departments' administrative staff at UCF.

I am also grateful to my supportive Ph.D. committee members, Profs. Jiann S. Yuan, Reza Abdolvand, C. Kyle Renshaw, and Kyu Young Han.

My acknowledgments would be incomplete without thanking my amazing friends who supported me through the ups and downs of my life during Ph.D. studies, namely, Mahdi Kalayeh,

Amirtaha Taebi, Alireza Safaei, Farzad V. Farahani, Shahriar Talebi, Mahlagha Sedghi, Zahra Tavakkoli, Fatemeh Mehri, Seyedmohammad Mousavi, Amirhasan Fallah, Ahoo Eelhami, and many others.

Last but not least, I appreciate the endless support of my family from thousands of miles away - my beloved parents, to whom I owe everything, and my lovely little sister.

TABLE OF CONTENTS

LIST OF FIGURES	x
LIST OF TABLES	xxii
CHAPTER 1: INTRODUCTION	1
1.1 Background	1
1.2 Heterogeneous Thin-Film Lithium Niobate	1
1.3 Electrooptic Modulators	4
1.4 Pockel’s Effect	5
1.5 Modeling of Ultracompact Electrooptic Modulators	6
1.6 Ultrahigh-Bandwidth Electrooptic Modulators	7
1.7 Ultralow-Power Electrooptic Modulators	9
1.8 Coherent Modulation on Thin-Film Lithium Niobate Platform	10
1.9 Nonlinear Optical Properties	11
1.10 Cascaded Integration of Different Optical Nonlinearities on a Single Chip	11
1.11 Foundry-Compatible Integration of Thin-Film Lithium Niobate with Silicon Photonic	14
1.12 Conclusion and Future Work	15
1.13 References	16
CHAPTER 2: THIN-FILM LITHIUM NIOBATE PHOTONICS	19
2.1 Introduction	19
2.2 TFLN Platforms and Waveguides	23
2.2.1 Thin-Film Platforms	23
2.2.2 Ultracompact Waveguides	24
2.3 Electrooptic Modulators on TFLN	29

2.4	Nonlinear Optics on TFLN	37
2.4.1	Periodically-Poled TFLN Waveguides	38
2.4.2	Other Approaches to Phase Matching in TFLN Waveguides	43
2.4.3	Other Nonlinear Applications of TFLN Waveguides	46
2.5	Quantum Optics on TFLN	47
2.6	Roadmap Ahead	49
2.7	Concluding Remarks	51
2.8	References	52

CHAPTER 3: HIGH-SPEED MODELING OF ULTRACOMPACT ELECTROOPTIC MOD-

	ULATORS	73
3.1	Introduction	73
3.2	Electrical - Optical Modeling	77
3.3	RF Transmission Line Modeling	80
3.3.1	Characteristic Impedance	82
3.3.2	RF Attenuation Constant	86
3.4	Simulation Results and Discussions	87
3.5	Conclusions	95
3.6	Appendix	95
3.7	References	97

CHAPTER 4: TOWARDS SUBTERAHERTZ BANDWIDTH ULTRACOMPACT LITHIUM

	NIOBATE ELECTROOPTIC MODULATOR	104
4.1	Introduction	104
4.2	Design optimization	106
4.3	Final results and discussions	111
4.4	Conclusion	114

4.5	References	114
CHAPTER 5: CASCADED INTEGRATION OF OPTICAL WAVEGUIDES WITH THIRD- ORDER NONLINEARITY WITH LITHIUM NIOBATE WAVEGUIDES ON SILICON SUBSTRATES		
		117
5.1	Introduction	117
5.2	Design and Simulation	120
5.3	Fabrication	122
5.4	Characterization	123
	5.4.1 Linear Characterization	123
	5.4.2 Nonlinear Characterization	125
5.5	Conclusion	129
5.6	References	129
CHAPTER 6: FUTURE WORK AND PRELIMINARY RESULTS		
		134
6.1	Ultralow-Power Thin-Film Lithium Niobate Electrooptic Modulators	134
6.2	Coherent Modulation in Thin-Film Lithium Niobate Electrooptic Modulators . . .	138
6.3	Cascaded Second-, and Third-Order Optical Nonlinearities on a Single Chip	140
6.4	Foundry-Compatible Integration of Thin-Film Lithium Niobate with Silicon Pho- tonics	143
6.5	Summary	148
6.6	References	149
APPENDIX A: COPYRIGHT PERMISSIONS		
		150

LIST OF FIGURES

Figure 1.1: Summary of unique material properties of LN and their corresponding applications [1]. This dissertation focuses on the main photonic applications of LN through exploiting its strong EO effect and large second-order optical nonlinearity.	2
Figure 1.2: Fabrication steps of TFLN on Si wafers [1, 6]. (a) Initial bulk LN wafer; (b) Ion implantation (the red-dashedline shows the defected region at the desired depth of final thin-film thickness); (c) Bonding onto a Si handling wafer (or other wafers such as LN or quartz) with a low-index insulating layer (typically SiO ₂); (d) Thermal cycling process to exfoliate the thin film from the LN crystal at the defected layer and the final TFLN on Si product. The remaining bulk LN crystal can be recycled. For simplicity, other steps such as thermal annealing for preserving the material properties of LN, and mechanical polishing for smoothening of the surface roughness are not depicted here.	3
Figure 1.3: Comparison between (a) Conventional; (b) Compact, LN waveguide [1]. The waveguides cross-sections are drawn to scale to emphasize the significant reduction in optical mode size. This about two orders of magnitude reduction facilitates large-scale integration of photonic integrated circuits, as well as boosted performance for LN devices, as discussed in Chapter 2.	4
Figure 1.4: Modeling of RF and optical properties of ultracompact EOMs, as discussed in Chapter 3 [7].	7
Figure 1.5: Design and optimization of ultracompact EOMs for ultrahigh-BW (sub-THz applications) [14].	8

Figure 1.6: (a) Typical structure for the TFLN MZ EOM; (b) Proposed design for the ultralow-power EOMs. Lower gap between the electrodes can directly reduce the switching voltage of MZ EOMs, as discussed in Chapter 6; (c) Image of the fabricated chip; Microimages for two types of devices, designed for high-, and low-frequency operation, are given in (d), and (e), respectively.	9
Figure 1.7: (a) Image of the fabricated chip; (b) Microimage of the TFLN QPSK EOMs.	10
Figure 1.8: Examples of nonlinear optical processes: (a) Second-Harmonic generation (SHG); (b) Supercontinuum generation (SCG).	12
Figure 1.9: Demonstration of monolithic integration of waveguides with $\chi^{(2)}$ and $\chi^{(3)}$ optical nonlinearity on a single Si chip [17]. The inset is an SEM image of the fabricated waveguide's cross-section denoted by 'b' on the schematic.	13
Figure 1.10 The schematic depicts the proposed scheme for back-end-of-line integration of TFLN devices with Si photonics. Details are discussed in Chapter 6.	14
Figure 1.11 Summary of the fabrication steps for the proposed scheme. Details are discussed in Chapter 6.	15

Figure 2.1: (a) Summary of unique material properties of LN [1]–[7], [23]–[26]. This review focuses on the main photonic applications of LN through exploiting its strong EO effect and large second-order optical nonlinearity; (b) Crystalline structure of LN in ferroelectric phase. The red dashed-box represents its unit cell. The horizontal blue lines depict the oxygen (O) layers and the position of lithium (Li) and niobium (Nb) atoms are shown with respect to it (after [2, 27]). The position of the atoms are shown before and after the poling process, as discussed in Section 2.4.1; (c) Comparison between the traditional bulk versus thin-film LN waveguides. The figures for the waveguides cross-sections are drawn to scale to emphasize the significant reduction in optical mode size. This about two orders of magnitude reduction facilitates large-scale integration of photonic integrated circuits, as well as boosted performance for LN devices, e.g., reduced $V_{\pi} \cdot L$ for TFLN EOMs and increased mode overlap and efficiency for PPLN waveguides. The steps for fabrication of TFLN wafers on Si are presented in Figure 2.2. 21

Figure 2.2: Summary of the steps for fabrication of TFLN on Si wafers [28]. (a) Initial bulk LN wafer; (b) Ion implantation (the red-dashed line shows the defected region at the desired depth of final thin-film thickness); (c) Bonding onto a Si handling wafer (or other wafers such as LN or quartz) with a low-index insulating layer (typically SiO_2); (d) Thermal cycling process to exfoliate the thin film from the LN crystal at the defected layer and the final TFLN on Si product. The remaining bulk LN crystal can be recycled. For simplicity, other steps such as thermal annealing for preserving the material properties of LN, and mechanical polishing for smoothening of the surface roughness are not depicted here. 24

Figure 2.3: Common waveguide structures for TFLN-on-Si devices: (a) Rib-loaded, (b) dry-etched, (c) proton-exchanged or Ti-diffused, and (d) SOI-bonded structures; These methods can also be applied to TFLN on LN or quartz substrates. The majority of recent work demonstrating high-performance TFLN EOMs are utilizing rib-loaded (Figure 2.3a) [66], dry-etched (Figure 2.3b) [70, 73], and SOI-bonded (Figure 2.3d) [71, 72, 74, 78] methods, while for nonlinear devices, rib-loaded [90, 91] and dry-etched [92, 95] have been the most commonly employed platforms. In comparison to platforms (a)-(c), platform (d) requires additional bonding and TFLN substrate removal steps. The microimages for (e) rib-loaded, (f) dry-etched, (g) proton-exchanged, and (d) SOI-bonded waveguides, are reproduced with permission from [91], [45], [50], and [74], respectively. 25

Figure 2.4: Fabrication steps for bonded-SOI TFLN platform [71, 72, 74, 117]: (a) Patterned SOI structure; (b) TFLN (see Figure 2.2d) bonding onto the SOI wafer using SiO₂ or BCB; (c) TFLN substrate removal; (d) Prepared structure and associated optical mode simulation. At this step, metallic electrodes can be deposited on top in order to form LN photonic devices such as EOM and PPLN waveguides. 27

Figure 2.5: A novel approach for heterogeneous integration of TFLN with SOI waveguides is shown. The SiN intermediate layer serves as the adiabatic mode converter from SOI to the LN region (from AA' to BB'), as well as the rib for the hybrid SiN-LN waveguide. The optical mode simulation at different cross-sections of the structure are shown on the right. The SiN width can be optimized for achieving the desired optical mode confinement in TFLN [117]. 29

Figure 2.6: The timeline presents recent progress in TFLN EOMs in terms of key performance parameters, namely, LN waveguide propagation loss, 3-dB modulation BW, ER, and $V_{\pi} \cdot L$ at low frequencies. Q denotes the quality factor of TFLN microrings. The figure represents significant achievements in TFLN EOM technology and is not all-inclusive. 30

Figure 2.7: Comparison between conventional bulk LN versus ultracompact TFLN MZ EOMs. The 3-D schematics are drawn to scale, in order to emphasize the significant reduction in the device footprint. The 2-D device cross-sections are not in scale. By utilizing the highly-compact optical mode in the TFLN case, the gap between the metallic electrodes can be decreased without inducing additional optical loss which results in lower $V_{\pi} \cdot L$ values compared to its bulk counterpart. 30

Figure 2.8: Examples of recent high-performance TFLN MZ EOMs on Si [66, 70, 71, 74]: (a) 18-dB ER, and 33-GHz BW. Reproduced with permission from [66]; (b) 30-dB ER, and 100-GHz BW. Reproduced with permission from [70]; (c) 20-dB ER, and 106-GHz BW. Reproduced with permission from [71]; (d) 40-dB ER, and 70-GHz BW. Reproduced with permission from [74]. L is the modulation length. Values for V_{π} , and ER are reported at low frequencies. 32

Figure 2.9: Examples of recently-demonstrated TFLN resonance-based EOMs [62, 65, 69, 76]: (a) BCB-bonded LN-SOI microring. Reproduced with permission from [62]; (b) Rib-loaded LN-on-Si microring. Reproduced with permission from [65]; (c) Dry-etched LN-on-LN microring. The racetrack resonator exhibits 3-dB BW of 30 GHz. Reproduced with permission from [69]; (d) Rib-loaded LN-on-quartz microring. Reproduced with permission from [76]. 36

Figure 2.10 Examples of recently-demonstrated TF-PPLN waveguides [90, 91, 92, 95]:

(a) Rib-loaded TF-PPLN with nonlinear conversion efficiency of 8% for pulsed input. Reproduced with permission from [90]; (b) Rib-loaded TF-PPLN. Reproduced with permission from [91]; (c) Dry-etched TF-PPLN. Reproduced with permission from [92]; (d) Dry-etched TF-PPLN. Reproduced with permission from [95]. η is the reported normalized conversion efficiency. L denotes the length of the poled region. 39

Figure 2.11 Demonstration of efficient SHG in PPLN microring resonators: (a) SHG signal (red), when TE-polarized pump laser is swept across the telecom band (blue); (b) False color SEM images of the etched device in hydrofluoric acid. Reproduced with permission from [97]. 40

Figure 2.12 Periodic poling of TFLN waveguides: (a) Example of poling pulse for TF-PPLN along with (b) piezoresponse force microscope image of the resulting periodic domain. Reproduced with permission from [133]; (c) Schematic illustration of the evolution of inverted domain using a long poling pulse and multi-pulse waveforms with short pulse durations. Images of the device are obtained after ion milling to visualize the periodically poled region. Reproduced with permission from [91]; Actively-monitored poling technique demonstrates increase of SHG efficiency with (d) the number of poling pulses and (e) the number of poling cycles, used for ferroelectric domain inversion (see Figure 2.1b). Reproduced with permission from [95]. 41

Figure 2.13	Demonstration of poling-free methods [138, 140, 139] for SHG in TFLN platform: (a) 3-D schematic of a rib-loaded GA-QPM waveguide with a sinusoidal modulation of the width along with the optical mode profiles of the fundamental and second-harmonic TE modes at a grating width of 1095 nm. Reproduced with permission from [138]; (b) 3-D schematic of a random QPM waveguide on a dry-etched TFLN platform along with a micrograph of the fabricated device. Reproduced with permission from [140].; (c) Optical mode profiles of the first- and third-order TE modes at the pump and second-harmonic wavelengths for MPM; (d) SEM image of the fabricated GA-QPM structure. (c) and (d) are reproduced with permission from [139].	45
Figure 2.14	Examples of photon-pair generation demonstrated in TFLN platform: (a) Wide-band (up to 400 nm) SPDC spectrum. Reproduced with permission from [143]; (b) CAR values of up to 7000 with more than 120-nm signal-idler channel separation. Reproduced with permission from [103]; (c) CAR values > 67000 at 82 kHz pair generation rate. Reproduced with permission from [105].	48
Figure 3.1:	(a) Conventional LN waveguide; (b) Compact thin-film LN waveguide. . . .	75
Figure 3.2:	Two dimensional schematic of a typical thin-film LN MZ EO modulator. . . .	77
Figure 3.3:	Schematic of a general transmission line model. V_s is the source voltage with the impedance Z_S . The transmission line is terminated with a load with impedance Z_L . Z_0 and γ are characteristic impedance and complex propagation constant of the transmission line, respectively. The transmission line is along the x -axis.	80

Figure 3.4: Comparison between the calculated real part, and imaginary part of the characteristic impedance (Z_0) of the example electrooptic modulator (EOM) using conformal mapping (CM) and COMSOLTM simulations vs. the conventional bulk modulator for the operating frequency range. 85

Figure 3.5: Calculated RF refractive index (n_{RF}) of the example modulator using conformal mapping and COMSOLTM simulations, and α_c , α_d , and α_{RF} by using conformal mapping method. 88

Figure 3.6: (a) Simulated RF mode profile of MZ modulator with 5.5 μm gap between the electrodes at 10 GHz.; (b) Simulated optical mode profile of the hybrid ridge waveguide with Si_3N_4 rib. 89

Figure 3.7: Calculated effective refractive indices of optical waveguide of the modulator for 3 different rib-loading materials as examples. The height and width of the rib is varied. The thin-film LN thickness is 400 nm. The inset table shows the assumed refractive indices of rib-loading materials. 90

Figure 3.8: (a) Variation of the normalized frequency dependent response of the EO modulator for different values of effective optical refractive index, n_{op}^{eff} .; (b) Simulated optical loss vs. the gap between the electrodes (W_g) for 3 different rib-loading materials as an example.; (c) Characteristic impedance (Z_0) vs. the gap between the electrodes (W_g) for different values of the center electrode's width (W_c). 92

Figure 3.9: (a) Comparison between the experimental data [17] vs. the performance prediction from the developed (see Eq. (3.20)) as well as the conventional model [43].; (b) Variation of the simulated frequency response, and half-wave voltage (V_π) of the modulators for different lengths of RF electrodes vs. the RF frequency. 94

Figure 4.1: (a) 3-D schematic of the thin-film LN MZ EOMs; (b) Cross-section of the EOMs in the lateral y - z plane. The zoomed section shows the misalignment ($\Delta D = D_2 - D_1$) of the rib's center (D_1) from the middle of the gap between the electrodes (D_2).	106
Figure 4.2: RF design considerations (all performed at 100 GHz for $w_l = 12.0 \mu\text{m}$ ($w_c = 8.0 \mu\text{m}$ for (a), (c), and (e))): Variation of (a) RF loss vs. w_g for different values of t_2 ; (b) RF loss vs. w_c for different values of w_g and t_2 ; (c) n_{RF} vs. w_g for different values of t_2 ; (d) n_{RF} vs. w_c for different values of w_g and t_2 ; (e) Z_0 vs. t_2 for different values of w_g and w_c ; and (f) Z_0 vs. w_c for different values of w_g	108
Figure 4.3: Simulated RF mode profile for (a) rib-loaded and (b) all-LN EOMs with identical dimensions. Arrows are proportional to the magnitude of the field. Identical plot settings have been employed for COMSOL TM plots in both cases. Simulated TE optical mode profile for (c) rib-loaded and (d) all-LN waveguides with the same $w_{rib} = 1.3 \mu\text{m}$, $t_{rib} = 0.5 \mu\text{m}$, and a $1\text{-}\mu\text{m}$ -thick top cladding SiO_2 layer.	109
Figure 4.4: Γ for (a) rib-loaded; (b) all-LN EOMs; $V_\pi \cdot L$ for (c) rib-loaded; (d) all-LN EOMs, vs. ΔD (see Fig. 4.1(b)).	110
Figure 4.5: Metal-induced optical propagation loss vs. ΔD (see Fig. 4.1(b)) for $D_2 = 7.5 \mu\text{m}$	111
Figure 4.6: (a) n_{RF} ; (b) Z_0 and RF loss; (c) EO response (S_{21}) of the EOMs for different lengths. The horizontal dashed line shows the 3-dB electrical BW, and the inset depicts Δn	113

Figure 5.1: (a) Schematic of the integrated ChG-LN as well as the reference waveguides. Simulated optical mode profiles of the structure are also shown for fundamental TE input at 1550 nm for different cross-sections. Adiabatic mode transition is shown in the inset. (b) A cross-section SEM image of the fabricated devices at position b of the taper. 120

Figure 5.2: Simulated coupling efficiency of the mode-converting tapers vs. (a) Length of the taper; (b) Wavelength; (c) Width of the taper’s tip; and (d) Misalignment between the centers of the ChG waveguide/taper and Si₃N₄-LN waveguide. . 122

Figure 5.3: (a) Optical spectra of output power (10 dBm input power) for the integrated as well as the reference waveguides for both TE and TM input polarizations in the 1550-1560 nm wavelength range; (b) Output power difference between the integrated and reference waveguides for TE and TM input polarizations for the same wavelength range. 124

Figure 5.4: Schematic of the experimental setup for wavelength conversion via FWM. PC: Polarization Controller, EDFA: Erbium-doped fiber amplifier, OSA: Optical spectrum analyzer. 125

Figure 5.5: Measured output spectrum from the integrated ChG-LN waveguides from the OSA at a resolution of 0.02 nm. 126

Figure 5.6: Measured peak power of FWM#1 signal vs. Pump#1 power. The result is also compared with the data obtained from simulation. 128

Figure 6.1: (a) Standard TFLN MZ EOM structure; (b) Proposed novel structure for ultralow-power TFLN MZ EOMs. 135

Figure 6.2: (a) Standard TFLN MZ EOM structure; (b) Proposed novel structure for ultralow-power TFLN MZ EOMs. The optical mode is TE polarized. 136

Figure 6.3: (a) Image of the fabricated chip; Microimages of the devices for (b) low-, and (c) high-frequency operation. The high-frequency design posses narrower middle electrode.	137
Figure 6.4: (a) Experimental setup for low-, and high-frequency measurements.	138
Figure 6.5: Operation principle of a QPSK modulator and its schematic diagram.	139
Figure 6.6: Experimental setup and preliminary measurement results.	140
Figure 6.7: (a) Quasi-TE optical mode transition from ChG waveguides (left) to TFLN waveguides (right) through carefully designed mode-converting tapers; (b) Fundamental optical mode distribution in ChG waveguide for SCG; (c) 3-D schematic of the fully-integrated chip; (d) Simulation results for adiabatic mode transition for tapers with length above $100 \mu\text{ m}$; (e) Fundamental optical mode distribution in TFLN waveguide (rib-loaded with SiN) for SHG. Reproduced with permission from [3].	141
Figure 6.8: Image of the fabricated chip.	142
Figure 6.9: Conceptual 3-D schematic of a fully-integrated chip for frequency-stabilized optical comb generation application. [4]	142
Figure 6.10(a) Schematic of the proposed structure for thin-film integration. As presented in (a), a host of different materials can be used in this approach; (b) An example of designed dimension for TFLN integration with standard Si photonic waveguides. [5]	143
Figure 6.11 3-D schematic of a conceptual fully-integrated TFLN EOM with Si photonic circuitry including on-chip laser source and detection components. The simulated optical mode is provided at different positions of the circuit. An adiabatic mode transition from Si waveguide (left) to TFLN region (right) is shown as well. [5]	144
Figure 6.12 Summary of the fabrication steps using TFLN-on-Si wafers [5]	145

Figure 6.13 Summary of the fabrication steps using TFLN-on-LN (LNOI) wafers [5] . . . 146

Figure 6.14 Summary of the fabrication steps using TFLN-on-Si wafers and BCB bonding [5] 147

LIST OF TABLES

Table 2.1: State of the art in propagation loss for various TFLN platforms of Figure 2.3.	29
Table 2.2: Summary of performance parameters for TFLN MZ EOMs. BW denotes the 3-dB electrical modulation BW. $V_{\pi} \cdot L$, and ER are at reported values at low frequencies. The values inside the parenthesis represent the reported measurements for another device in the same work.	35
Table 2.3: Summary of performance parameters for TFLN resonance-based EOMs. R and BW denote the radius, and 3-dB electrical modulation BW, respectively. The values for ER are at low frequencies.	37
Table 2.4: Examples of recently-demonstrated TF-PPLN devices. η and L represent the normalized conversion efficiency, and the length of the poled region, respectively. CAR denotes the coincidence-to-accidental ratio measurements for on-chip photon-pair generation.	42
Table 4.1: Values of the geometrical dimensions in Fig. 1(b) for the optimized EOMs.	112
Table 4.2: Comparison between rib-loaded and all-LN design for a fixed drive voltage.	114
Table 6.1: Simulated results of Γ and $V_{\pi} \cdot L$ for the structure of Figs. 6.1 and 6.2.	135
Table 6.2: Simulated results of metallic-induce optical absorption for the structure of Figs. 6.1 and 6.2.	137

CHAPTER 1: INTRODUCTION

1.1 Background

Lithium niobate (LiNbO_3 , LN) is one of the most widely used materials in integrated photonics for electrooptic (EO) and nonlinear optical applications. Transparency in a broad range of the electromagnetic spectrum (0.4-5 μm), strong second-order optical nonlinearity, as well as a large EO coefficient make LN an ideal material for integration with silicon (Si) photonics for applications such as second-harmonic generation (SHG), and optical modulation. A summary of unique material properties of LN and their corresponding applications are presented in Fig. 1.1. A short description on EO and optical nonlinearity theories are given in Sections 1.4 and 1.9, respectively.

Traditionally, LN waveguides are fabricated using dopant diffusion or proton-exchange processes. The resultant low index-contrast waveguides (< 0.1) yield weak optical confinement. Therefore, conventional LN devices are bulky in general and exhibit low efficiency in terms of power consumption and device footprint, hence hampering the desired large-scale integration capability. As an example, high bending loss, long MZ electrode lengths, and low power efficiency due to large half-wave voltage-length product ($V_\pi \cdot L$), render the conventional LN electrooptic modulators (EOMs) unattractive for large-scale integration demands of advanced optical networks [2]–[5].

1.2 Heterogeneous Thin-Film Lithium Niobate

Thin-film approaches have been alternatively pursued to overcome these drawbacks of conventional LN waveguides and achieve ultracompact (submicron-scale) devices. Particularly, exploiting heterogeneous integration techniques, based on bonding of thin films of LN (TFLN) on oxidized Si substrates (as shown in Fig. 1.2), led to the emergence of ultracompact EOMs on Si substrates [6]. This technology is potentially compatible with Si photonics due to the choice of Si substrate.

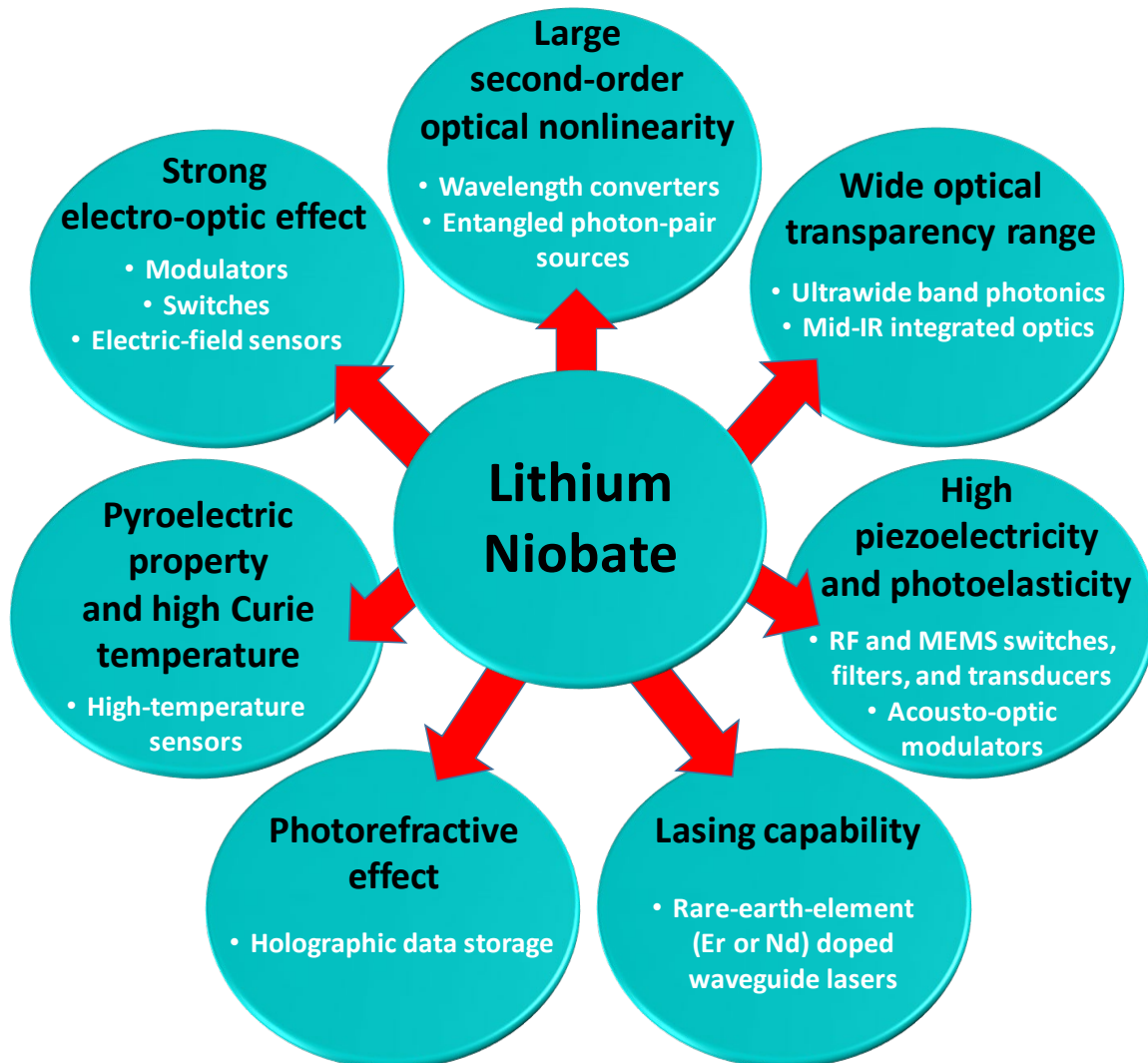


Figure 1.1: Summary of unique material properties of LN and their corresponding applications [1]. This dissertation focuses on the main photonic applications of LN through exploiting its strong EO effect and large second-order optical nonlinearity.

Various methods such as rib-loading the TFLN with a refractive-index-matched material (e. g. silicon nitride, SiN), direct dry etching, and wafer-, or individual die-bonding methods have been utilized in order to achieve ultracompact LN waveguides [1]. The optical mode size in the resultant waveguides is typically reduced by about two orders of magnitude compared to their bulk counterparts (see Fig. 1.3). A comprehensive review of various methods and recent strides made

towards this realization are given in Chapter 2.

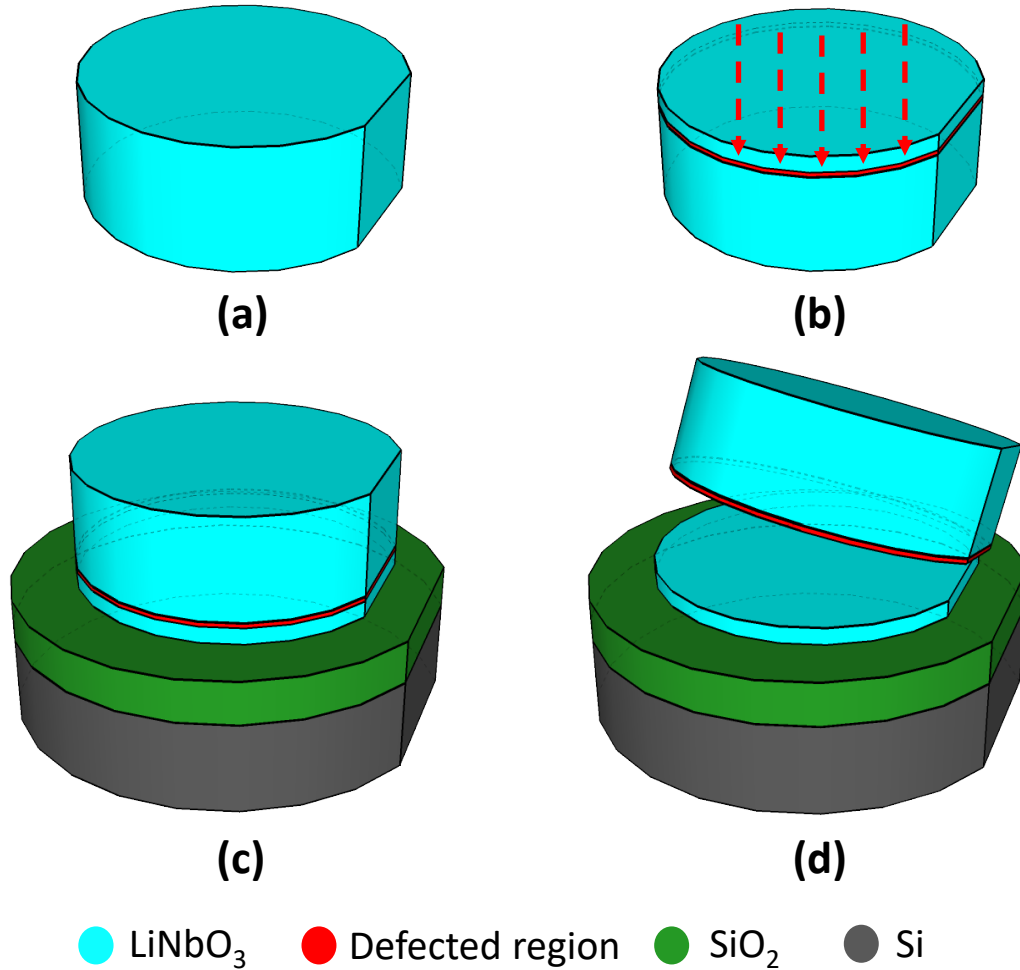


Figure 1.2: Fabrication steps of TFLN on Si wafers [1, 6]. (a) Initial bulk LN wafer; (b) Ion implantation (the red-dashedline shows the defected region at the desired depth of final thin-film thickness); (c) Bonding onto a Si handling wafer (or other wafers such as LN or quartz) with a low-index insulating layer (typically SiO₂); (d) Thermal cycling process to exfoliate the thin film from the LN crystal at the defected layer and the final TFLN on Si product. The remaining bulk LN crystal can be recycled. For simplicity, other steps such as thermal annealing for preserving the material properties of LN, and mechanical polishing for smoothening of the surface roughness are not depicted here.

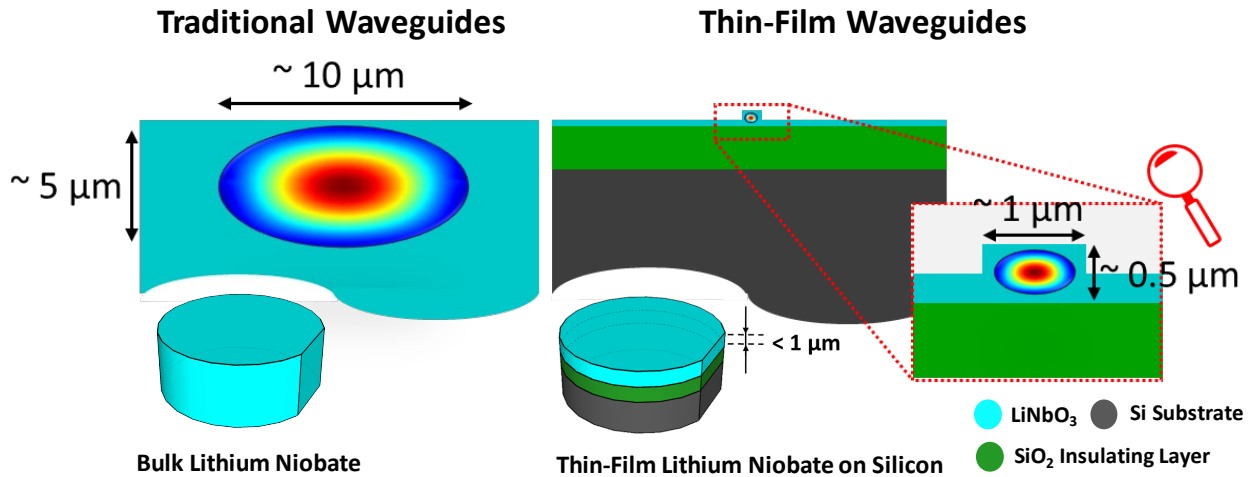


Figure 1.3: Comparison between (a) Conventional; (b) Compact, LN waveguide [1]. The waveguides cross-sections are drawn to scale to emphasize the significant reduction in optical mode size. This about two orders of magnitude reduction facilitates large-scale integration of photonic integrated circuits, as well as boosted performance for LN devices, as discussed in Chapter 2.

1.3 Electrooptic Modulators

High-performance optical modulation is an essential part of modern communication systems. Historically, commercial optical modulators have been made on materials with strong EO effect (e.g., LN) or electroabsorption (EA) effect (particularly, III-V compound semiconductors). More recently, Si optical modulators based on free-carrier plasma dispersion effect (FCA) are being widely pursued, as they benefit from compatibility with standard Si foundry processing. Another recent trend is heterogeneous integration of compound semiconductors as well as silicon germanium (SiGe), on silicon substrates that utilize EA effects such as Franz-Keldysh in bulk semiconductors or quantum-confined Stark effect in quantum-well structures. Several modulators operating based on FCA or EA have been demonstrated with high data transmission rates up to 50 Gb/s. However, they typically suffer from low extinction ratios [7].

On the contrary, modulators relying on linear EO or Pockel's effect have demonstrated modulation depth of 20 dB or more as well as up to 100 GHz modulation bandwidth (BW) [1]. With such performance, LN has been well established as the standard material of choice for EO

modulators in applications where high BW and extinction ratio are required, e.g., in long-haul communications. Transparency in a broad range of the electromagnetic spectrum (0.4-5 μm), and a large EO coefficient (31 pm/V) are among other reasons which make LN a suitable option for EO modulators [7]. A short description on EO effect is given in Section 1.4.

1.4 Pockel's Effect

The change in the refractive index (n) of a material by applying an electric field (E) is called the electrooptic (EO) effect. This change is the result of the displacement in the lattice structure. The dependence of n on E can be expressed as follows [8, 9]:

$$1/n^2 = 1/n_0^2 + rE + hE^2 + \dots, \quad (1.1)$$

where n_0 is the refractive index of the material before applying E , and r and h are the linear and the quadratic EO coefficients, respectively. In materials with centrosymmetric lattice structure, such as silicon, r is not available and the lowest-order change in n depends quadratically on E . This effect is known as Kerr electrooptic effect. On the other hand, materials which lack centrosymmetry, such as LN, possess the linear EO effect, called Pockel's effect, i.e., the refractive index change (Δn) is linearly proportional to E . Δn can be written as [8, 9]:

$$\Delta(1/n^2) = \sum r E = \begin{pmatrix} r_{11} & r_{12} & r_{13} \\ r_{21} & r_{22} & r_{23} \\ r_{31} & r_{32} & r_{33} \\ r_{41} & r_{42} & r_{43} \\ r_{51} & r_{52} & r_{53} \\ r_{61} & r_{62} & r_{63} \end{pmatrix} \begin{pmatrix} E_x \\ E_y \\ E_z \end{pmatrix}. \quad (1.2)$$

For LN, the largest coefficient is $r_{33} \simeq 31$ pm/V [8]. Hence, as explained later in Chapters

2 – 4, and 6, the electric field is applied along the z direction (E_z) in order to utilize the largest EO coefficient of LN.

1.5 Modeling of Ultracompact Electrooptic Modulators

By utilizing thin-film LN platform (see Fig. 1.2), we have reported high-speed TFLN LN EOMs on Si with 3-dB BWs of 33 GHz and an extinction ratio of 18 dB [10]. Recently, TFLN MZ EOMs with 3-dB BWs up to ~ 100 GHz have been demonstrated [11]–[13]. With this stage of maturity, accurate design of the ultracompact EOMs and reliable prediction of their high-speed performance limits demanded an elaborate model. We have developed such a general transmission-line model and verified its accuracy by comparing the simulated results with prior experimental data, as shown in Fig. 1.4 [7]. Despite some early work in recognizing the effect of frequency-dependent impedance mismatch in travelling-wave EO modulator, the commonly employed models in the literature for conventional LN modulators do not consider this effect. In these models, impedance matching is typically assumed between the MZ EO modulator’s transmission line characteristics and the terminating resistive load at all frequencies [7].

Unlike conventional models, the developed model presented in this work, is capable of accurately predicting the 3-dB BW of ultracompact LN EO modulators. By utilizing this model, and with proper design of such compact EO modulators, the overall EO performance can be improved in order to meet the requirements of advanced optical communication systems [7]. This has been reported in details in Chapter 3.

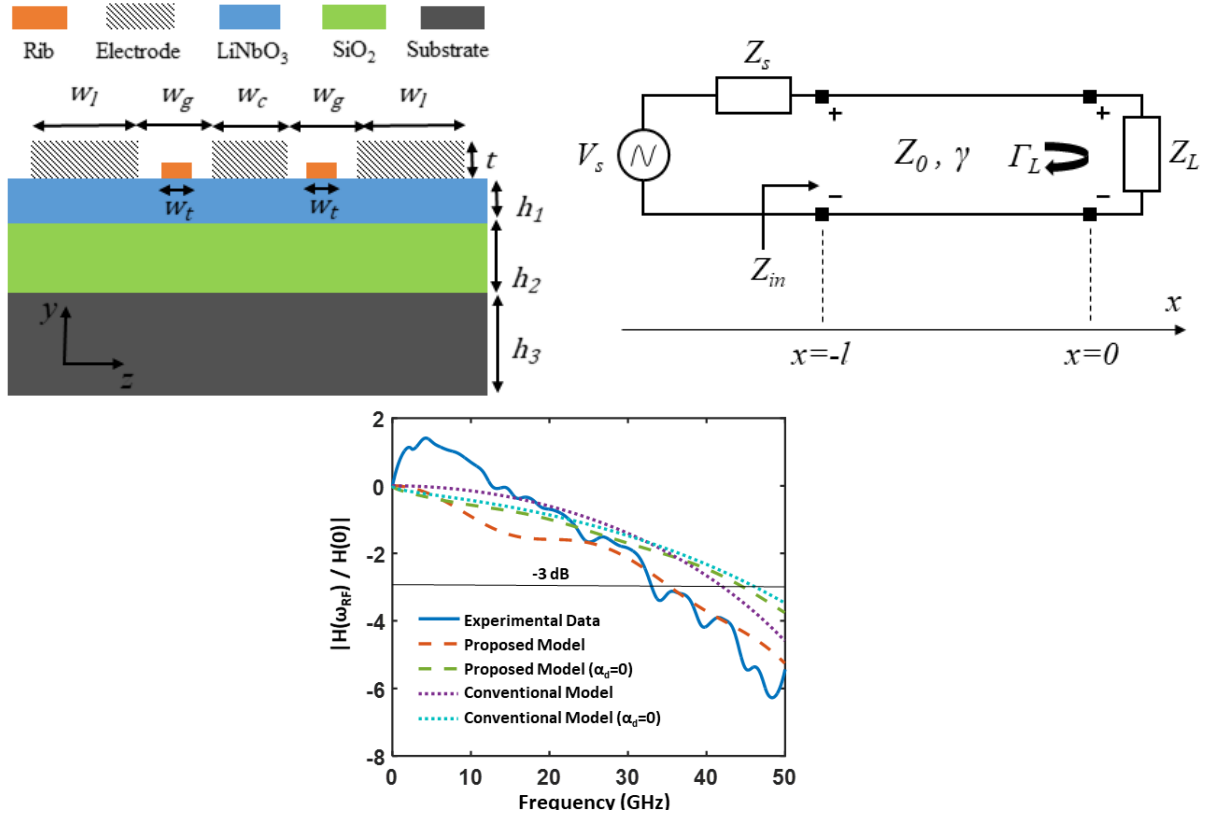


Figure 1.4: Modeling of RF and optical properties of ultracompact EOMs, as discussed in Chapter 3 [7].

1.6 Ultrahigh-Bandwidth Electrooptic Modulators

Ultrahigh-speed modulators are of great interest for ever-increasing aggregate BW requirements of optical communication systems. Due to increased complexity of the electronic and photonic systems, reduction in power consumption, manufacturing cost, device footprint, and overall packaged size are also demanded for analog and digital applications. Hence, in Chapter 4, novel designs are presented in order to attain ultrahigh-BW (up to 400 GHz) MZ EOMs, as depicted in Fig. 1.5 [14]. Radio-frequency (RF) and optical parameters of the devices have been studied, and design guidelines and optimization procedures are presented for such unprecedented 3-dB modulation BWs for both rib-loaded and direct-etched thin-film LN EOMs. This work paves the path towards exploiting the ultracompact devices in advanced integrated photonic circuits targeting futuristic optical

communication applications, analog or digital, where subterahertz (sub-THz) BWs are desired.

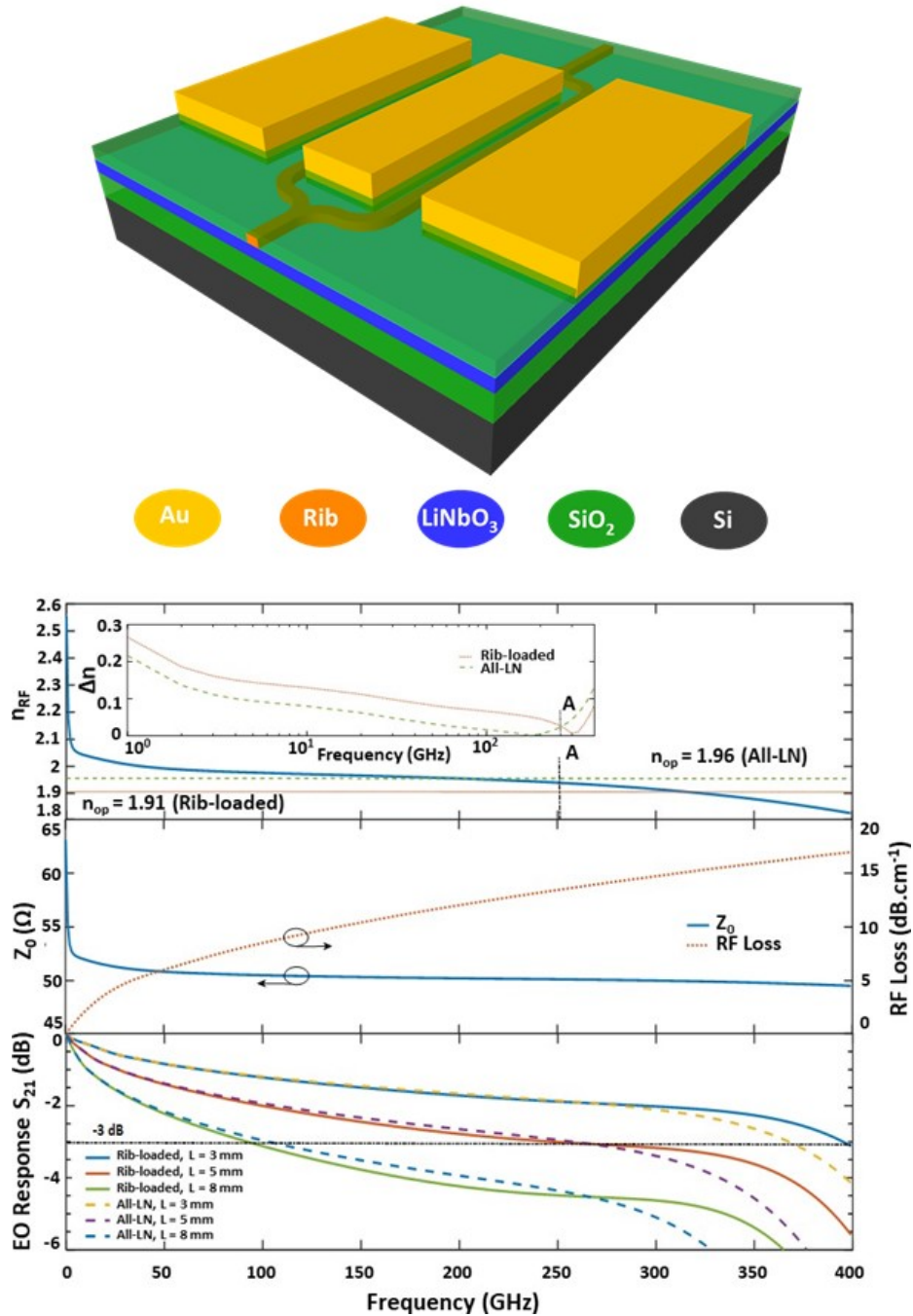


Figure 1.5: Design and optimization of ultracompact EOMs for ultrahigh-BW (sub-THz applications) [14].

1.7 Ultralow-Power Electrooptic Modulators

For applications such as optical interconnects, one of the the most critical requirements of densely-integrated photonic circuits is to increase the power efficiency of EOMs. Hence, as discussed in Chapter 6, a novel structure for TFLN MZ EOMs is designed and presented (see Fig. 1.6). As a result, the switching voltage of TFLN EOMs is reduced by a factor of about five. Moreover, in this design, the high-frequency operation of EOMs is not sacrificed and the devices can achieve up to 50 GHz while maintaining sub-volt switching voltages, rendering them compatible with on-chip electronic drivers using CMOS technology. This can significantly pave the path towards utilization of TFLN EOMs in applications where ultralow power consumption is required.

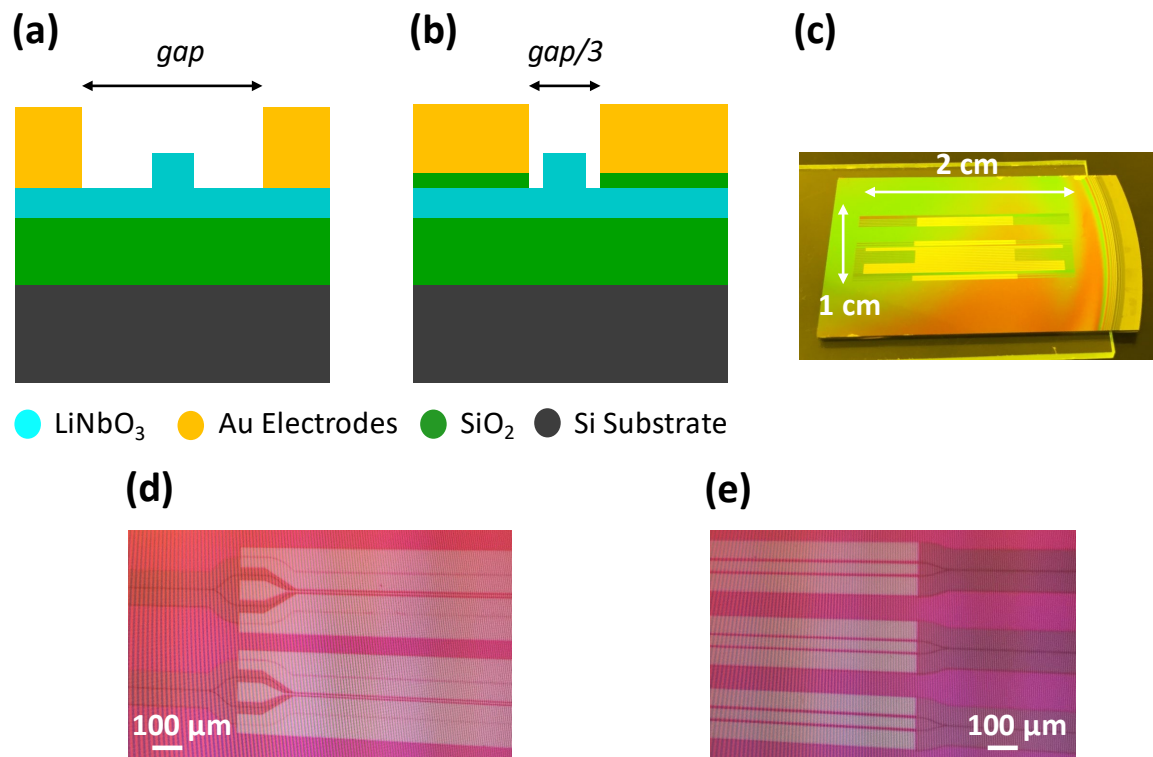


Figure 1.6: (a) Typical structure for the TFLN MZ EOM; (b) Proposed design for the ultralow-power EOMs. Lower gap between the electrodes can directly reduce the switching voltage of MZ EOMs, as discussed in Chapter 6; (c) Image of the fabricated chip; Microimages for two types of devices, designed for high-, and low-frequency operation, are given in (d), and (e), respectively.

1.8 Coherent Modulation on Thin-Film Lithium Niobate Platform

The technology for TFLN EOMs has made significant advances recently. With achieving high levels of maturity for this platform, the next step is to demonstrate higher modulation schemes, such as Quadrature Phase-Shift Keying (QPSK), which is required for coherent communication in advanced optical networks. In a QPSK modulator, transmission of phase information is utilized instead of amplitude modulation. In advanced optical communication systems, this results in lower transmitted optical power, and signal-to-noise ratio requirements [15].

While this has been previously reported for bulk LN [15] and all-Si modulators [16], to the best of our knowledge, the work presented in Chapter 6 of this dissertation, is the first demonstration of such devices on TFLN platform.

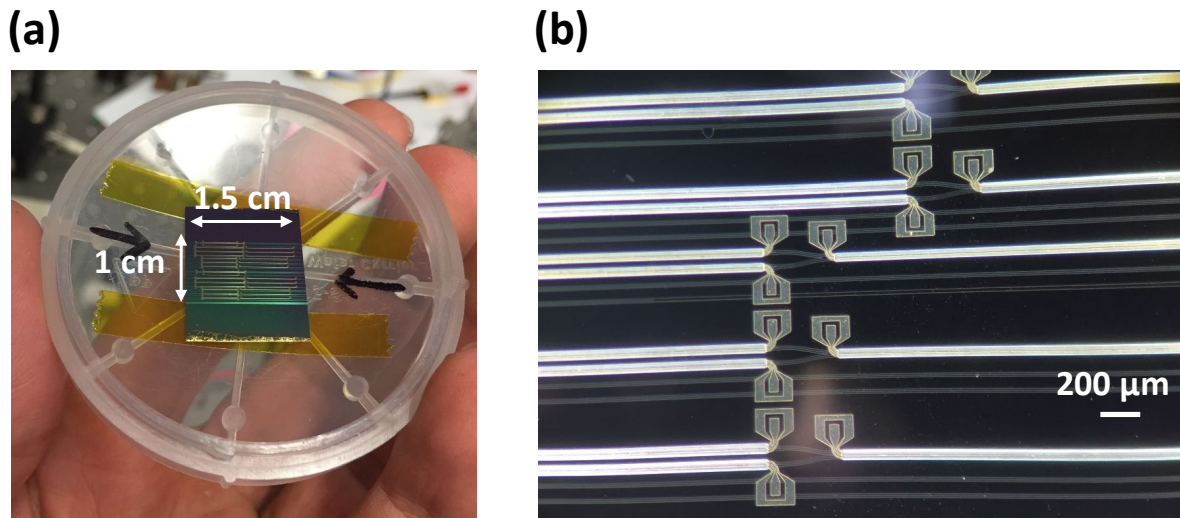


Figure 1.7: (a) Image of the fabricated chip; (b) Microimage of the TFLN QPSK EOMs.

1.9 Nonlinear Optical Properties

In light-matter interaction, the polarization response for an applied electric field is expressed by the following [8]:

$$P(E) = \epsilon_0 \chi E, \quad (1.3)$$

where ϵ_0 is the vacuum permittivity, and χ denotes optical susceptibility. However, for large enough applied electric field or in nonlinear materials, polarization response is no longer linear and can be written as [8]:

$$P(E) = \epsilon_0 [\chi^{(1)}E + \chi^{(2)}E^2 + \chi^{(3)}E^3 + \dots], \quad (1.4)$$

where χ^i 's are higher order optical susceptibilities. Materials with inversion symmetry in their lattice structure, such as silicon, lack χ^2 . These higher-order susceptibilities can be exploited in order to generate several nonlinear optical functionalities.

For example, second-harmonic generation (SHG), is a $\chi^{(2)}$ process which is employed in order to double the frequency of light, as depicted in Fig. 1.8(a). Another nonlinear functionality, supercontinuum generation (SCG), utilizes $\chi^{(3)}$ to generate a broad spectrum of light from a high power narrow-band laser pulse, as depicted in Fig. 1.8(b).

1.10 Cascaded Integration of Different Optical Nonlinearities on a Single Chip

Several shortcomings are well-known for Si, when it comes to nonlinear optical applications. For example, Si inherently lacks second-order optical susceptibility ($\chi^{(2)}$) due to its centrosymmetric lattice structure. This restricts convenient utilization of standard Si photonics for applications such as second-harmonic generation (SHG). Also, the presences of two-photon and free-carrier absorptions (TPA and FCA), at the required high optical intensities, limit the exploitation of silicon's

large third-order optical susceptibility ($\chi^{(3)}$), at least at telecom wavelengths [17].

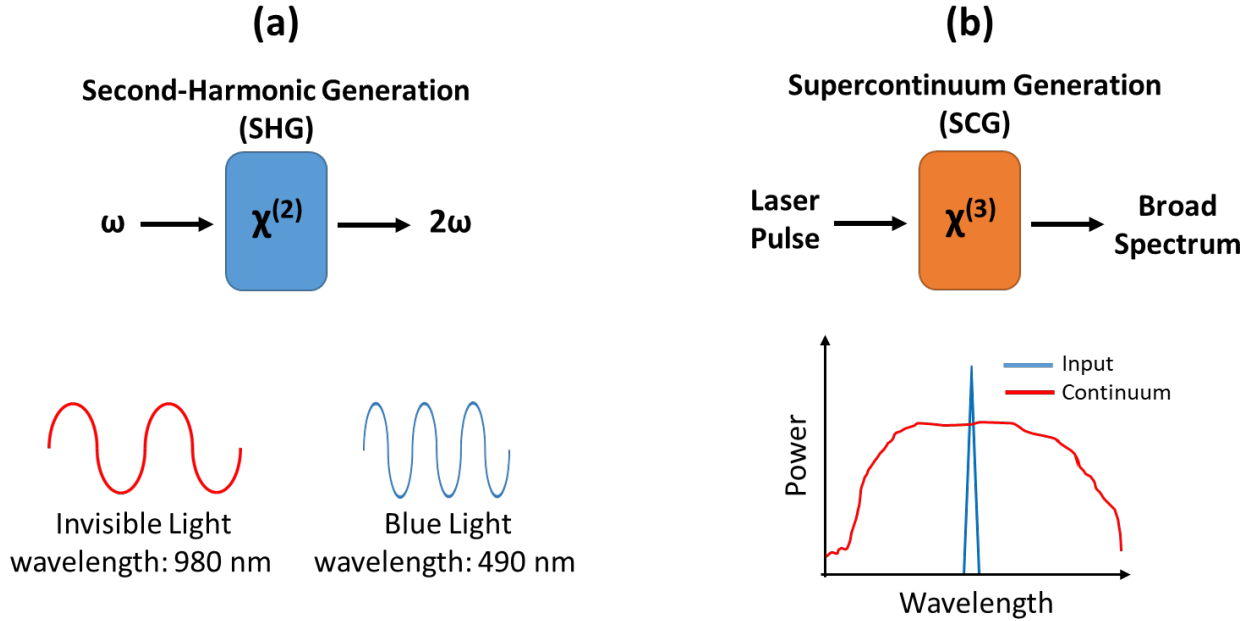


Figure 1.8: Examples of nonlinear optical processes: (a) Second-Harmonic generation (SHG); (b) Supercontinuum generation (SCG).

There has been several works on integration of other nonlinear materials on Si. However, the efforts have been primarily limited to integrating a "single" material. The new frontline of research should target monolithic integration of "multiple" materials/devices for more advanced functionalities on the same chip. For example, it is crucial to "co-integrate" cascaded waveguides with $\chi^{(2)}$ and $\chi^{(3)}$ properties in the context of frequency-stabilized optical comb generation. The $\chi^{(3)}$ waveguide provides octave-spanning SCG, while SHG in the $\chi^{(2)}$ device is used for stabilization by f -to- $2f$ carrier-envelope offset (CEO) locking.

In Chapter 5, we present cascaded integration of ChG glass and thin-film LN waveguides on the same Si chip. Carefully designed mode-converting tapers are employed for adiabatic optical mode transition from ChG to hybrid LN waveguides and vice versa. The presented work is the first effort in paving the path towards integration of two example materials, namely ChG ($\chi^{(3)}$) and LN ($\chi^{(2)}$) waveguides, towards this goal [17].

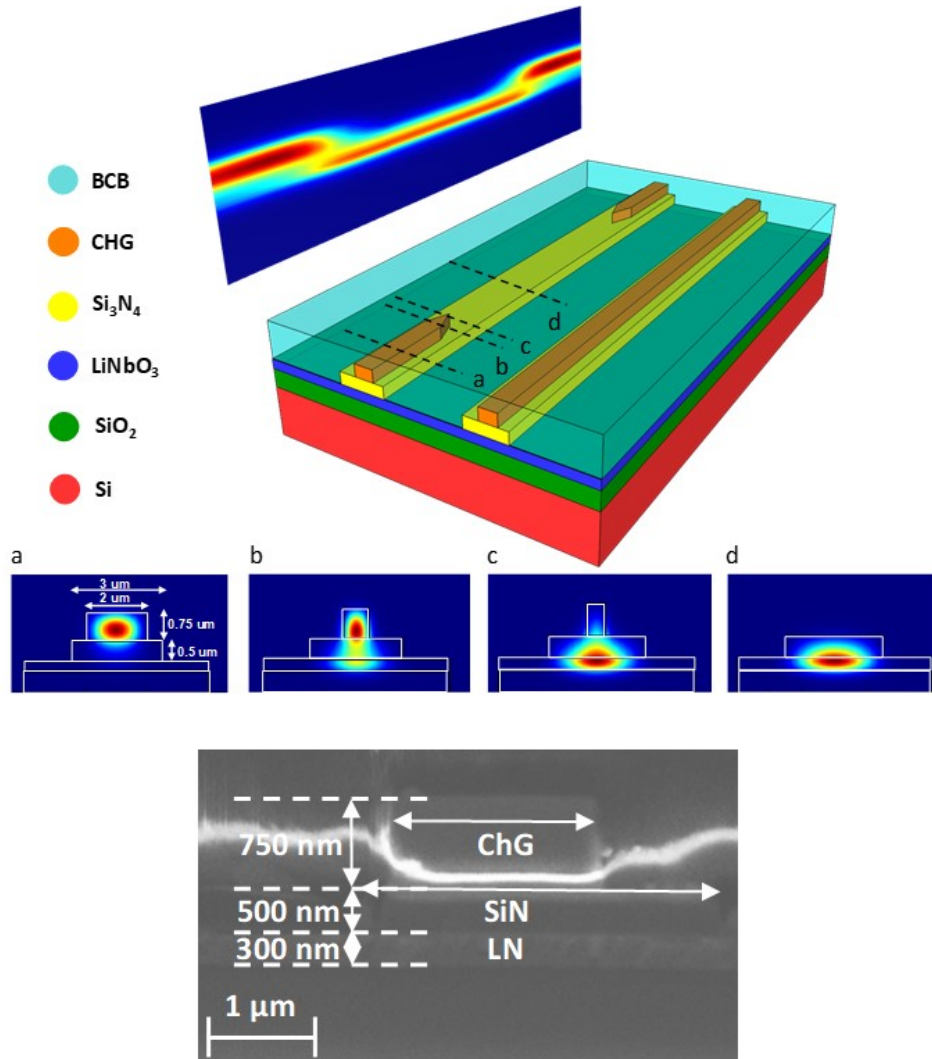


Figure 1.9: Demonstration of monolithic integration of waveguides with $\chi^{(2)}$ and $\chi^{(3)}$ optical non-linearity on a single Si chip [17]. The inset is an SEM image of the fabricated waveguide's cross-section denoted by 'b' on the schematic.

The extension of this work including a designed and fabricated novel structure is presented in Chapter 6.

1.11 Foundry-Compatible Integration of Thin-Film Lithium Niobate with Silicon Photonic

In order to exploit benefits of the mature Si photonic industry, namely its standard low-cost foundry-compatible processing and tightly-confined waveguides, a novel integration scheme is presented in detail in Chapter 6 [18]. A short description can also be found in Chapter 2, Section 2.2.2 (see Fig. 2.5). In this proposed scheme the thin films of LN are integrated at back end of the line. As depicted in Fig. 1.10, the intermediate SiN layer serves as an adiabatic mode converter as well as a rib, in order to efficiently transfer the optical mode from standard Si-on-insulator (SOI) waveguides into LN region. The fabrication steps for this scheme are summarized in Fig. 1.11.

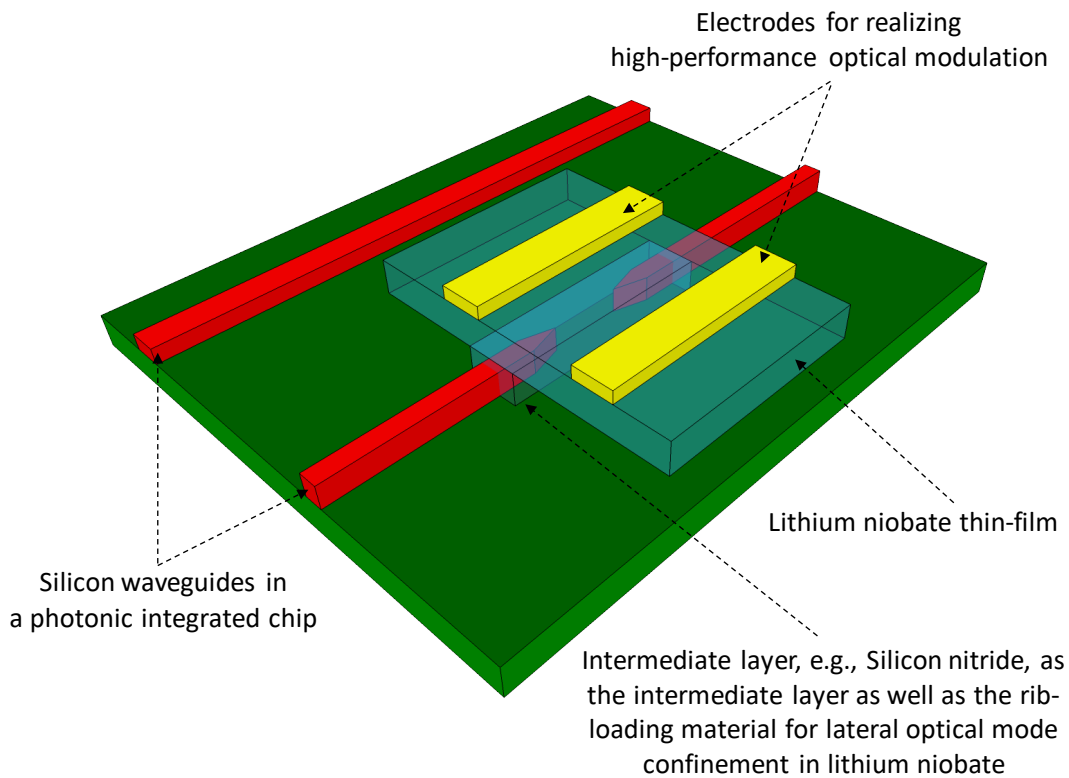


Figure 1.10: The schematic depicts the proposed scheme for back-end-of-line integration of TFLN devices with Si photonics. Details are discussed in Chapter 6.

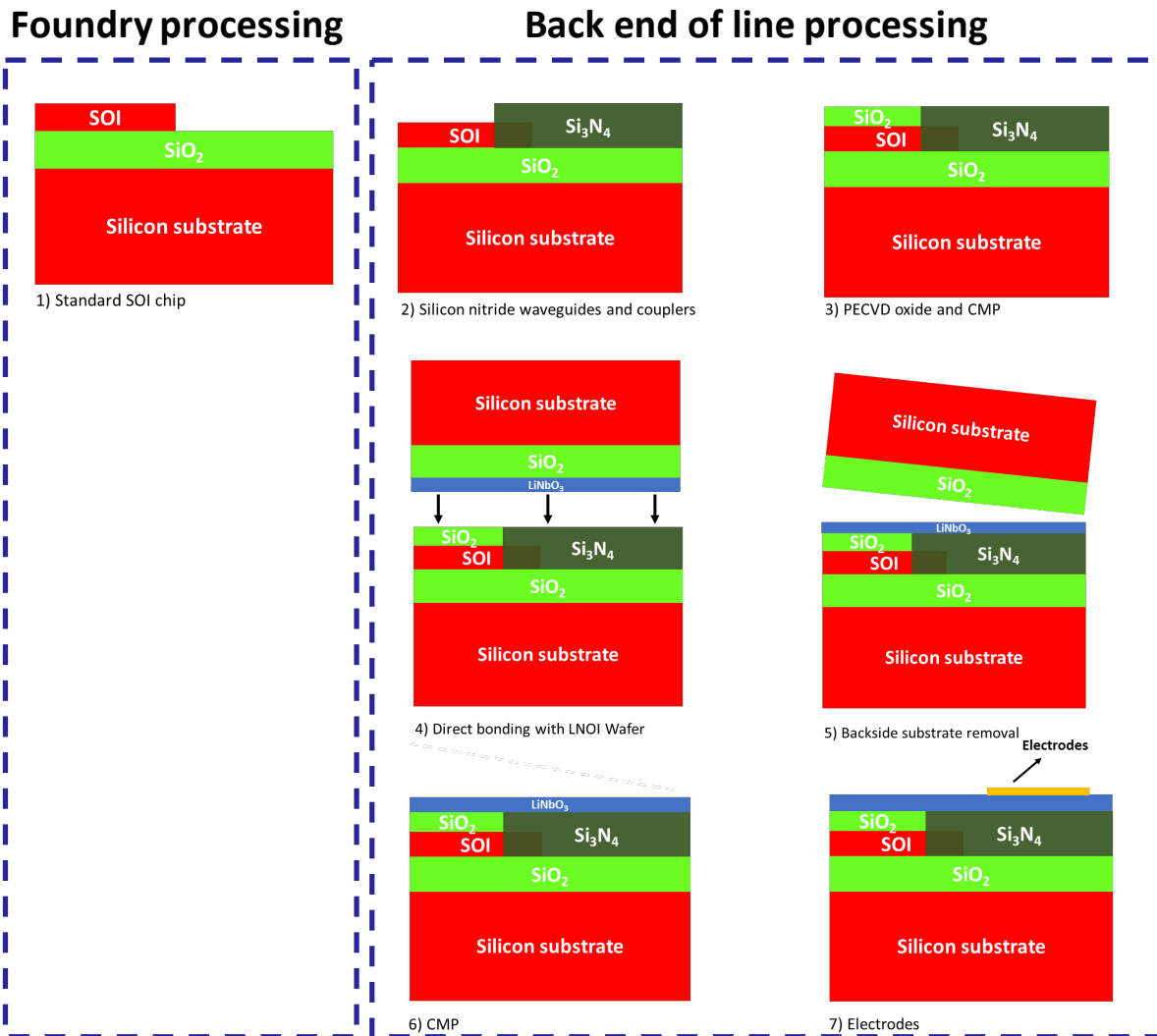


Figure 1.11: Summary of the fabrication steps for the proposed scheme. Details are discussed in Chapter 6.

1.12 Conclusion and Future Work

Finally, Chapter 6 concludes this dissertation by presenting the extensions of the demonstrated results for future work, and some preliminary results.

1.13 References

- [1] A. Honardoost, K. Abdelsalam, and S. Fathpour, “Rejuvenating a Versatile Photonic Material: Thin-Film Lithium Niobate,” *Laser & Photonics Reviews*, Under Review, 2020.
- [2] E. L. Wooten, K. M. Kissa, A. Yi-Yan, E. J. Murphy, D. A. Lafaw, P. F. Hallemeier, D. Maack, D. V. Attanasio, D. J. Fritz, G. J. McBrien, and D. E. Bossi, “A review of lithium niobate modulators for fiber-optic communications systems,” *IEEE J. Quant. Elec.*, vol. 6, no. 1, pp. 69–82, 2000.
- [3] K. Noguchi, O. Mitomi, and H. Miyazawa, “Millimeter-wave Ti:LiNbO₃ optical modulators,” *IEEE J. Light. Technol.*, vol. 16, no. 4, pp. 615–619, 1998.
- [4] S. Fathpour, “Emerging heterogeneous integrated photonic platforms on silicon,” *Nanophotonics*, vol. 4, no. 1, pp. 143–164, 2015.
- [5] A. Rao, and S. Fathpour, “Compact lithium niobate electrooptic modulators,” *IEEE J. Sel. Top. Quantum Electron.*, vol. 24, no. 4, pp. 1–14, 2018.
- [6] P. Rabiei, J. Ma, S. Khan, J. Chiles, and S. Fathpour, “Heterogeneous lithium niobate photonics on silicon substrates,” *Opt. Express*, vol. 21, no. 21, pp. 25573–25581, 2013.
- [7] A. Honardoost, R. Safian, A. Rao, and S. Fathpour, “High-speed modeling of ultracompact electrooptic modulators,” *IEEE J. Light. Technol.*, vol. 36, no. 24, pp. 5893–5902 (2018).
- [8] R. W. Boyd, “Nonlinear optics,” 3rd edition, *Academic Press*, 2008.
- [9] T. S. El-Bawab, “Optical switching,” 1th edition, *Springer*, 2005.
- [10] A. Rao, A. Patil, P. Rabiei, A. Honardoost, R. DeSalvo, A. Paoella, and S. Fathpour, “High-performance and linear thin-film lithium niobate Mach-Zehnder modulators on silicon up to 50 GHz,” *Opt. Lett.*, vol. 41, no. 24, pp. 5700–5703, 2016.

- [11] C. Wang, M. Zhang, X. Chen, M. Bertrand, A. Shams-Ansari, S. Chandrasekhar, P. Winzer, and M. Loncar, “Integrated lithium niobate electro-optic modulators operating at CMOS-compatible voltages,” *Nature*, **562**, 101–104 (2018).
- [12] P. O. Weigel, J. Zhao, K. Fang, H. Al-Rubaye, D. Trotter, D. Hood, J. Mudrick, C. Dallo, A. T. Pomerene, A. L. Starbuck, C. T. DeRose, A. L. Lentine, G. Rebeiz, and S. Mookherjee, “Bonded thin film lithium niobate modulator on a silicon photonics platform exceeding 100 GHz 3-dB electrical modulation bandwidth,” *Optics Express*, vol. 26, no. 18, pp. 23728–23739, 2018.
- [13] M. He, M. Xu, Y. Ren, J. Jian, Z. Ruan, Y. Xu, S. Gao, S. Sun, X. Wen, L. Zhou, L. Liu, C. Guo, H. Chen, S. Yu, L. Liu, and X. Cai, “High-performance hybrid silicon and lithium niobate Mach–Zehnder modulators for 100 Gbit s⁻¹ and beyond,” *Nature Photonics*, vol. 13, no. 5, pp. 359–364, 2019.
- [14] A. Honardoost, F. A. Juneghani, R. Safian, and S. Fathpour, “Towards subterahertz bandwidth ultracompact lithium niobate electrooptic modulator,” *Opt. Express*, vol. 27, no. 5, pp. 6495–6501 (2019).
- [15] A. Kaplan, K. Achiam, A. Greenblatt, G. Harston, and P. S. Cho, “LiNbO₃ Integrated Optical QPSK Modulator and Coherent Receiver,” *Proc. Eur. Conf. Integrated Optics (ECIO)*, pp. 79–82, 2003.
- [16] P. Dong, L. Chen, C. Xie, L. L. Buhl, and Y. -K. Chen, “50-Gb/s silicon quadrature phase-shift keying modulator,” *Opt. Express*, vol. 20, no. 19, pp. 21181–21186, 2012.
- [17] A. Honardoost, G. F. Camacho Gonzalez, S. Khan, M. Malinowski, A. Rao, J. -E. Tremblay, A. Yadav, K. A. Richardson, M. C. Wu, and S. Fathpour, “Cascaded integration of optical waveguides with third-order nonlinearity with lithium niobate waveguides on silicon substrates,” *IEEE Photon. J.*, vol. 10, no. 3, Art. no. 4500909, 2018.

- [18] S. Fathpour, A. Honardoost, and S. Khan, “Thin-film integration compatible with silicon photonics foundry production,” *US Patent App. 15/932,800*, 2018.

CHAPTER 2: THIN-FILM LITHIUM NIOBATE PHOTONICS

The contents of this chapter were submitted to Laser & Photonics Reviews on March 9, 2020 as a review article under the 2020 WILEY-VCH Verlag GmbH & Co. KGaA, Weinheim license under the title: “Rejuvenating a Versatile Photonic Material: Thin-Film Lithium Niobate,” A. Honardoost, K. Abdelsalam, and S. Fathpour.

Abstract– The excellent optical and unique material properties of lithium niobate have long established it as a prevailing photonic material, especially for the long-haul telecom modulator and wavelength-converter applications. However, conventional lithium niobate optical waveguides are bulky, hence large-scale photonic circuit implementations are impeded and high power requirements are imposed. To address these shortcomings, thin-film lithium niobate technology has been a topic of intense research in the last few years and a plethora of ultracompact devices with significantly superior performances than the conventional counterparts have been demonstrated. These efforts have rejuvenated lithium niobate for novel electro-, nonlinear-, and quantum-optic applications. This Review summarizes the most recent advancements of this booming field and concludes with a perspective for future directions.

2.1 Introduction

Lithium niobate (LiNbO_3 , LN) has been recognized as a versatile material for over half a century, thanks to its strong ferroelectric, piezoelectric, electrooptic, thermooptic, acoustooptic, pyroelectric and other properties [1]. Improvements in bulk crystal growth by the Czochralski technique has rendered LN a dominant choice for applications based on these properties, as summarized in Figure 2.1(a). Particularly for optical applications, strong electrooptic (EO) coefficient ($r_{33} \approx 31$ pm/V), large nonlinearity ($d_{33} = 30$ pm/V), remarkable thermooptic birefringence and a broad transparency range in the electromagnetic spectrum ($0.4 - 5 \mu\text{m}$) ought to be highlighted

[2]–[5].

Indeed, LN has been the standard material of choice for the EO modulators used in long-haul communication [6] and nonlinear wavelength-converters [7]. Several commercial off-the-shelf modulator products are available with high performance, i.e., up to 50 GHz bandwidth (BW) and large extinction ratios (ER) [8]–[10]. Also, $\sim 250 \text{ \%W}^{-1}\text{cm}^{-2}$ normalized conversion efficiency for second-harmonic generation (SHG) has been commercialized [11]–[13].

With the ever-increasing complexity of modern optical systems, there has been a growing demand for reduction in power consumption, device footprint, and manufacturing cost of photonic integrated circuits (PICs) in the past decades. While the mature silicon (Si) photonic technology can meet these requirements [14]–[17], owing to its standard low-cost foundry-compatible processing and tightly-confined waveguides, the performance of LN-based modulators and wavelength converters are unrivaled by their all-Si-based counterparts. Lack of linear EO via Pockel’s effect, lack of second-order nonlinearity ($\chi^{(2)}$) due to silicon’s centrosymmetric lattice structure, and nonlinear two-photon and free-carrier absorption effects are among the hurdles of silicon photonics [4].

On the other hand, conventional LN devices are bulky and power hungry in general. Traditionally, LN waveguides are commonly formed by in-diffusion of dopants, such as titanium (Ti) [18], or proton-exchange (PE) [19] processes. While low propagation loss is attainable, these methods only slightly alter the refractive index of the material ($\Delta n \approx 0.1$), which yields in weak optical confinement. Hence, conventional LN devices suffer from a number of shortcomings, including large bending radii in general, increased half-wave voltage-length product ($V_\pi \cdot L$), and long Mach-Zehnder (MZ) arm lengths for EO modulators [20, 21], as well as limited nonlinear conversion efficiency due to the inefficient overlap of the resultant large optical modes in guided devices for wavelength conversion, e.g., periodically-poled LN (PPLN) waveguides for SHG [7, 22]. Essentially, these shortcomings impede the exploitation of conventional bulk LN devices for large-scale PICs.

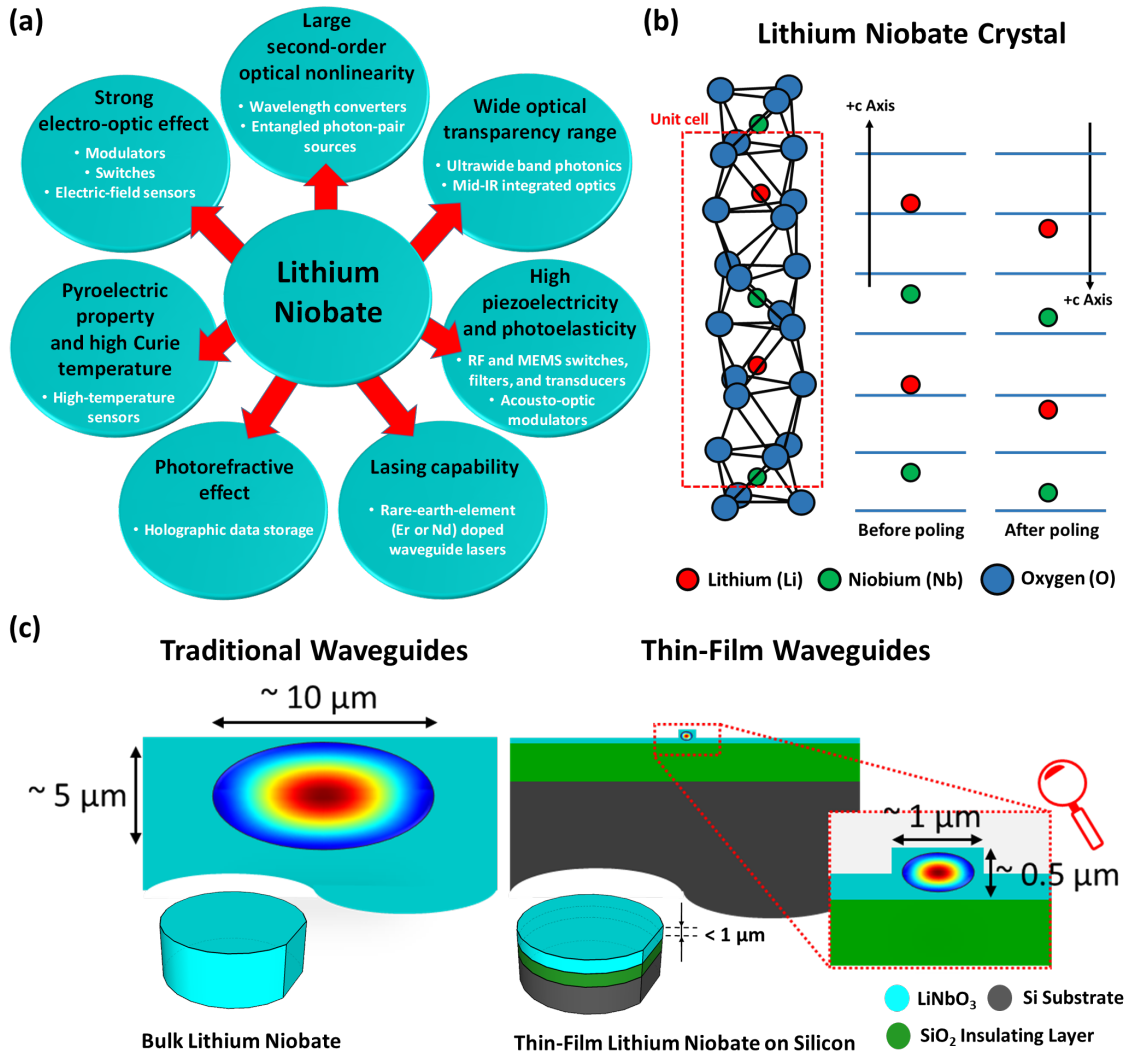


Figure 2.1: (a) Summary of unique material properties of LN [1]–[7], [23]–[26]. This review focuses on the main photonic applications of LN through exploiting its strong EO effect and large second-order optical nonlinearity; (b) Crystalline structure of LN in ferroelectric phase. The red dashed-box represents its unit cell. The horizontal blue lines depict the oxygen (O) layers and the position of lithium (Li) and niobium (Nb) atoms are shown with respect to it (after [2, 27]). The position of the atoms are shown before and after the poling process, as discussed in Section 2.4.1; (c) Comparison between the traditional bulk versus thin-film LN waveguides. The figures for the waveguides cross-sections are drawn to scale to emphasize the significant reduction in optical mode size. This about two orders of magnitude reduction facilitates large-scale integration of photonic integrated circuits, as well as boosted performance for LN devices, e.g., reduced $V_{\pi} \cdot L$ for TFLN EOMs and increased mode overlap and efficiency for PPLN waveguides. The steps for fabrication of TFLN wafers on Si are presented in Figure 2.2.

As a solution, thin-film LN (TFLN) approaches have been pursued since 2004 [29] by using crystal ion slicing [30] and room-temperature wafer bonding [31, 32] methods. TFLN on Si substrate was first demonstrated at CREOL in 2013 [28]. Among other advantages (e.g., cost, scalability, ease of handling thermal cycles), the choice of Si substrate has paved the path towards heterogeneous integration of TFLN devices with Si photonics. Since then, commercialization of TFLN wafers by a CREOL spinoff company [33], as well as other vendors [34, 35], have facilitated the availability of this platform for extensive research. In addition, other methods such as direct bonding [36] and benzocyclobutene (BCB) bonding [37] of individual TFLN dies on Si, as well as mechanical thinning of bulk LN [38], have been pursued. In order to achieve low-loss submicron waveguides, several methods have been demonstrated on the TFLN technology. They include rib-loading with a refractive-index-matched material [28, 39], [40]–[43], dry etching [44]–[48], PE [49, 50], Ti in-diffusion [51], direct- or BCB-bonding on silicon-on-insulator (SOI) [52, 53, 37], plasma-enhanced chemical deposition (PECVD) of other materials, such as amorphous Si [54], and mechanical thinning [38]. The optical mode size in these waveguides is typically reduced by about two orders of magnitude compared to their bulk counterparts (see Figure 2.1c).

In recent years, based on this rapidly-growing technology, a plethora of ultracompact integrated photonic devices and circuits, such as microdisk [55]–[57] and microring [44], [58]–[61] resonators, EO modulators [62]–[79], acousto-optic modulators [80]–[82], grating couplers [83]–[87], fiber-to-chip edge couplers [88, 89], wavelength converters [90]–[101], entangled-photon sources [102]–[106] with significantly superior performances than their conventional LN counterparts have been demonstrated. The overall efforts have rejuvenated LN for novel electro-, nonlinear-, and quantum-optic applications and the material is considered among the top candidates for heterogeneous integrated photonics, where multiple materials are monolithically integrated on a single chip, while each material is chosen for the functionalities that suits it best.

Here, we summarize the most recent advancements of this flourishing field for its main photonic applications. The review is structured as follows. Section 2.2 gives a brief overview of the

strides made towards the realization of ultracompact TFLN waveguides with the mentioned various approaches and the associated challenges in order to achieve low-propagation loss. In Sections 2.3, 2.4, and 2.5 the path from first realization to the state-of-the-art performance is chronologically reviewed for electro-, nonlinear-, and quantum-optic applications, respectively. Section 2.6 lays out a roadmap for future directions, and concluding remarks are given in Section 2.7.

For completeness, it should be mentioned that the detailed design guidelines of these devices are obviously beyond the scope of this work. Moreover, it is noted that while this paper focuses on various advancements of TFLN field, realization of ultracompact integrated photonic devices, such as EO modulators and wavelength converters are not limited to this platform. For other material platforms, readers are referred to relevant references [107]–[111].

2.2 TFLN Platforms and Waveguides

2.2.1 *Thin-Film Platforms*

As mentioned in the Introduction, TFLN approaches have been pursued in order to overcome the drawbacks associated with bulk LN devices and have led to the LN-on-insulator (LNOI) platform. The insulator layer is comprised of a lower refractive index material, such as silicon dioxide (SiO_2), in order to avoid optical mode leakage from the thin film into the substrate. Among different choice of substrates, e.g., LN and Quartz, Si has been the most attractive one due to its potential for compatibility with Si photonics [28]. As mentioned before, other attributions such as cost, scalability and thermal handling are important too.

In this approach, single-crystalline LN is implanted with helium (He) or other low-mass ions. Next, the ion-implanted wafer is bonded to an oxidized Si wafer. Then, through thermal cycling processes, the TFLN is exfoliated from the bulk crystal and remains bonded onto the oxidized Si substrate. It has been shown that the EO and nonlinear properties of LN is preserved at the end of the process [112]. Figure 2.2 summarizes the fabrication steps for this method.

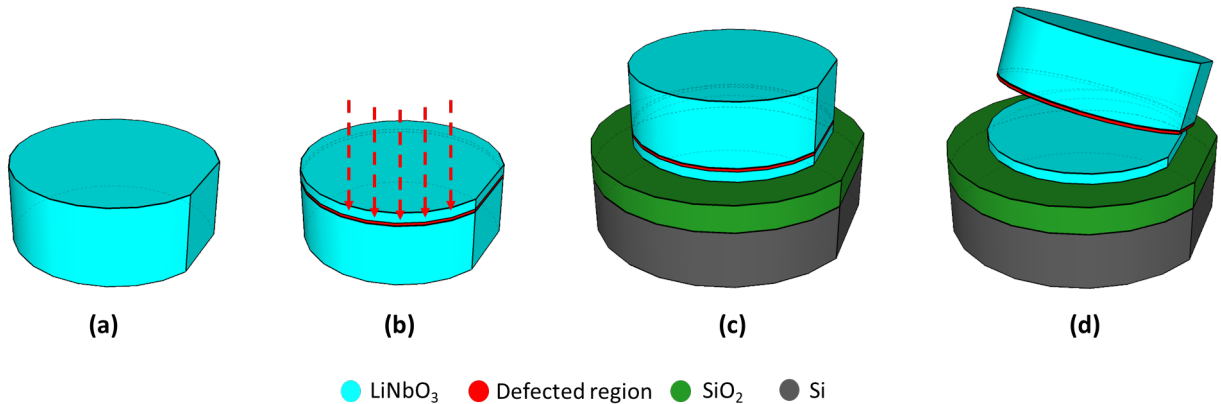


Figure 2.2: Summary of the steps for fabrication of TFLN on Si wafers [28]. (a) Initial bulk LN wafer; (b) Ion implantation (the red-dashed line shows the defected region at the desired depth of final thin-film thickness); (c) Bonding onto a Si handling wafer (or other wafers such as LN or quartz) with a low-index insulating layer (typically SiO₂); (d) Thermal cycling process to exfoliate the thin film from the LN crystal at the defected layer and the final TFLN on Si product. The remaining bulk LN crystal can be recycled. For simplicity, other steps such as thermal annealing for preserving the material properties of LN, and mechanical polishing for smoothing of the surface roughness are not depicted here.

Currently, TFLN wafers on Si and other substrates with different crystal cuts are commercially available from suppliers in the US [33], in China [34], and in Japan [35].

Another approach is using polymers, such as BCB, for bonding individual dies or full wafers of TFLN to Si [36, 37, 58, 62]. However, thermal stability and temporal reliability of polymers remain a major concern.

2.2.2 Ultracompact Waveguides

As summarized in Figure 2.3, various approaches have been pursued in order to form optical waveguides on TFLN. In the following, we discuss these approaches and explore their merits.

Historically, LN has been difficult to etch and the roughness of the etched sidewalls, as well as re-deposition of the chemical-etching byproducts, have contributed to large amounts of scattering and propagation losses [21, 110]. As a solution, one method has been to rib-load the TFLN with a material whose refractive index ($\sim 2 - 2.2$) is close to that of LN (~ 2.2) (see Figure 2.3a).

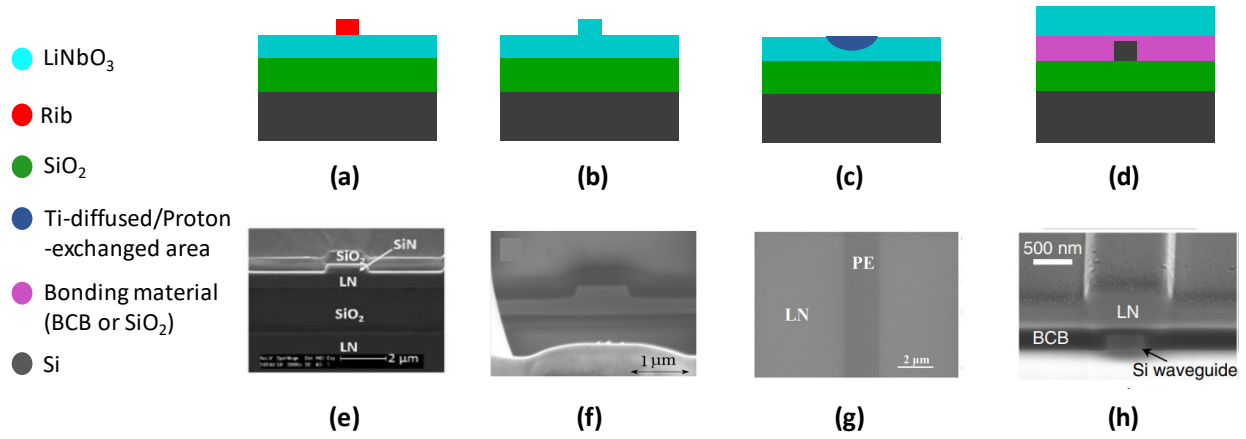


Figure 2.3: Common waveguide structures for TFLN-on-Si devices: (a) Rib-loaded, (b) dry-etched, (c) proton-exchanged or Ti-diffused, and (d) SOI-bonded structures; These methods can also be applied to TFLN on LN or quartz substrates. The majority of recent work demonstrating high-performance TFLN EOMs are utilizing rib-loaded (Figure 2.3a) [66], dry-etched (Figure 2.3b) [70, 73], and SOI-bonded (Figure 2.3d) [71, 72, 74, 78] methods, while for nonlinear devices, rib-loaded [90, 91] and dry-etched [92, 95] have been the most commonly employed platforms. In comparison to platforms (a)-(c), platform (d) requires additional bonding and TFLN substrate removal steps. The microimages for (e) rib-loaded, (f) dry-etched, (g) proton-exchanged, and (d) SOI-bonded waveguides, are reproduced with permission from [91], [45], [50], and [74], respectively.

One of the main advantages of this method is the ease of processing. Several materials have been pursued in this regard, such as tantalum pentoxide (Ta_2O_5) [28], chalcogenide glass (ChG) [65], silicon nitride (SiN , Si_3N_4) [40, 66, 67, 75, 79, 90, 91, 113], and titanium dioxide (TiO_2) [39], with reported propagation loss values as low as ~ 1 dB/cm for plasma-enhanced chemical-vapor deposition (PECVD) of SiN rib [66, 90]. Although other forms of deposition, such as low-pressure chemical-vapor deposition (LPCVD), can offer rib materials with much lower propagation loss, the standard TFLN wafers cannot withstand the high temperature used in these type of processes. Alternatively, LPCVD-SiN can be bonded to TFLN [40, 42], offering loss values as low as ~ 0.3 dB/cm [40].

The rib material's effective index and dimensions can be engineered to provide high optical mode overlap (more than 70%) in TFLN, in order to efficiently utilize its EO and nonlinear prop-

erties [110]. Another advantage of rib-loaded method is that it can be applied to all crystal cuts of TFLN, whereas some other methods which are discussed in the following, can only be applied to certain cuts. This method has also been utilized for bulk LN crystals in order to form compact waveguides using monocrystalline [114, 115] or amorphous [54] Si.

More recently, promising works [44]–[47] have been reported on low-loss dry-etching of LN with reported loss values as low as 0.027 dB/cm [44] for *X*-cut, and < 2-nm sidewall roughness [45] for *Z*-cut TFLN. Following the dry-etching of LN, the waveguides have to undergo a thorough RCA cleaning step in order to remove the organic residue and chemical byproducts of the etching process [47]. In a recent work [46], a combination of PE and dry etching is presented for efficient direct-etching of TFLN, i.e., faster etch rates while avoiding re-deposition of byproducts. By using this method, low-loss channel waveguides with large etch depths (~ 900 nm) and improved verticality of sidewalls are reported in *X*-cut TFLN. It is important to note that the dry-etching method can result differently for various crystal cuts of LN, e.g., re-deposition of byproducts from dry etching are different for *Z*-cut compared to the *X*- or *Y*-cut LN [110].

As depicted in Figure 2.3b, dry-etched waveguides have been also utilized for TFLN EO modulators (EOMs) [68, 69, 70, 73] and nonlinear devices [90]–[92], [95]. For EOMs, in comparison with rib-loading, this approach provides higher optical confinement in LN, which can consequently result in smaller electrode gaps in MZ-based devices, hence reducing the EOM's V_π . However, in the presence of certain requirements due to ultrahigh-speed design, the rib-loaded method is more advantageous due to the lower dielectric constant of the rib compared to that of LN [116].

Figure 2.3c shows another type of waveguide in the TFLN platform. PE or annealed-PE (PE followed by a high-temperature annealing step in order to recover the LN EO properties) processes are low-cost technologies, which are well-established for conventional bulk LN devices [6, 118]. In this process, the lithium ions in the crystal are exchanged with protons from an acid bath. This results in a small increase in the extraordinary refractive index, which can confine

the optical mode in the exchanged region. This method has been applied to TFLN [49, 50] and waveguide loss values as low as 0.2 dB/cm have been achieved in *X*-cut TFLN [50]. Although the optical mode sized can be reduced to $\sim 0.6 \mu\text{m}^2$, the main downsides of this platform are weak optical confinement, and very large bending radii, which are two to three orders of magnitude higher than values in other TFLN platforms. Moreover, since the acid chemically etches the *Y*-cut LN, this process can only be applied to *X*- or *Z*-cut TFLN [6]. More recently, in-diffusion of Ti, another well-established process for conventional EOMs, is also utilized in an LNOI structure, and a TFLN MZ EOM is reported [51].

In order to exploit benefits of the mature Si photonic industry, an interesting type of platform is recently pursued, in which the TFLN is bonded at the end stages of fabrication onto a patterned SOI wafer [37, 117]. Figure 2.3d depicts such a structure. Common types of bonding are direct-bonding using SiO_2 [71, 72, 74], or by using an adhesive polymer like BCB [36, 37], [62]–[64]. However, direct-bonding is usually preferred due to stability and reliability issues with BCB, as previously pointed out in Section 2.2.1.

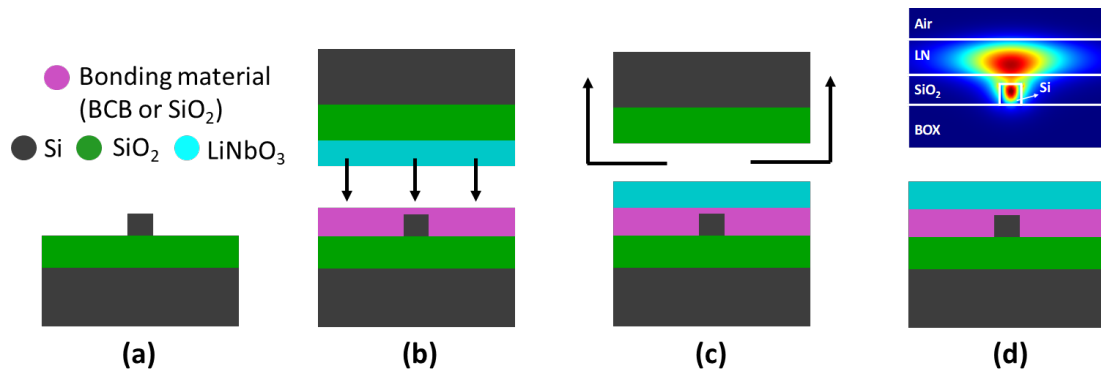


Figure 2.4: Fabrication steps for bonded-SOI TFLN platform [71, 72, 74, 117]: (a) Patterned SOI structure; (b) TFLN (see Figure 2.2d) bonding onto the SOI wafer using SiO_2 or BCB; (c) TFLN substrate removal; (d) Prepared structure and associated optical mode simulation. At this step, metallic electrodes can be deposited on top in order to form LN photonic devices such as EOM and PPLN waveguides.

The fabrication steps for this platform are summarized in Figure 2.4 [117]. Figure 2.4a

shows the prepared SOI waveguides. To form hybrid waveguides, the width of the Si waveguide is decreased, in order to confine most of the optical mode in the TFLN region. As a result of this Si waveguide narrowing, a disadvantage is the more interaction of optical mode with Si waveguide sidewalls which could yield in additional loss. Figures 2.4b and 2.4c depict the TFLN bonding and substrate removal steps, respectively. Another challenge for this approach is achieving the desired amount of thin bonding-material layer between the SOI and TFLN regions. The schematic of the prepared hybrid waveguide and its associate optical mode simulation are shown in Figure 2.4d. In this step, metallic electrodes can be deposited and patterned on top for realizing EOM or other devices.

A more robust approach is using an intermediate layer, such as LPCVD-formed SiN serving as an adiabatic mode converter as well as a rib, in order to efficiently transfer the optical mode from standard SOI waveguides into LN region [117] (see Figure 2.5). Another variation is to embed the metallic electrodes into the bottom optical waveguide structure, as recently reported for TFLN EOMs[79]. This eliminates the need for TFLN substrate removal and results in a more straightforward fabrication process.

In summary, by employing TFLN technology (see Figure 2.2d), various methods discussed in this section have resulted in ultracompact TFLN waveguides. The optical mode size and the waveguide propagation loss have been reduced by one to two orders (depending on the waveguide platform choice), and one order of magnitude, respectively, compared to the Ti-diffused or PE bulk LN counterparts [22, 44]. The propagation loss values of each TFLN platform are summarized in Table 2.1.

It is noted that among the above mentioned structures, most of the recently-demonstrated high-performance TFLN EOMs have utilized rib-loaded [66], dry-etched [70, 73], and SOI-bonded [71, 74] methods integrated on Si substrate. For nonlinear LN devices, rib-loaded [90, 91] and dry-etched [92, 95] methods have been employed so far.

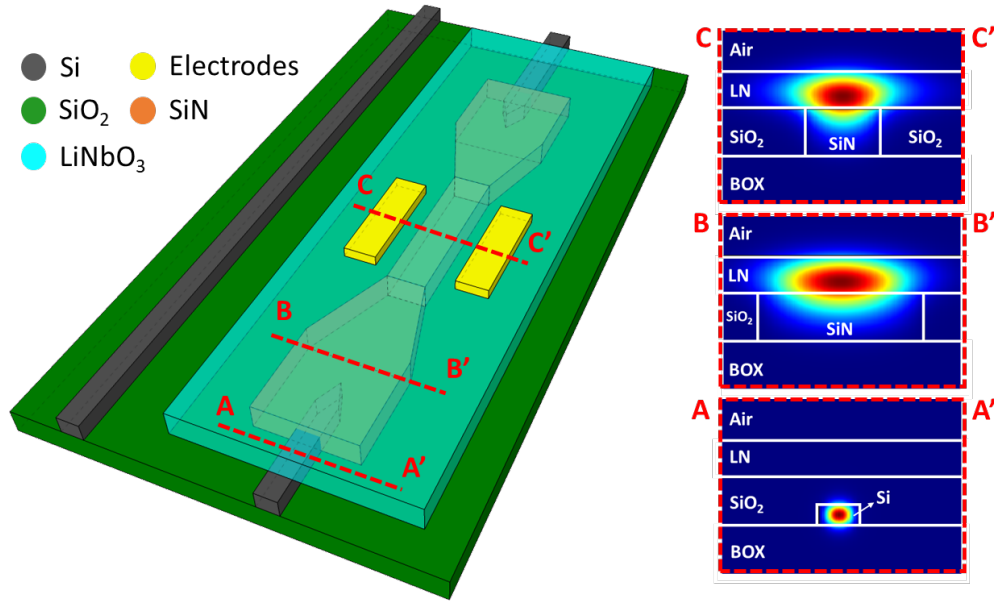


Figure 2.5: A novel approach for heterogeneous integration of TFLN with SOI waveguides is shown. The SiN intermediate layer serves as the adiabatic mode converter from SOI to the LN region (from AA' to BB'), as well as the rib for the hybrid SiN-LN waveguide. The optical mode simulation at different cross-sections of the structure are shown on the right. The SiN width can be optimized for achieving the desired optical mode confinement in TFLN [117].

Table 2.1: State of the art in propagation loss for various TFLN platforms of Figure 2.3.

TFLN Platform	Waveguide Loss [dB/cm]	Reference
Rib-loaded	0.3	[91]
Dry-etched	0.027	[44]
Proton-Exchanged	0.2	[50]
SOI-bonded	0.3	[48]

2.3 Electrooptic Modulators on TFLN

There is a host of different applications for high-performance TFLN EOMs. These include optical electric-field sensors [119], analog and digital optical links for telecommunication systems [120], and optical interconnects [121] in high-capacity data centers, EO-based frequency comb generation [99, 122] for LiDAR, integrated spectroscopy [123], millimeter-wave imaging [124], and high-performance computing for optical neural networks [125], as well as quantum technologies [126]. Some applications in visible-wavelength photonics include molecular spectroscopy and

biophotonics [127, 128].

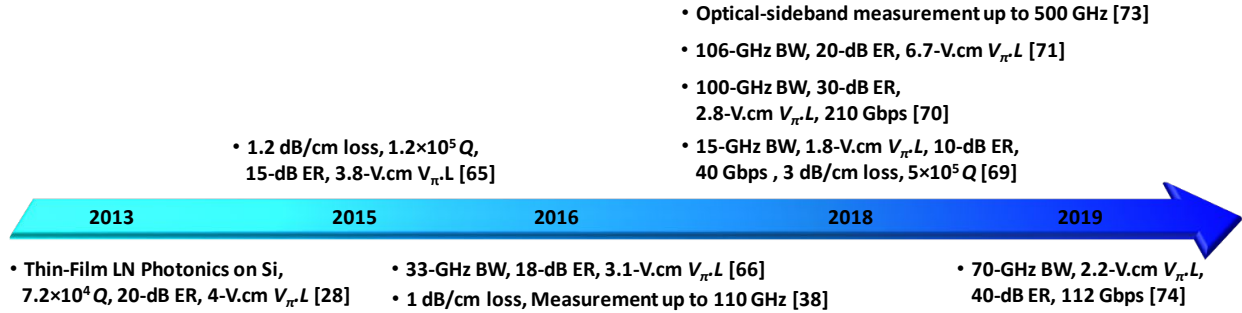


Figure 2.6: The timeline presents recent progress in TFLN EOMs in terms of key performance parameters, namely, LN waveguide propagation loss, 3-dB modulation BW, ER, and $V_{\pi} \cdot L$ at low frequencies. Q denotes the quality factor of TFLN microrings. The figure represents significant achievements in TFLN EOM technology and is not all-inclusive.

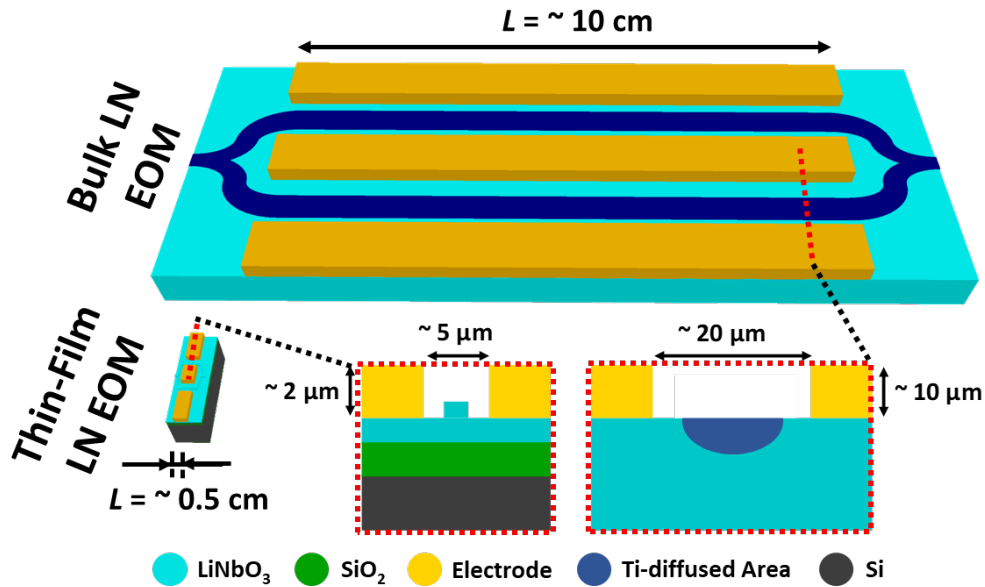


Figure 2.7: Comparison between conventional bulk LN versus ultracompact TFLN MZ EOMs. The 3-D schematics are drawn to scale, in order to emphasize the significant reduction in the device footprint. The 2-D device cross-sections are not in scale. By utilizing the highly-compact optical mode in the TFLN case, the gap between the metallic electrodes can be decreased without inducing additional optical loss which results in lower $V_{\pi} \cdot L$ values compared to its bulk counterpart.

In this section, we provide a brief chronological review of the recent advancements for TFLN EOMs. Figure 2.6 summarizes the main achievements in terms of key performance param-

eters, i.e., propagation loss, BW and ER. The comparison between the conventional and ultracompact LN EOMs are depicted in Figure 2.7.

As mentioned in Section 2.2, TFLN on LN substrates was demonstrated in 2004 [29]. Later on [112], it was shown that the material properties of bulk LN are preserved in TFLN platform, and an EOM with $V_{\pi} \cdot L$ of 15 V.cm and 15-20 dB/cm propagation loss was demonstrated for direct-etched Z-cut TFLN waveguides at 1550 nm wavelength. In BCB-bonded Z-cut TFLN, direct-etched microrings with quality factors, Q , of $10^3 - 10^4$ were demonstrated in [58] and [20], respectively, and propagation loss as low as 7 dB/cm were reported [20].

In 2013, our group at CREOL demonstrated the first wafer-scale TFLN on Si substrates [28]. The fabrication process for such wafers are summarized in Figure 2.2. By rib-loading the obtained TFLN with tantalum pentoxide (Ta_2O_5), MZ EOMs with remarkable $V_{\pi} \cdot L$ of 4 V.cm and 20 dB ER were attained. Decent propagation loss of 5 dB/cm, and a Q of $\sim 7.2 \times 10^4$ were also demonstrated for microrings. Moreover, by using the Y-cut TFLN, the largest EO coefficient of LN (r_{33}) was utilized by applying a lateral electric field along the Z-axis. In an improved report [65], by rib-loading the same platform with ChG, MZ EOMs with $V_{\pi} \cdot L$ of 3.8 V.cm and gigahertz-range operation were demonstrated. Also, the propagation loss was reduced to 1.2 dB/cm and microrings with Q of $\sim 1.2 \times 10^5$ were reported.

Ultracompact TFLN waveguides with propagation loss as low as 0.2 dB/cm are achieved by Cai *et al.* [50], by utilizing the mature PE process from bulk LN technology and applying it to the LNOI platform. This value was on par with the best propagation loss reported for conventional LN waveguides. However, as mentioned in Section 2.2.2, weak optical confinement and large bending radii of this platform impede ultracompact EOMs.

Our group reported on high-speed TFLN EOMs in 2016 [66]. Characterized up to 50 GHz, the devices demonstrated 33-GHz 3-dB BW, $V_{\pi} \cdot L$ of 3.1 V.cm, and 18-dB ER in 8-mm-long devices (see Figure 2.8a). PECVD- Si_3N_4 was used for rib-loading the Y-cut TFLN, and waveguides with propagation loss of 1 dB/cm were reported.

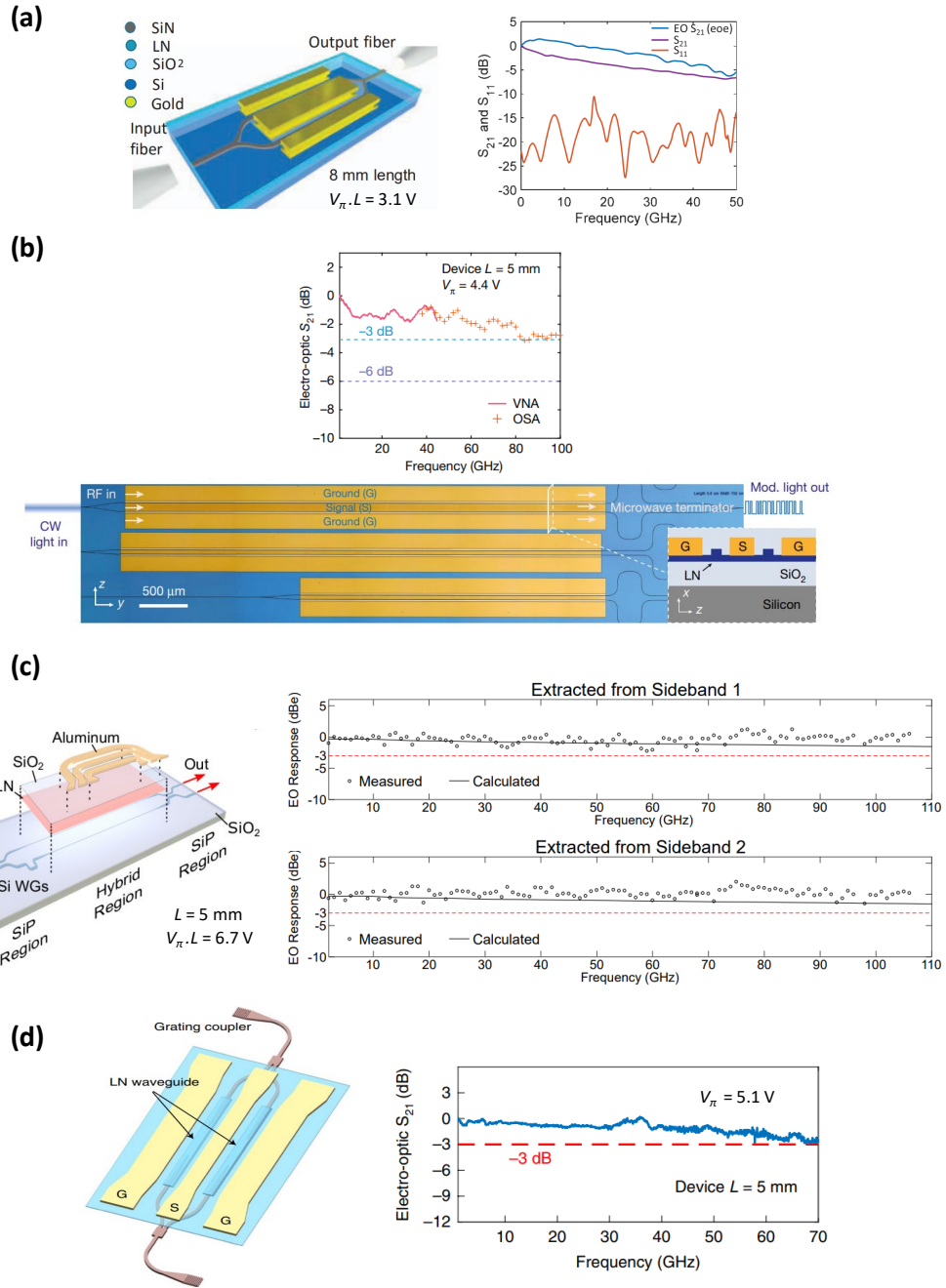


Figure 2.8: Examples of recent high-performance TFLN MZ EOMs on Si [66, 70, 71, 74]: (a) 18-dB ER, and 33-GHz BW. Reproduced with permission from [66]; (b) 30-dB ER, and 100-GHz BW. Reproduced with permission from [70]; (c) 20-dB ER, and 106-GHz BW. Reproduced with permission from [71]; (d) 40-dB ER, and 70-GHz BW. Reproduced with permission from [74]. L is the modulation length. Values for V_{π} , and ER are reported at low frequencies.

In the same year, Mercante *et al.* [38] demonstrated a 10-mm-long TFLN phase modulator on Si substrate with ~ 40 -GHz BW and ~ 1 -dB/cm waveguide propagation loss. The fabrication of the device included less-favored approach of mechanical thinning an X -cut LN film and bonding it to Si substrate using an adhesive polymer. Nonetheless, careful RF design of the EOM (reducing the impedance and RF and optical index mismatch by partially etching the LN layer at the waveguides region and decreasing the thickness of the LN which possesses a large dielectric constant) ensured high-speed operation up to 110 GHz.

In 2017, Zhang *et al.* [44] demonstrated microrings with Q values up to $\sim 10^7$, and propagation loss of 0.027 dB/cm on an X -cut TFLN on Si platform. This work among a few others later on [45, 47], were significant achievements in low-loss direct-etching of LN.

In 2018, we reported on detailed general transmission-line modelling, and design guidelines for ultracompact TFLN EOMs predicting 100-GHz BW [129]. The main shortcoming with the commonly employed models in the literature which had been originally developed for bulk device was the impedance matching, typically assumed, between the EOM's transmission line properties and the terminating resistive load at all modulation frequencies. This was proved to not be applicable to compact EOMs. By comparison with our previous experimental data [66], we showed that our EO modelling [129] is capable of accurate prediction of the device's EO response. Additionally, by optimization of device parameters, the model predicted that 100-GHz 3-dB BW is attainable in such ultracompact devices.

Later that year, Wang *et al.* [70] reported MZ EOMs with 100-GHz BW, 30-dB ER, $V_{\pi} \cdot L$ of 2.2 V.cm, and insertion loss of < 1 dB in 5-mm-long devices on direct-etched X -cut TFLN on Si platform (see Figure 2.8b). Direct CMOS-driven modulation at 70 Gbit/s was demonstrated on 20-mm-long devices with ~ 45 -GHz BW. Higher modulation speeds up to 210 Gbit/s were also presented with bit-error-ratio (BER) of 1.5×10^{-2} .

Also, Weigel *et al.* [71] reported on > 106 -GHz BW, 20-dB ER, $V_{\pi} \cdot L$ of 6.7 V.cm, and 7.6-dB insertion loss in 5-mm-long EOMs on a direct-bonded X -cut TFLN on to SOI waveguides (see

Figure 2.8c). The 3-dB BW reported in this work is the highest experimentally demonstrated value up to date. The same group has recently showed 20 Gbit/s data modulation with eye-diagrams and signal-to-noise ratio measurements up to 102 GHz [72].

In another TFLN EOM demonstration in 2018, Mercante *et al.* [73] demonstrated a direct-etched TFLN phase modulator on quartz substrate. The devices exhibited ~ 7 -dB/cm propagation loss, and were characterized up to 500 GHz by optically-assisted methods. The 3-dB RF BW of this work, however, is limited to below 10 GHz.

While ~ 100 GHz remains the highest experimentally-demonstrated BW to date [70, 71], we have recently reported on detailed optical and RF design techniques, which proves that up to 400-GHz 3-dB BW is attainable in ultracompact TFLN EOMs [116]. Such unprecedented BWs could find tremendous interest in a variety of system applications mentioned at the beginning of this section.

More recently, He *et al.* [74] have demonstrated TFLN MZ EOMs with 70-GHz BW, and $V_{\pi} \cdot L$ of 2.55 V.cm in 5-mm-long devices (see Figure 2.8d). $V_{\pi} \cdot L$ of 2.2 V.cm and ER of 40 dB and more are reported for 3-mm-long EOMs. Also, eye diagram measurements and BER values have been reported for high-speed modulations up to 112 Gbit/s. So far, the ER and $V_{\pi} \cdot L$ of this work are the best values reported for TFLN EOMs to date. However, it is worth mentioning that, recently, by cascading two TFLN MZ EOMs higher ER (up to 53 dB) has been demonstrated [130]. The devices in [74] are fabricated by using a BCB-bonding method of TFLN to SOI waveguides, as depicted in Figure 2.4. In addition, direct-etching of LN is also employed (see Figure 2.3h) in order to fully transfer the optical mode from SOI to LN waveguides in the modulator region compared to the partially-transferred optical mode in [71]. Clearly, more optical confinement in LN leads to an improved EO performance in the TFLN EOMs. This optical mode transitions are carried through vertical adiabatic couplers. The measured optical loss for each coupler is ~ 0.19 dB, and the overall insertion loss of the EOM is 2.5 dB. More recently, the same group has reported on a Michelson interferometer modulator on the same platform with 17.5-GHz BW, 30-dB ER, and

a low $V_{\pi} \cdot L$ of 1.2 V.cm in 1-mm-long devices [78] .

It is also worthwhile mentioning that there are only few work among TFLN EOMs, which report on linearity for analog applications [64, 66, 74, 79]. Spurious-free dynamic range (SFDR) is a figure of merit for measuring the linearity of EOMs in microwave photonics [110]. Values from ~ 90 to ~ 100 dB.Hz^{2/3} have been reported in these four TFLN work [64, 66, 74, 79], which are still inferior to the best values reported for bulk LN EOMs (~ 120 dB.Hz^{2/3}) [131]. Hence, it is expected that more works could emerge to improve SFDR of TFLN EOMs.

In summary, a comparison between the main performance parameters of the MZ EOMs discussed in this work is presented in Table 2.2.

For completeness, we mention that compact TFLN EOMs are not limited to MZ or phase modulators. Another type is resonance-based devices such as microring modulators (MMs). In principal, they can be formed on any of the platforms depicted in Figure 2.3. While they offer smaller device footprint, they are usually more prone to fabrication errors compared to other type of EOMs and provide less BW. The main figures of merit for MMs are Q , tunability, i.e., the amount of spectral shift in microring's optical resonance per applied electrical field, ER, and 3-dB BW. A summary of reported TFLN resonance-based devices are presented in Figure 2.9 and Table 2.3.

Table 2.2: Summary of performance parameters for TFLN MZ EOMs. BW denotes the 3-dB electrical modulation BW. $V_{\pi} \cdot L$, and ER are at reported values at low frequencies. The values inside the parenthesis represent the reported measurements for another device in the same work.

TFLN Platform (Year)	$V_{\pi} \cdot L$ [V.cm]	V_{π} [V]	L [mm]	BW [GHz]	ER [dB]	Reference
Dry-etched (2005)	15	42.8	3.5	N/A	N/A	[112]
Rib-loaded (2013)	4	6.8	6	N/A	20	[28]
Rib-loaded (2015)	3.8	6.3	6	1	15	[65]
Rib-loaded (2016)	3	2.5	12	8	13.8	[67]
Rib-loaded (2016)	3.1	3.87	8	33	18	[66]
Dry-etched (2018)	1.8	9	2	15	10	[69]
Dry-etched (2018)	2.2 (2.8)	4.4 (1.4)	5 (20)	100 (45)	N/A (30)	[70]
SOI-bonded (2018)	6.7	13.4	5	>106	20	[71]
Ti-diffused (2019)	7.2	1.2	60	20	40	[51]
SOI-bonded (2019)	2.55 (2.2)	5.1 (7.4)	5 (3)	70 (>70)	N/A (40)	[74]
SOI-bonded (2019)	2.5	2.5	10	50	16	[77]
Rib-loaded (2020)	6.7	13.4	5	30.6	20	[79]

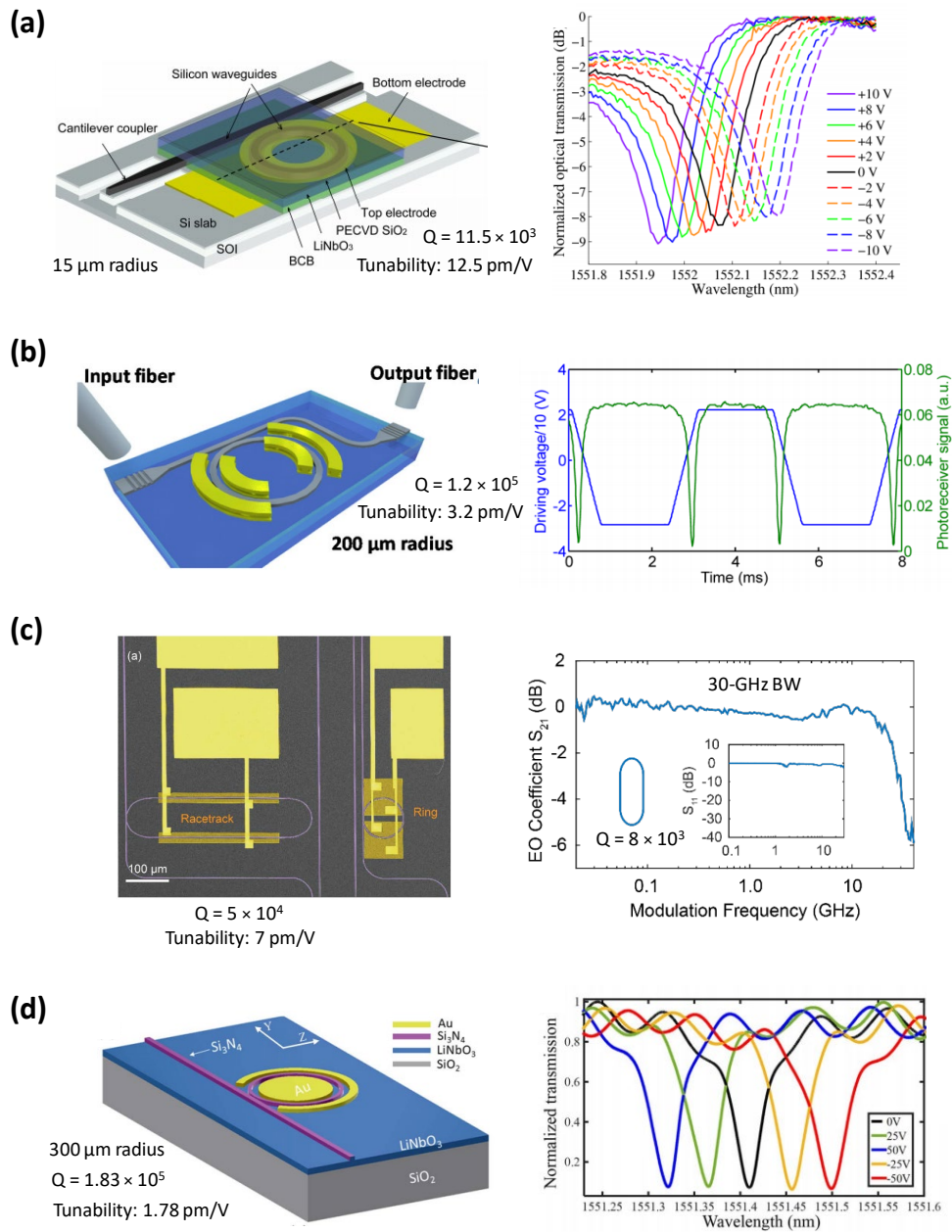


Figure 2.9: Examples of recently-demonstrated TFLN resonance-based EOMs [62, 65, 69, 76]: (a) BCB-bonded LN-SOI microring. Reproduced with permission from [62]; (b) Rib-loaded LN-on-Si microring. Reproduced with permission from [65]; (c) Dry-etched LN-on-LN microring. The racetrack resonator exhibits 3-dB BW of 30 GHz. Reproduced with permission from [69]; (d) Rib-loaded LN-on-quartz microring. Reproduced with permission from [76].

Table 2.3: Summary of performance parameters for TFLN resonance-based EOMs. R and BW denote the radius, and 3-dB electrical modulation BW, respectively. The values for ER are at low frequencies.

TFLN Platform (Year)	Q	Tunability [pm/V]	R [μm]	ER [dB]	BW [GHz]	Reference
SOI-bonded (2007)	4×10^3	1.05	100	7	N/A	[58]
SOI-bonded (2011)	1.68×10^4	1.7	6	5	N/A	[36]
SOI-bonded (2013)	1.15×10^4	12.5	15	8	N/A	[62]
SOI-bonded (2014)	1.2×10^4	3.3	15	10	5	[63]
Rib-loaded (2015)	1.2×10^5	3.2	200	13	N/A	[65]
Dry-etched (2018)	8×10^3	7	N/A	N/A	30	[69]
Rib-loaded (2019)	1.85×10^5	1.78	300	27	N/A	[75]

2.4 Nonlinear Optics on TFLN

Another widespread application domain for LN is nonlinear integrated photonic due to its high second-order nonlinear coefficient ($d_{33} = 30$ pm/V). Titanium in-diffusion [18] and proton exchange [19] have been the most commonly employed techniques in order to form LN waveguides, as previously discussed in Section 2.2.2. However, various limitations arise in these waveguides, which limit their performance and applicability to nonlinear integrated photonics. Low index contrast of the waveguide is a fundamental drawback that yields in a large cross-section and small overlap between the interacting modes. This limits the device performance due to high pump power required for the onset of second-order nonlinearity. On the other hand, large-scale integration can not be achieved with such devices due to their large device footprint.

TFLN platform is an excellent alternative that avoids the limitations of the predecessor approaches and demonstrates more compact and more efficient nonlinear integrated devices. On this platform, by employing rib-loading (see Figure 2.3a) [90, 91], or direct-etching (see Figure 2.3b) [92, 95] methods, high index contrast and hence tight optical mode confinement, efficient modal overlap integral, and ultrahigh nonlinear conversion efficiency can be achieved. A variety of efficient nonlinear integrated devices have been recently demonstrated on this platform by various research groups, as elaborated in this section.

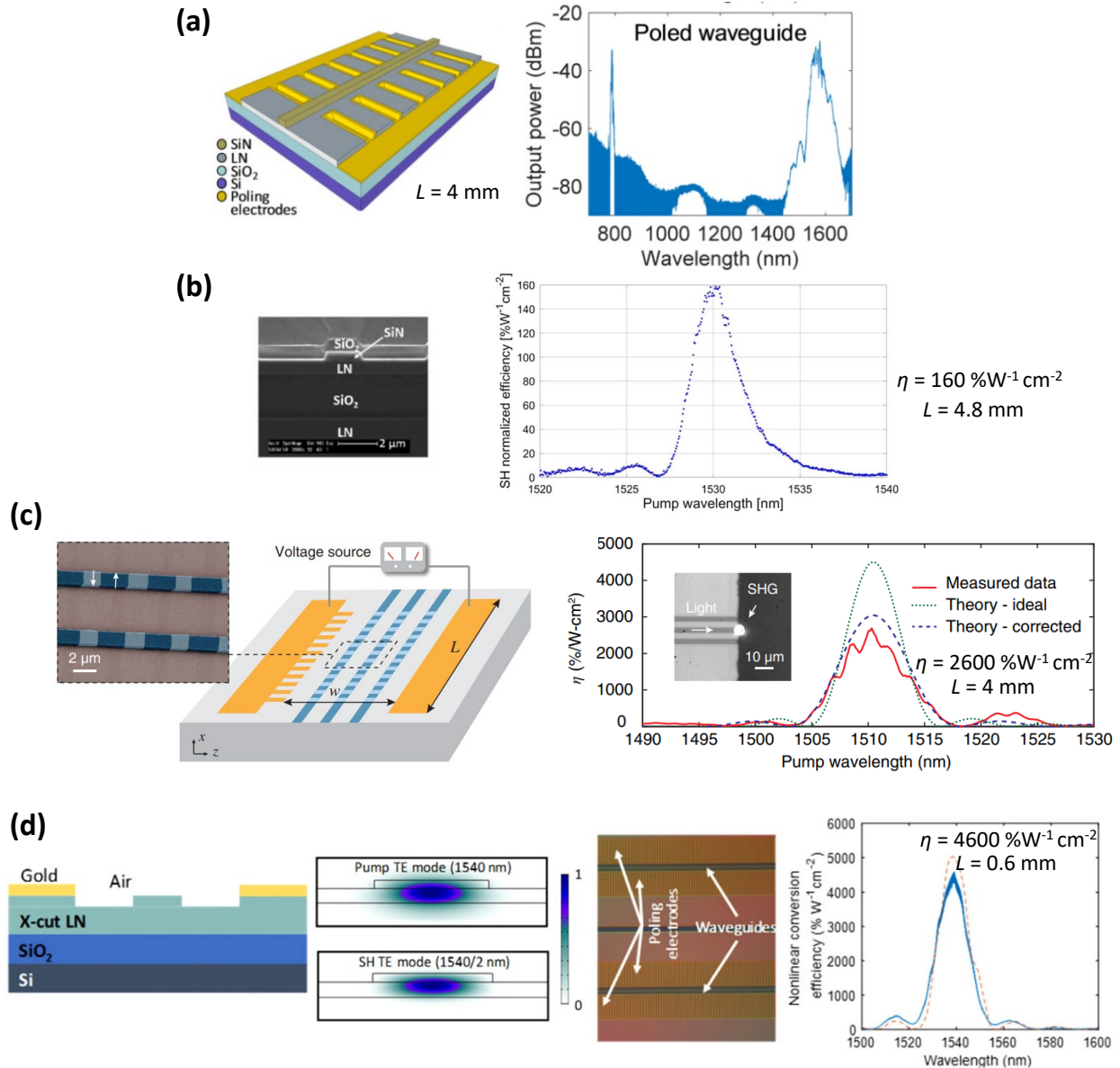
2.4.1 Periodically-Poled TFLN Waveguides

Following the development of the TFLN technology, first periodically poled lithium niobate (PPLN) waveguides were demonstrated in 2016 using TFLN on Si and TFLN on LN platforms [90, 91]. PPLN waveguides are conceptually wavelength converters that can be utilized for a variety of nonlinear processes such as, second-harmonic generation (SHG), difference-frequency generation (DFG) or sum-frequency generation (SFG). In principal, quasi-phase matching (QPM) is achieved in PPLN waveguides through inverting the crystalline domain polarity periodically to compensate for the wave-vector mismatch Δk between the pump and SHG optical modes. This has been historically realized in bulk PPLN by applying an electric field higher than the coercive (threshold) field value of ~ 21 kV/mm [132]. The same concept is used in TF-PPLN, but with higher threshold field value of $\sim 30 - \sim 50$ kV/mm. This higher required electric field can be attributed to the bonding interface between the TFLN and the SiO₂ insulating layer or the out-diffusion of Li⁺ during annealing step of the TFLN wafer fabrication process [91, 133].

A 3-D schematic diagram of the PPLN device on Si is shown in Figure 2.10a with a SiN rib-loaded waveguide on Si substrate [90] along with optical mode simulation of the pump and SHG. This waveguide demonstrated 8% nonlinear conversion efficiency with pulsed laser pump around 1550-nm wavelength. A cross-section of TF-PPLN waveguide on LN substrate [91] is shown in Figure 2.10b with reported normalized nonlinear conversion efficiency of $160 \text{ \%W}^{-1}\text{cm}^{-2}$ in 4.8-mm-long device using continuous-wave pump around 1530-nm wavelength. This efficiency is more than 4 times larger than the typical values in conventional PPLNs, yet one order of magnitude less than the theoretical value, which can be attributed to the imperfections of the periodic domain duty cycle and non-uniformities of the fabricated waveguide. This stresses the importance of the poling process for optimizing the conversion efficiency.

As previously discussed in Section 2.2.2, dry etching *X*- and *Y*-cut LN waveguides have been historically challenging, however, various research groups have recently reported successful

etching processes with low propagation loss [44]–[47], [92, 95].



These demonstrations have opened the door wide for realization of ultrahigh efficient TF-

PPLN waveguides. Such a process has been first used to fabricate a 4-mm long PPLN waveguide, shown in Figure 2.10c, with normalized conversion efficiency of $2600 \text{ \%W}^{-1}\text{cm}^{-2}$ [92]. By utilizing an active iterative poling technique, our group at CREOL has recently demonstrated record-high $4600 \text{ \%W}^{-1}\text{cm}^{-2}$ normalized efficiency in 0.6-mm-long devices [95], as shown in Figure 2.10d. This efficiency is the highest reported normalized conversion efficiency to date and very close to the theoretical limit calculated for this type of waveguides. The TF-PPLN waveguides discussed above are summarized in Table 2.4.

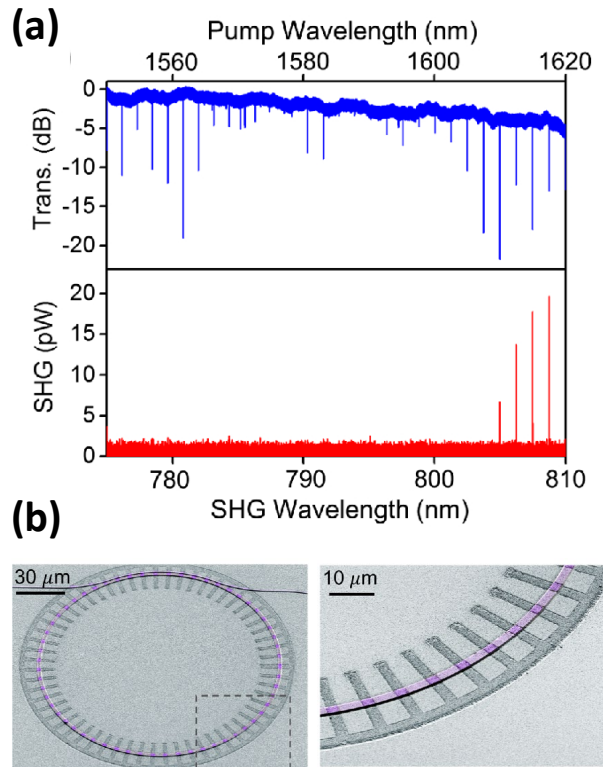


Figure 2.11: Demonstration of efficient SHG in PPLN microring resonators: (a) SHG signal (red), when TE-polarized pump laser is swept across the telecom band (blue); (b) False color SEM images of the etched device in hydrofluoric acid. Reproduced with permission from [97].

In addition to standard PPLN devices, SHG has also been recently reported in *X*-cut and *Z*-cut PPLN microring resonators, with normalized conversion efficiency of $230,000 \text{ \%}/W$ [96] and $250,000 \text{ \%}/W$ [97], respectively. This method has been achieved through careful design of a

doubly-resonant device at the pump and the SHG wavelength using a single pulley waveguide. An example of such devices in Z-cut TFLN with the measured SHG spectrum is shown in Figure 2.11, while the pump laser is swept across the telecom band. Further optimization to decrease the propagation loss and increase the efficiency of these devices may enable nonlinearity at single-photon level, which will pave the path for interesting quantum-photonic applications such as deterministic entanglement generation and control-NOT gate for single photons [96].

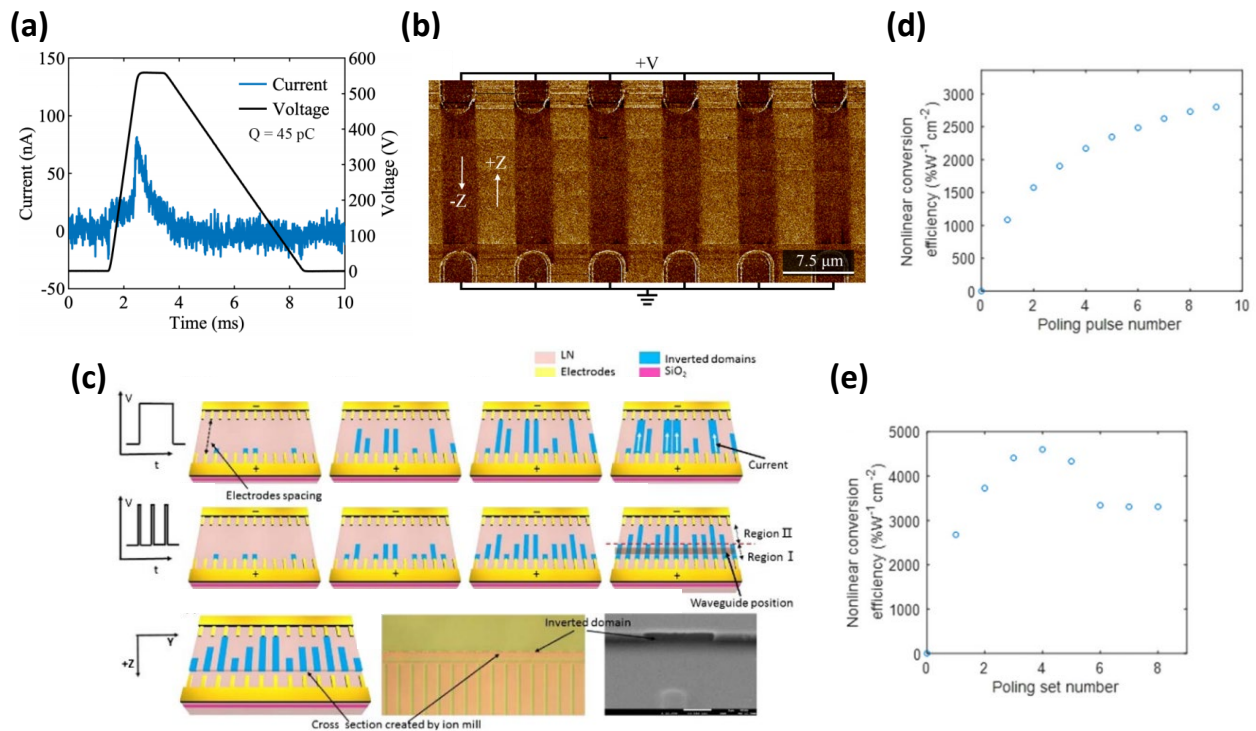


Figure 2.12: Periodic poling of TFLN waveguides: (a) Example of poling pulse for TF-PPLN along with (b) piezoresponse force microscope image of the resulting periodic domain. Reproduced with permission from [133]; (c) Schematic illustration of the evolution of inverted domain using a long poling pulse and multi-pulse waveforms with short pulse durations. Images of the device are obtained after ion milling to visualize the periodically poled region. Reproduced with permission from [91]; Actively-monitored poling technique demonstrates increase of SHG efficiency with (d) the number of poling pulses and (e) the number of poling cycles, used for ferroelectric domain inversion (see Figure 2.1b). Reproduced with permission from [95].

Periodic poling by means of electric field is a powerful technique for domain inversion of ferroelectric materials, in order to achieve quasi-phase matching (QPM) for second-order ($\chi^{(2)}$)

nonlinear processes. It does not suffer from drawbacks such as shallow inverted layers as in the chemical diffusion technique or axial variation in domain periodicity in the crystal growth technique [132]. LN domain polarity is determined by the relative position of the metal ions (Li and Nb) to the oxygen layers and can be reversed by reorienting the crystal from one stable configuration to the other as depicted in Figure 2.1b. This can be achieved by applying an electric field higher than the coercive electric field of LN, which is ~ 20.5 kV/mm at room temperature. Electric-field-driven poling process can be divided into four successive steps: (1) nucleation centers formation at the positive electrode, (2) tip propagation or domain growth along the z -axis of the crystal, (3) domain walls propagation in lateral directions, i.e., x - and y - directions of the crystal, and (4) domains merging [134].

Table 2.4: Examples of recently-demonstrated TF-PPLN devices. η and L represent the normalized conversion efficiency, and the length of the poled region, respectively. CAR denotes the coincidence-to-accidental ratio measurements for on-chip photon-pair generation.

TFLN Platform (Year)	η [% W ⁻¹ cm ⁻²]	L [mm]	CAR	Reference
Rib-loaded (2016)	160	4.8	N/A	[91]
Rib-loaded (2016)	N/A	4	~ 300	[90, 102, 106]
Dry-etched (2018)	2600	4	N/A	[92]
Dry-etched (2019)	4600	0.6	~ 7000	[95, 103]
Dry-etched (2019)	2000	5	~ 67000	[105]
Dry-etched (2019)	2200	4	~ 600	[104]

Achieving 50% duty cycle and uniform periodicity are critical factors in determining the overall efficiency of the nonlinear device as previously discussed. Domain inversion in TFLN is usually realized through applying a square pulse or more efficiently a series of short pulses (~ 10 -20 ms) as in Figure 2.12c, depicting the evolution of the inverted domain in both cases. Employing a series of short pulses for poling guarantees formation of enough nucleation centers, complete inversion of the domain, periodic domain uniformity, and high poling yield. This also avoids temperature rising and domain merging due to sidewall propagation. An example of a poling pulse is shown in Figure 2.12a along with the piezoresponse force microscope image of the resulting

periodic domain Figure 2.12b with $\sim 50\%$ duty cycle and high yield [133].

Our group has recently demonstrated an actively-monitored iterative poling technique that enables higher efficiencies than usually achieved using conventional passive techniques [95]. It utilizes an optically-monitored iterative poling, depoling, and repoling sequence with a series of at least nine pulses in each poling cycle. The resulting efficiency measured during this process is shown in Figures 2.12d and 2.12e, which confirm increase of the efficiency with the number of poling pulses and poling cycles. More details of the periodic poling of TFLN waveguides and various methods in order to study and improve the domain inversion can be found in [95], and [133]–[136].

2.4.2 Other Approaches to Phase Matching in TFLN Waveguides

Other alternative approaches for phase matching have been successfully demonstrated for $\chi^{(2)}$ processes in TFLN, although with less conversion efficiency compared to PPLN method. Nonetheless, the advantage of these methods is that they are poling-free, hence fabrication and device preparation are simplified. Another advantage is that the techniques discussed in this section are not limited to ferroelectrics, and in principal, can be applied to other nonlinear materials [137]. Detailed mathematical derivations for different phase matching methods can be found in [111].

Grating assisted quasi-phase matching (GA-QPM) (or mode-shape modulation [138]) is an example of such alternatives, in which periodic spatial modulation of waveguide parameters is utilized in order to induce a periodic variation in the nonlinear overlap integral [138]–[140].

In Ref. [138] (see Figure 2.13a), our group applied GA-QPM to the TFLN platform by employing a sinusoidal width perturbation of the rib-loaded waveguides with SiN. SHG with $\sim 1\% \text{W}^{-1}\text{cm}^{-2}$ normalized conversion efficiency was demonstrated in 4.9-mm-long waveguides at 784 nm wavelength. An optimized width modulation pattern and a higher-refractive-index rib material can increase the conversion efficiency of such devices.

We have also reported on random QPM based on the GA-QPM technique and demonstrated

SHG at 775-nm wavelength [140]. As shown in Figure 2.13b, the periodicity of the sinusoidal modulation of waveguide's width (created by dry etching TFLN) is chosen randomly. Random QPM has the benefit of overcoming the intrinsic bandwidth limitations imposed by uniform periodic perturbation.

In modal phase matching (MPM), a multi-mode waveguide is designed so that the wavevector of the mode at pump wavelength is matched with the wavevector of one of the higher order modes at SHG wavelength [139, 141]. Wang *et al.* [139] reported on MPM and GA-QPM on TFLN platform and demonstrated SHG with 41 and 6.8 $\%W^{-1}cm^{-2}$ normalized conversion efficiency, in 1-mm-, and 0.5-mm-long waveguides, respectively. For the MPM case, first- and third-order transverse-electric (TE) modes of a waveguide with fixed width (see Figure 2.13c) were phase matched, while a periodically-grooved structure is used for GA-QPM, as depicted in Figure 2.13d. While MPM waveguides offer higher conversion efficiency and a simpler fabrication process than the GA-QPM counterpart in this work, the GA-QPM method benefits from fundamental mode operation at both pump and signal wavelengths, similar to the PPLN devices in the previous section.

In general, the utilization of higher order modes have the drawbacks of less confinement and less overlap integral between the interacting optical modes. This results in higher propagation loss due to waveguide sidewall roughness and lower nonlinear efficiency. It is worth mentioning that for the case of microresonators, in addition the MPM method [142], other techniques for phase matching have been also demonstrated, e.g., cyclic phase matching [143].

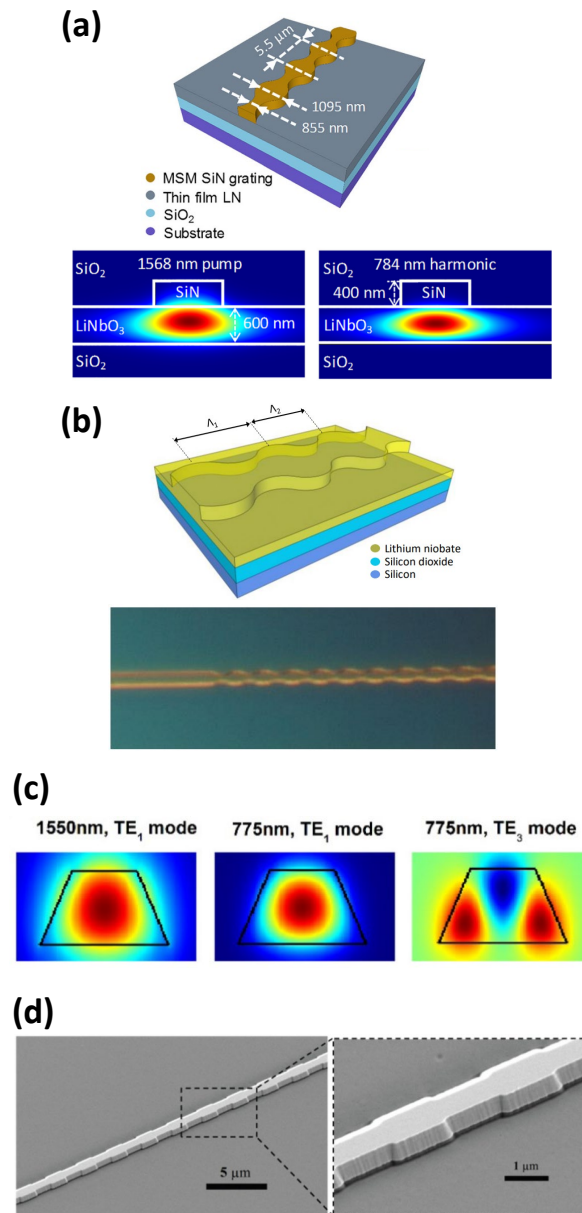


Figure 2.13: Demonstration of poling-free methods [138, 140, 139] for SHG in TFLN platform: (a) 3-D schematic of a rib-loaded GA-QPM waveguide with a sinusoidal modulation of the width along with the optical mode profiles of the fundamental and second-harmonic TE modes at a grating width of 1095 nm. Reproduced with permission from [138]; (b) 3-D schematic of a random QPM waveguide on a dry-etched TFLN platform along with a micrograph of the fabricated device. Reproduced with permission from [140].; (c) Optical mode profiles of the first- and third-order TE modes at the pump and second-harmonic wavelengths for MPM; (d) SEM image of the fabricated GA-QPM structure. (c) and (d) are reproduced with permission from [139].

In another interesting poling-free MPM approach for SHG in TFLN platform, Luo *et al.* [144] have employed a heterogeneous TiO₂-LN waveguide structure, and demonstrated 36 %W⁻¹ conversion efficiency corresponding to 650 %W⁻¹cm⁻² normalized efficiency in 2.3-mm-long waveguides at 775-nm wavelength.

By combining the thermo-optic birefringence property of LN with MPM, the same group have demonstrated tunable SHG in TFLN platform with 0.84 nm/K tunability for a telecom-band pump with 4.7 %W⁻¹ conversion efficiency in 8-mm-long waveguides [145].

2.4.3 Other Nonlinear Applications of TFLN Waveguides

Applications of TFLN nonlinear devices include frequency metrology, coherent optical communication links between the telecom and visible bands, optical frequency synthesizers, compression of ultrashort pulses required for studying solid-state material properties, frequency comb generation in LiDAR, and mid-infrared spectroscopy [7, 22, 95, 146]. The high amount of optical power used in certain nonlinear applications can induce optical damage to the TFLN crystal. This can be mitigated by employing adequate Magnesium Oxide (MgO) doping in TFLN similar to bulk LN crystals [147]. In this section, we present the different classical nonlinear applications whereas the quantum applications will be summarized later in Section 2.5.

SHG is the most straight forward nonlinear application of TFLN waveguides. As discussed earlier, TFLN platform has achieved ultrahigh efficient SHG devices. Difference-Frequency Generation (DFG) and Sum-Frequency Generation (SFG) are similar nonlinear applications that have been successfully demonstrated as well in TFLN waveguides. DFG has been recently reported in X-cut TF-PPLN waveguides with bandwidth more than 4.3 THz [104] and TFLN microdisks [148]. SFG has also been demonstrated by different groups either in TFLN waveguides [95, 149] or TFLN microdisks [56, 150].

LN is a non-centrosymmetric material with small $\chi^{(3)}$ coefficient compared to its $\chi^{(2)}$. However, effective four-wave mixing, i.e., Kerr nonlinearity, has been recently reported through

cascaded SHG-DFG process in TFLN microdisk [151]. Third- [95], [152]–[155] and fourth- [95, 152, 153] harmonic generation have also been observed through similar cascaded nonlinear processes. Cascaded nonlinearity has enabled multi-octave supercontinuum generation in dispersion-engineered LN [93] and PPLN waveguides [101]. By employing high- Q microrings, Kerr frequency comb generation has also been demonstrated on the TFLN platform [100, 156, 157]. Second- and third-harmonic generation have been also recently reported in high- Q 2-D photonic crystals in X -cut TFLN [158].

In addition to standalone nonlinear devices on TFLN platform, cascaded heterogeneous integration of other materials with higher $\chi^{(3)}$ nonlinearity, such as SiN and ChG, have been also pursued [40, 113, 159]. In [113], we have addressed the fabrication challenges of cascaded integration of such materials by employing low-loss mode-converting tapers. This work paves the path towards providing efficient platform in order to realize multiple nonlinearity, i.e., large $\chi^{(2)}$ of LN and high $\chi^{(3)}$ of ChG, on a single Si chip with applications like stabilized comb generation through f -to- $2f$ carrier envelope offset (CEO) locking.

In another application of TF-PPLN waveguides, we have recently employed our highly-efficient devices accompanied with spectral filtering, to build wide-band non-magnetic linear optical isolators with potential for monolithic integration of the whole system on a single chip [160]. This work could add an important piece to the component library of PICs, which enables building complete systems out of this platform only.

2.5 Quantum Optics on TFLN

Integrated quantum photonic is an emerging field with promising applications in quantum computing and quantum optical communication [161, 162]. The TFLN platform is a suitable candidate with a high potential for realization of complex quantum PICs due to its superior nonlinear and EO properties. This enables the generation and manipulation of non-classical light on chip [163].

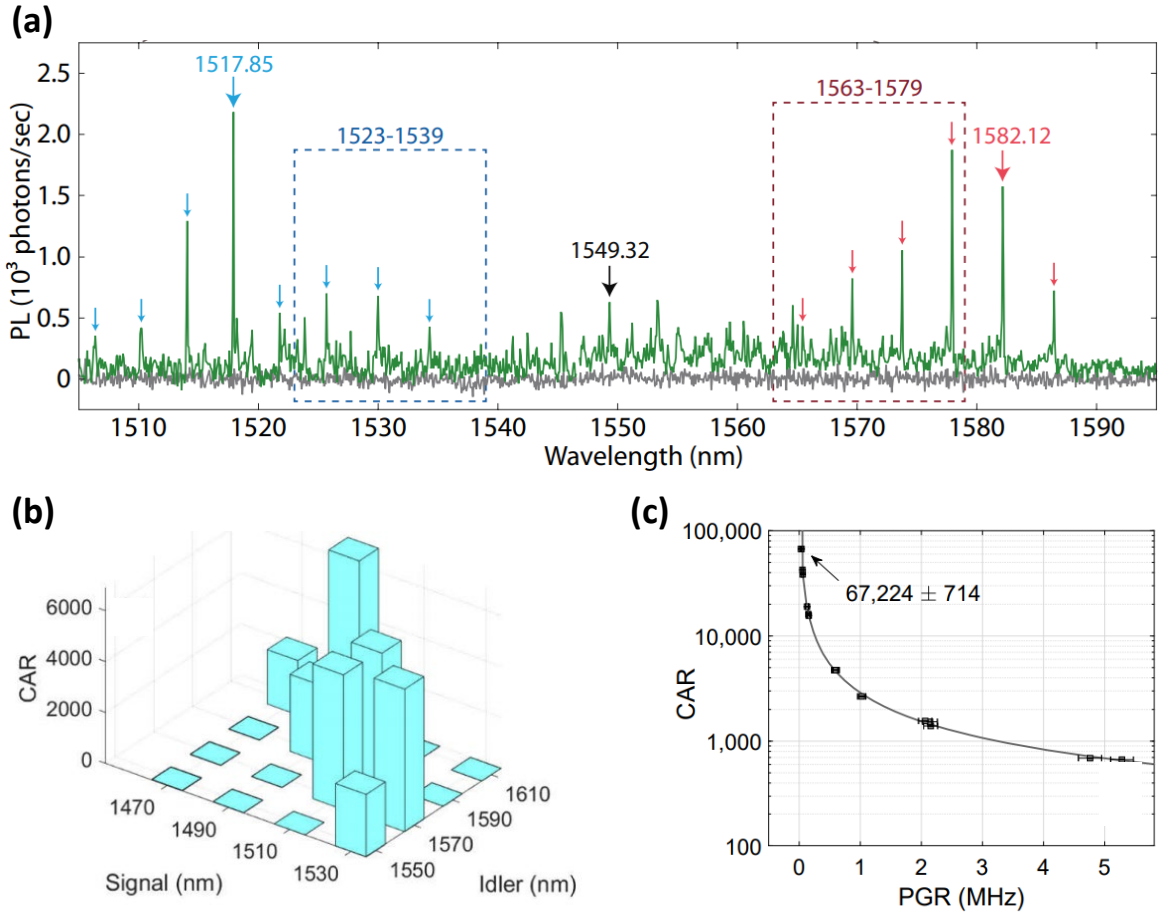


Figure 2.14: Examples of photon-pair generation demonstrated in TFLN platform: (a) Wide-band (up to 400 nm) SPDC spectrum. Reproduced with permission from [143]; (b) CAR values of up to 7000 with more than 120-nm signal-idler channel separation. Reproduced with permission from [103]; (c) CAR values > 67000 at 82 kHz pair generation rate. Reproduced with permission from [105].

The first entangled photon pair sources in TF-PPLN on Si, based on the spontaneous parametric down conversion (SPDC) process, was demonstrated in 2018 [102, 106]. Pumped with a Ti-sapphire laser at 792 nm, with < 0.5 ps pulse-width, and a repetition rate of 81.8 MHz, on-chip photon pair generation with rate of ~ 1 MHz/mW and a coincidence-to-accidental ratio (CAR) of 15 were demonstrated [102]. By utilizing a time-of-flight fiber spectrometer, we were able to spectrally resolve the second-order coherence of photon pairs on the same chip with CAR values of > 300 [106]. More recently, by using the aforementioned highly-efficient TF-PPLN devices

[95], broadband correlated photon-pair was generated in 300 μm -long-PPLN waveguides with a signal-idler channel separations of ~ 140 nm and CAR around 7000 [103] (see Figure 2.14b). This work paves the path towards wide and continuous on-chip pair-matching for high channel capacities. Reducing the input/output coupling loss and improved filtering can result in much higher heralding efficiencies than the 3% reported in this work.

By incorporating longer TF-PPLN waveguides (5-mm-long poled region), Zhao *et al.* [105] have recently reported on CAR values > 67000 with 82 kHz generation rate, as depicted in Figure 2.14c. CAR values of the discussed work in this section are summarized in Table 2.4.

Figure 2.14c presents demonstrations of photon-pair generation in TFLN microdisks [143]. This device demonstrated a potential SPDC bandwidth over 400 nm inferred from the spectral measurements and a coincidence-to-accidental ratio (CAR) of 43. It is noted that due to the resonance-based operation of microdisks, the generated signal-idler pair spectrum is discrete whereas TF-PPLN devices are able to provide a continuous broadband spectrum which can be divided into various channels [103].

We need to stress that integrated quantum photonics on TFLN platform is a still a young field with great potential but few reports to date. For discussion of previous work for conventional bulk LN waveguides, we refer the readers to the review in [164]. It is expected that fully-integrated quantum chips, such as those reported for conventional LN waveguides [163, 165], will be realized in the near future in TFLN platform with higher performance than their conventional LN counterparts due to improved modes confinement and smaller waveguide cross-sectional area.

2.6 Roadmap Ahead

In general, further improvement in terms of fiber-to-chip interface coupling [83]–[89], careful consideration of electrical, RF, and optical packaging, and thermal/temporal reliability and stability studies are expected to be achieved soon for commercialization of fully-packaged TFLN devices.

Heterogeneous integration of active elements such as lasers, amplifiers, and photodetectors along with various TFLN components on single photonic chip is another front which is expected to attract extensive research for a host of applications such as optical communication transceivers, high-performance computation, analog, digital, and quantum communication links, and LiDAR systems. In this regard, back end of line heterogeneous integration with SOI and SiN photonic circuitry seems to be the most anticipated scheme to be pursued for low-cost, large-scale, and foundry-compatible deployment of TFLN devices.

With such high levels of maturity for TFLN platform, the following advancements are expected to be achieved for each application reviewed in this work.

For the case of EOMs, achieving modulation BWs beyond 100 GHz is one of the next steps required for advanced communication systems. Studies have shown promising pathways for subterahertz application of EOMs [73, 116]. However, it should be noted that full realization of integrated EOMs with such unprecedented BWs will require development of ultrahigh-speed electronic and photonic drivers and detection components as well. Another crucial milestone would be realization of higher modulation formats for coherent optical communication, which is yet to be demonstrated in TFLN platform.

Demonstration of nonlinear devices on TFLN with better performance is to be pursued in the near future, through decreasing insertion and propagation losses, achieving the optimum poling conditions for PPLN waveguides or increasing the efficiency of other phase-matched waveguides. Incorporating standalone nonlinear devices into more system-like applications, such as our optical isolators, is also a promising direction to be followed. Heterogeneous integration of $\chi^{(3)}$ materials onto TFLN and cascaded nonlinearity using this heterogeneous platform is also a promising direction that paves the path for a variety of interesting applications such as highly efficient high-harmonic generation, frequency-stabilized optical frequency combs and generation of mid-infrared wavelengths.

More complex quantum PICs for generation and manipulation of single- and entangled-

photon states are expected to be realized on LN. This is due to the fact that LN is combining linear (e.g., power splitters and combiners, wavelength division multiplexers), nonlinear (SHG and SPDC) functions and fast EO modulation. Entangled photon states, such as tripartite Greenberger-Horne-Zeilinger (GHZ), may also be attained in TFLN platform through cascading nonlinear devices on the same platform, with optimized ultrahigh nonlinear efficiency to realize high generation rate of these non-classical states. other non-classical applications such as entanglement swapping and heralded single photon sources with better efficiency are yet to be realized in TFLN. All of these demonstration will eventually enable the realization of quantum key distribution links, a crucial step for quantum secure communication.

2.7 Concluding Remarks

Diverse material features and excellent optical properties of LN have been extensively studied over the past decades. This versatile material has been one of the most attractive photonic platforms especially for electrooptic modulator and wavelength converter markets.

Recently, with the emergence of thin-film LN technology, the challenges and drawbacks of bulk LN have been overcome and standalone TFLN devices are outperforming their conventional bulk counterparts in terms of key performance parameters, such as waveguide propagation loss, modulation BW for EOMs, and conversion efficiency in the case of wavelength converters. In addition to performance boost, the TFLN technology is providing dramatic reduction in power consumption and overall device footprint in order to address the ever-increasing demands of large-scale integration in modern electronic-photonic systems.

In this paper, we have reviewed the most recent advancements of this flourishing technology. Key performance parameters of the main discussed applications, namely electro-, nonlinear-, and quantum-optics, are summarized in Table 2.2, Table 2.3, and Table 2.4. Thanks to successful commercialization of TFLN technology, a plethora of ultracompact photonic components and de-

vices have been demonstrated on this platform. The overall efforts have rejuvenated LN for the major photonic applications focused in this work, as well as other optical and RF/MEMS applications (see Figure 2.1a) not discussed here.

2.8 References

- [1] K. Nassau, “Early history of lithium niobate: personal reminiscences,” *Processing of Guided Wave Optoelectronic Materials I*, vol. 460, pp. 2–5, 1984.
- [2] R. Weis, and T. K. Gaylord, “Lithium niobate: summary of physical properties and crystal structure,” *Applied Physics A*, vol. 37, no. 4, pp. 191–203, 1985.
- [3] K. K. Wong, “Properties of lithium niobate,” *IET*, no. 28, 2002.
- [4] S. Fathpour, “Emerging heterogeneous integrated photonic platforms on silicon,” *Nanophotonics*, vol. 4, no. 1, pp. 143–164, 2015.
- [5] A. Bartasyte, S. Margueron, T. Baron, S. Oliveri, and P. Boulet, “Toward High-Quality Epitaxial LiNbO₃ and LiTaO₃ Thin Films for Acoustic and Optical Applications,” *Advanced Materials Interfaces*, vol. 4, no. 8, 2017.
- [6] E. L. Wooten, K. M. Kissa, A. Yi-Yan, E. J. Murphy, D. A. Lafaw, P. F. Hallemeier, D. Maack, D. V. Attanasio, D. J. Fritz, G. J. McBrien, and D. E. Bossi, “A review of lithium niobate modulators for fiber-optic communications systems,” *IEEE Journal of Selected Topics in Quantum Electronics*, vol. 6, no. 1, pp. 69–82, 2000.
- [7] A. Rao, and S. Fathpour, “Heterogeneous Thin-Film Lithium Niobate Integrated Photonics for Electrooptics and Nonlinear Optics,” *IEEE Journal of Selected Topics in Quantum Electronics*, vol. 24, no. 6, pp. 1–12, 2018.
- [8] [Online], Available: www.thorlabs.com/navigation.cfm?guide_id=2218.

- [9] [Online], Available: www.photonics.ixblue.com/store/lithium-niobate-electro-optic-modulator/intensity-modulators.
- [10] [Online], Available: <https://www.eospace.com/40-gb/s-modulators>.
- [11] [Online], Available: <https://www.hcphotonics.com/ppln-chips>.
- [12] [Online], Available: www.covesion.com/products/magnesium-doped-ppln-mgoppln-crystals/mgo-ppln-for-second-harmonic-generation/mshg1550-0.5.html.
- [13] [Online], Available: <http://www.psicorp.com/products/rf-and-optical-components/periodically-poled-lithium-niobate-ppln-frequency-converter>.
- [14] B. Jalali, and S. Fathpour, “Silicon Photonics,” *Journal of Lightwave Technology*, vol. 24, no. 12, pp. 4600–4615, 2006.
- [15] J. E. Bowers, T. Komljenovic, M. Davenport, J. Hulme, A. Y. Liu, C. T. Santis, A. Spott, S. Srinivasan, E. J. Stanton, and C. Zhang, “Recent advances in silicon photonic integrated circuits,” *Next-Generation Optical Communication: Components, Sub-Systems, and Systems V*, edited by G. Li and X. Zhou, SPIE, pp. 1–18, 2016.
- [16] A. H. Atabaki, S. Moazeni, F. Pavanello, H. Gevorgyan, J. Notaros, L. Alloatti, M. T. Wade, C. Sun, S. A. Kruger, H. Meng, K. Al Qubaisi, I. Wang, B. Zhang, A. Khilo, C. V. Baiocco, M. A. Popović, V. M. Stojanović, and R. J. Ram, “Integrating photonics with silicon nanoelectronics for the next generation of systems on a chip,” *Nature*, vol. 556, no. 7701, pp. 349–354, 2018.
- [17] M. Teng, A. Honardoost, Y. Alahmadi, S. Saghaye Polkoo, K. Kojima, H. Wen, C. K. Renshaw, P. LiKamWa, G. Li, S. Fathpour, R. Safian, and L. Zhuang, “Miniaturized Silicon Photonics Devices for Integrated Optical Signal Processors,” *Journal of Lightwave Technology*, vol. 38, no. 1, pp. 6–17, 2020.

- [18] K. Noguchi, O. Mitomi, and H. Miyazawa, "Millimeter-wave Ti:LiNbO₃ optical modulators," *Journal of Lightwave Technology*, vol. 16, no. 4, pp. 615–613, 1998.
- [19] P. G. Suchoski, T. K. Findakly, and F. J. Leonberger, "Stable low-loss proton-exchanged LiNbO₃ waveguide devices with no electro-optic degradation," *Optics Letters*, vol. 13, no. 11, pp. 1050–1052, 1988.
- [20] G. Poberaj, H. Hu, W. Sohler, and P. Günter, "Lithium niobate on insulator (LNOI) for micro-phonic devices," *Laser & Photonics Reviews*, vol. 6, no. 4, pp. 488–503, 2012.
- [21] A. Boes, B. Corcoran, L. Chang, J. Bowers, and A. Mitchell, "Status and Potential of Lithium Niobate on Insulator (LNOI) for Photonic Integrated Circuits," *Laser & Photonics Reviews*, vol. 12, no. 4, 2018.
- [22] M. Rusing, P. O. Weigel, J. Zhao, and S. Mookherjea, "Toward 3D Integrated Photonics Including Lithium Niobate Thin Films: A Bridge Between Electronics, Radio Frequency, and Optical Technology," *IEEE Nanotechnology Magazine*, vol. 13, no. 4, pp. 18–33, 2019.
- [23] W. Sohler, B. K. Das, D. Dey, S. Reza, H. Suche, and R. Ricken, "Erbium-doped lithium niobate waveguide lasers," *IEICE transactions on electronics*, vol. 88, no. 5, pp. 990–997, 2005.
- [24] D. Bruske, S. Suntsov, C. E. Ruter, and D. Kip, "Efficient Nd:Ti:LiNbO₃ ridge waveguide lasers emitting around 1085 nm," *Optics Express*, vol. 27, no. 6, pp. 8884–8889, 2019.
- [25] M. R. H. Sarker, H. Karim, R. Martinez, N. Love, and Y. Lin, "A Lithium Niobate High-Temperature Sensor for Energy System Applications," *IEEE Sensors Journal*, vol. 16, no. 15, pp. 5883–5888, 2016.
- [26] K. Buse, A. Adibi, and D. Psaltis, "Non-volatile holographic storage in doubly doped lithium niobate crystals," *Nature*, vol. 393, no. 6686, pp. 665–668, 1998.

- [27] V. Gopalan, V. Dierolf, and D. A. Scrymgeour, “Defect–domain wall interactions in trigonal ferroelectrics,” *Annu. Rev. Mater. Res.*, vol. 37, pp. 449–489, 2007.
- [28] P. Rabiei, J. Ma, S. Khan, J. Chiles, and S. Fathpour, “Heterogeneous lithium niobate photonics on silicon substrates,” *Opt. Express*, vol. 21, no. 21, pp. 25573–25581, 2013.
- [29] P. Rabiei, and P. Gunter, “Optical and electro-optical properties of submicrometer lithium niobate slab waveguides prepared by crystal ion slicing and wafer bonding,” *Applied Physics Letters*, vol. 85, no. 20, pp. 4603–4605, 2004.
- [30] M. Levy, R. M. Osgood, R. Liu, L. E. Cross, G. S. Cargill, A. Kumar, and H. Bakhru, “Fabrication of single-crystal lithium niobate films by crystal ion slicing,” *Applied Physics Letters*, vol. 73, no. 16, pp. 2293–2295, 1998.
- [31] H. Takagi, R. Maeda, N. Hosoda, and T. Suga, “Room-temperature bonding of lithium niobate and silicon wafers by argon-beam surface activation,” *Applied Physics Letters*, vol. 74, no. 16, pp. 2387–2389, 1999.
- [32] M. M. R. Howlader, T. Suga, and M. J. Kim, “Room temperature bonding of silicon and lithium niobate,” *Applied Physics Letters*, vol. 89, no. 3, 2006.
- [33] [Online], Available: <http://www.partow-tech.com/>.
- [34] [Online], Available: <https://www.nanoln.com/>.
- [35] [Online], Available: <https://www.ngk-insulators.com/en/index.html>.
- [36] Y. S. Lee, G. -D. Kim, W. -J. Kim, S. -S. Lee, W. -G. Lee, and W. H. Steier, “Hybrid Si-LiNbO₃ microring electro-optically tunable resonators for active photonic devices,” *Optics Letters*, vol. 36, no. 7, pp. 1119–1121, 2011.

- [37] P. O. Weigel, M. Savanier, C. T. DeRose, A. T. Pomerene, A. L. Starbuck, A. L. Lentine, V. Stenger, and S. Mookherjea, “Lightwave circuits in lithium niobate through hybrid waveguides with silicon photonics,” *Scientific Reports*, vol. 6, 2016.
- [38] A. J. Mercante, P. Yao, S. Shi, G. Schneider, J. Murakowski, and D. W. Prather, “110 GHz CMOS compatible thin film LiNbO₃ modulator on silicon,” *Optics Express*, vol. 24, no. 14, pp. 15590–15595, 2016.
- [39] S. Li, L. Cai, Y. Wang, Y. Jiang, and H. Hu, “Waveguides consisting of single-crystal lithium niobate thin film and oxidized titanium stripe,” *Optics Express*, vol. 23, no. 19, pp. 24212–24219, 2015.
- [40] L. Chang, M. H. P. Pfeiffer, N. Volet, M. Zervas, J. D. Peters, C. L. Manganelli, E. J. Stanton, Y. Li, T. J. Kippenberg, and J. E. Bowers, “Heterogeneous integration of lithium niobate and silicon nitride waveguides for wafer-scale photonic integrated circuits on silicon,” *Optics Letters*, vol. 42, no. 4, pp. 803–806, 2017.
- [41] Y. Wang, Z. Chen, H. Hu, “Analysis of waveguides on lithium niobate thin films,” *Crystals*, vol. 8, no. 5, 2018.
- [42] A. N. R. Ahmed, A. Mercante, S. Shi, P. Yao, and D. W. Prather, “Vertical mode transition in hybrid lithium niobate and silicon nitride-based photonic integrated circuit structures,” *Optics Letters*, vol. 43, no. 17, pp. 4140–4143, .
- [43] S. Liu, Y. Zheng, Z. Fang, X. Ye, Y. Cheng, and X. Chen, “Effective four-wave mixing in the lithium niobate on insulator microdisk by cascading quadratic processes,” *Optics Letters*, vol. 44, no. 6, pp. 1456–1459, 2019.
- [44] M. Zhang, C. Wang, R. Cheng, A. Shams-Ansari, and M. Loncar, “Monolithic ultra-high-Q lithium niobate microring resonator,” *Optica*, vol. 4, no. 12, pp. 1536–1537, 2017.

- [45] I. Krasnokutskaya, J. -L. J. Tambasco, X. Li, and A. Peruzzo, “Ultra-low loss photonic circuits in lithium niobate on insulator,” *Optics Express*, vol. 26, no. 2, pp. 897–904, 2018.
- [46] X. P. Li, K. X. Chen, and Z. F. Hu, “Low-loss bent channel waveguides in lithium niobate thin film by proton exchange and dry etching,” *Optical Materials Express*, vol. 8, no. 5, pp. 1322–1327, 2018.
- [47] L. Cai, A. Mahmoud, and G. Piazza, “Low-loss waveguides on Y-cut thin film lithium niobate: towards acousto-optic applications,” *Optics Express*, vol. 27, no. 7, pp. 9794–9802, 2019.
- [48] Q. Xu, Y. -X. Shao, R. -Q. Piao, F. Chen, X. Wang, X. -F. Yang, W. -H. Wong, E. Y. -B. Pun, and D. -L. Zhang, “A Theoretical Study on Rib-Type Photonic Wires Based on LiNbO₃ Thin Film on Insulator,” *Advanced Theory and Simulations*, vol. 2, no. 10, 2019.
- [49] L. Cai, S. L. H. Han, and H. Hu, “Waveguides in single-crystal lithium niobate thin film by proton exchange,” *Optics Express*, vol. 23, no. 2, pp. 1240–1248, 2015.
- [50] L. Cai, R. Kong, Y. Wang, and H. Hu, “Channel waveguides and y-junctions in x-cut single-crystal lithium niobate thin film,” *Optics Express*, vol. 23, no. 22, pp. 29211–29221, 2015.
- [51] Y. Yamaguchi, A. Kanno, N. Yamamoto, and T. Kawanishi, “Experimental Evaluation of Wavelength-Dependence of Thin-Film LiNbO₃ Modulator with an Extinction-Ratio-Tunable Structure,” in *2019 24th OptoElectronics and Communications Conference (OECC) and 2019 International Conference on Photonics in Switching and Computing (PSC)*, pp. 1–3, 2019.
- [52] L. Chen, J. Nagy, and R. M. Reano, “Patterned ion-sliced lithium niobate for hybrid photonic integration on silicon,” *Optical Materials Express*, vol. 6, no. 7, pp. 2460–2467, 2016.
- [53] R. Takigawa, and T. Asano, “Thin-film lithium niobate-on-insulator waveguides fabricated on silicon wafer by room-temperature bonding method with silicon nanoadhesive layer,” *Optics Express*, vol. 26, no. 19, pp. 24413–24421, 2018.

- [54] L. Cao, A. Aboketaf, Z. Wang, and S. Preble, “Hybrid amorphous silicon (a-Si:H)–LiNbO₃ electro-optic modulator,” *Optics Communications*, vol. 330, pp. 40–44, 2014.
- [55] J. Wang, F. Bo, S. Wan, W. Li, F. Gao, J. Li, G. Zhang, and J. Xu, “High-Q lithium niobate microdisk resonators on a chip for efficient electro-optic modulation,” *Optics Express*, vol. 23, no. 18, pp. 23072–23078, 2015.
- [56] Z. Hao, J. Wang, S. Ma, W. Mao, F. Bo, F. Gao, G. Zhang, and J. Xu, “Sum-frequency generation in on-chip lithium niobate microdisk resonators,” *Photon. Res.*, vol. 5, no. 6, pp. 623–628, 2017.
- [57] L. Zhang, D. Zheng, W. Li, F. Bo, F. Gao, Y. Kong, G. Zhang, and J. Xu, “Microdisk resonators with lithium-niobate film on silicon substrate,” *Optics Express*, vol. 27, no. 23, pp. 33662–33669, 2019.
- [58] A. Guarino, G. Poberaj, D. Rezzonico, R. Degl’Innocenti, and P. Gunter, “Electro–optically tunable microring resonators in lithium niobate,” *Nature Photonics*, vol. 1, no. 7, pp. 407–410, 2007.
- [59] Y. He, H. Liang, R. Luo, M. Li, and Q. Lin, “Dispersion engineered high quality lithium niobate microring resonators,” *Optics Express*, vol. 26, no. 13, pp. 16315–16322, 2018.
- [60] R. Wolf, I. Breunig, H. Zappe, and K. Buse, “Scattering-loss reduction of ridge waveguides by sidewall polishing,” *Optics Express*, vol. 26, no. 16, pp. 19815–19820, 2018.
- [61] M. Bahadori, Y. Yang, L. L. Goddard, and S. Gong, “High performance fully etched isotropic microring resonators in thin-film lithium niobate on insulator platform,” *Optics Express*, vol. 27, no. 15, pp. 22025–22039, 2019.

- [62] L. Chen, M. G. Wood, and R. M. Reano, “12.5 pm/V hybrid silicon and lithium niobate optical microring resonator with integrated electrodes,” *Optics Express*, vol. 21, no. 22, pp. 27003–27010, 2013.
- [63] L. Chen, Q. Xu, M. G. Wood, and R. M. Reano, “Hybrid silicon and lithium niobate electro-optical ring modulator,” *Optica*, vol. 1, no. 2, pp. 112–118, 2014.
- [64] L. Chen, J. Chen, J. Nagy, and R. M. Reano, “Highly linear ring modulator from hybrid silicon and lithium niobate,” *Optics Express*, vol. 23, no. 10, pp. 13255–13264, 2015.
- [65] A. Rao, A. Patil, J. Chiles, M. Malinowski, S. Novak, K. Richardson, P. Rabiei, and S. Fathpour, “Heterogeneous microring and Mach-Zehnder modulators based on lithium niobate and chalcogenide glasses on silicon,” *Optics Express*, vol. 23, no. 17, pp. 22746–22752, 2015.
- [66] A. Rao, A. Patil, P. Rabiei, A. Honardoost, R. DeSalvo, A. Paoletta, and S. Fathpour, “High-performance and linear thin-film lithium niobate Mach-Zehnder modulators on silicon up to 50 GHz,” *Optics Letters*, vol. 41, no. 24, pp. 5700–5703, 2016.
- [67] S. Jin, L. Xu, H. Zhang, and Y. Li, “LiNbO₃ Thin-Film Modulators Using Silicon Nitride Surface Ridge Waveguides,” *IEEE Photonics Technology Letters*, vol. 28, no. 7, pp. 736–739, 2016.
- [68] M. Mahmoud, C. Bottenfield, L. Cai, and G. Piazza, “Fully integrated lithium niobate electro-optic modulator based on asymmetric Mach-Zehnder interferometer etched in LNOI platform,” in *2017 IEEE Photonics Conference (IPC)*, pp. 223–224, 2017.
- [69] C. Wang, M. Zhang, B. Stern, M. Lipson, and M. Loncar, “Nanophotonic lithium niobate electro-optic modulators,” *Optics Express*, vol. 26, no. 2, pp. 1547–1555, 2018.

- [70] C. Wang, M. Zhang, X. Chen, M. Bertrand, A. Shams-Ansari, S. Chandrasekhar, P. Winzer, and M. Loncar, “Integrated lithium niobate electro-optic modulators operating at CMOS-compatible voltages,” *Nature*, vol. 562, no. 7725, pp. 101–104, 2018.
- [71] P. O. Weigel, J. Zhao, K. Fang, H. Al-Rubaye, D. Trotter, D. Hood, J. Mudrick, C. Dallo, A. T. Pomerene, A. L. Starbuck, C. T. DeRose, A. L. Lentine, G. Rebeiz, and S. Mookherjea, “Bonded thin film lithium niobate modulator on a silicon photonics platform exceeding 100 GHz 3-dB electrical modulation bandwidth,” *Optics Express*, vol. 26, no. 18, pp. 23728–23739, 2018.
- [72] X. Wang, P. O. Weigel, J. Zhao, M. Ruesing, and S. Mookherjea, “Achieving beyond-100-GHz large-signal modulation bandwidth in hybrid silicon photonics Mach Zehnder modulators using thin film lithium niobate,” *APL Photonics*, vol. 4, no. 9, 2019.
- [73] A. J. Mercante, S. Shi, P. Yao, L. Xie, R. M. Weikle, and D. W. Prather, “Thin film lithium niobate electro-optic modulator with terahertz operating bandwidth,” *Optics Express*, vol. 26, no. 11, pp. 14810–14816, 2018.
- [74] M. He, M. Xu, Y. Ren, J. Jian, Z. Ruan, Y. Xu, S. Gao, S. Sun, X. Wen, L. Zhou, L. Liu, C. Guo, H. Chen, S. Yu, L. Liu, and X. Cai, “High-performance hybrid silicon and lithium niobate Mach–Zehnder modulators for 100 Gbit s⁻¹ and beyond,” *Nature Photonics*, vol. 13, no. 5, pp. 359–364, 2019.
- [75] A. N. R. Ahmed, S. Shi, M. Zablocki, P. Yao, and D. W. Prather, “Tunable hybrid silicon nitride and thin-film lithium niobate electro-optic microresonator,” *Optics Letters*, vol. 44, no. 3, pp. 618–621, 2019.
- [76] A. N. R. Ahmed, S. Shi, A. J. Mercante, and D. W. Prather, “High-performance racetrack resonator in silicon nitride - thin film lithium niobate hybrid platform,” *Optics Express*, vol. 27, no. 21, pp. 30741–30751, 2019.

- [77] V. Stenger, A. Pollick, and C. Acampado, “Integrable Thin Film Lithium Niobate (TFLNTM) on Silicon Electro-optic Modulators,” in *Optical Fiber Communication Conference (OFC) 2019*, pp. Tu2H.6, 2019.
- [78] M. Xu, W. Chen, M. He, X. Wen, Z. Ruan, J. Xu, L. Chen, L. Liu, S. Yu, and X. Cai, “Michelson interferometer modulator based on hybrid silicon and lithium niobate platform,” *APL Photonics*, vol. 4, no. 10, 2019.
- [79] N. Boynton, H. Cai, M. Gehl, S. Arterburn, C. Dallo, A. Pomerene, A. Starbuck, D. Hood, D. C. Trotter, T. Friedmann, C. T. DeRose, and A. Lentine, “A heterogeneously integrated silicon photonic/lithium niobate travelling wave electro-optic modulator,” *Optics Express*, vol. 28, no. 2, pp. 1868–1884, 2020.
- [80] L. Shao, M. Yu, S. Maity, N. Sinclair, L. Zheng, C. Chia, A. Shams-Ansari, C. Wang, M. Zhang, K. Lai, and M. Loncar, “Microwave-to-optical conversion using lithium niobate thin-film acoustic resonators,” *Optica*, vol. 6, no. 12, pp. 1498–1505, 2019.
- [81] L. Cai, A. Mahmoud, M. Khan, M. Mahmoud, T. Mukherjee, J. Bain, and G. Piazza, “Acousto-optical modulation of thin film lithium niobate waveguide devices,” *Photonics Research*, vol. 7, no. 9, pp. 1003–1013, 2019.
- [82] M. Khan, A. Mahmoud, L. Cai, M. Mahmoud, T. Mukherjee, J. A. Bain, and G. Piazza, “Extraction of Elasto-Optic Coefficient of Thin Film Arsenic Trisulfide Using a Mach-Zehnder Acousto-Optic Modulator on Lithium Niobate,” *Journal of Lightwave Technology*, 2019.
- [83] Z. Chen, R. Peng, Y. Wang, H. Zhu, H. Hu, “Grating coupler on lithium niobate thin film waveguide with a metal bottom reflector,” *Optical Materials Express*, vol. 7, no. 11, pp. 4010–4017, 2017.

- [84] Z. Chen, Y. Wang, H. Zhang, and H. Hu, "Silicon grating coupler on a lithium niobate thin film waveguide," *Optical Materials Express*, vol. 8, no. 5, pp. 1253–1258, 2018.
- [85] L. Cai, and G. Piazza, "Low-loss chirped grating for vertical light coupling in lithium niobate on insulator," *Journal of Optics*, vol. 21, no. 6, 2019.
- [86] A. Kar, M. Bahadori, S. Gong, and L. L. Goddard, "Realization of alignment-tolerant grating couplers for z-cut thin-film lithium niobate," *Optics Express*, vol. 27, no. 11, pp. 15856–15867, 2019.
- [87] I. Krasnokutska, R. J. Chapman, J. -L. J. Tambasco, and A. Peruzzo, "High coupling efficiency grating couplers on lithium niobate on insulator," *Optics Express*, vol. 27, no. 13, pp. 17681–17685, 2019.
- [88] L. He, M. Zhang, A. Shams-Ansari, R. Zhu, C. Wang, and M. Loncar, "Low-loss fiber-to-chip interface for lithium niobate photonic integrated circuits," *Optics Letters*, vol. 44, no. 9, pp. 2314–2317, 2019.
- [89] I. Krasnokutska, J. -L. J. Tambasco, and A. Peruzzo, "Nanostructuring of LNOI for efficient edge coupling," *Optics Express*, vol. 27, no. 12, pp. 16578–16585, 2019.
- [90] A. Rao, M. Malinowski, A. Honardoost, J. R. Talukder, P. Rabiei, P. Delfyett, and S. Fathpour, "Second-harmonic generation in periodically-poled thin film lithium niobate wafer-bonded on silicon," *Optics Express*, vol. 24, no. 26, pp. 29941–29947, 2016.
- [91] L. Chang, Y. Li, N. Volet, L. Wang, J. Peters, and J. E. Bowers, "Thin film wavelength converters for photonic integrated circuits," *Optica*, vol. 3, no. 5, pp. 531–535, 2016.
- [92] C. Wang, C. Langrock, A. Marandi, M. Jankowski, M. Zhang, B. Desiatov, M. M. Fejer, and M. Loncar, "Ultrahigh-efficiency wavelength conversion in nanophotonic periodically poled lithium niobate waveguides," *Optica*, vol. 5, no. 11, pp. 1438–1441, 2018.

- [93] M. Yu, B. Desiatov, Y. Okawachi, A. L. Gaeta, and M. Loncar, “Coherent two-octave-spanning supercontinuum generation in lithium-niobate waveguides,” *Optics Letters*, vol. 44, no. 5, pp. 1222–1225, 2019.
- [94] T. Ding, Y. Zheng, and X. Chen, “Integration of cascaded electro-optic and nonlinear processes on a lithium niobate on insulator chip,” *Optics Letters*, vol. 44, no. 6, pp. 1524–1527, 2019.
- [95] A. Rao, K. Abdelsalam, T. Sjaardema, A. Honardoost, G. F. Camacho-Gonzalez, and S. Fathpour, “Actively-monitored periodic-poling in thin-film lithium niobate photonic waveguides with ultrahigh nonlinear conversion efficiency of $4600\%W^{-1}cm^{-2}$,” *Optics Express*, vol. 27, no. 18, pp. 25920–25930, 2019.
- [96] J. -Y. Chen, Z. -H. Ma, Y. M. Sua, Z. Li, C. Tang, and Y. -P. Huang, “Ultra-efficient frequency conversion in quasi-phase-matched lithium niobate microrings,” *Optica*, vol. 6, no. 9, pp. 1244–1245, 2019.
- [97] J. Lu, J. B. Surya, X. Liu, A. W. Bruch, Z. Gong, Y. Xu, H. X. Tang, “Periodically poled thin-film lithium niobate microring resonators with a second-harmonic generation efficiency of $250,000\%/W$,” *Optica*, vol. 6, no. 12, pp. 1455–1460, 2019.
- [98] R. Luo, Y. He, H. Liang, M. Li, and Q. Lin, “Semi-Nonlinear Nanophotonic Waveguides for Highly Efficient Second-Harmonic Generation,” *Laser & Photonics Reviews*, vol. 13, no. 3, 2019.
- [99] M. Zhang, B. Buscaino, C. Wang, A. Shams-Ansari, C. Reimer, R. Zhu, J. M. Kahn, and M. Loncar, “Broadband electro-optic frequency comb generation in a lithium niobate microring resonator,” *Nature*, vol. 568, no. 7752, pp. 373–377, 2019.

- [100] C. Wang, M. Zhang, M. Yu, R. Zhu, H. Hu, and M. Loncar, “Monolithic lithium niobate photonic circuits for Kerr frequency comb generation and modulation,” *Nature Communications*, vol. 10, no. 1, pp. 1–6, 2019.
- [101] M. Jankowski, C. Langrock, B. Desiatov, A. Marandi, C. Wang, M. Zhang, C. R. Phillips, M. Loncar, and M. M. Fejer, “Ultrabroadband nonlinear optics in nanophotonic periodically poled lithium niobate waveguides,” *Optica*, vol. 7, no. 1, pp. 40–46, 2020.
- [102] A. Rao, N. Nader, M. J. Stevens, T. Gerrits, O. S. Magana-Loaiza, G. F. Camacho-Gonzalez, J. Chiles, A. Honardoost, M. Malinowski, R. Mirin, and S. Fathpour, “Photon Pair Generation on a Silicon Chip Using Nanophotonic Periodically-Poled Lithium Niobate Waveguides,” in *2018 Conference on Lasers and Electro-Optics (CLEO)*, pp. 1–2, 2018.
- [103] B. S. Elkus, K. Abdelsalam, A. Rao, V. Velez, S. Fathpour, P. Kumar, and G. S. Kanter, “Generation of broadband correlated photon-pairs in short thin-film lithium-niobate waveguides,” *Optics Express*, vol. 27, no. 26, pp. 38521–38531, 2019.
- [104] J. -Y. Chen, Y. M. Sua, Z. -H. Ma, C. Tang, Z. Li, and Y. -P. Huang, “Efficient parametric frequency conversion in lithium niobate nanophotonic chips,” *OSA Continuum*, vol. 2, no. 10, pp. 2914–2924, 2019.
- [105] J. Zhao, C. Ma, M. Rusing, and S. Mookherjea, “Entangled photon-pair generation in periodically-poled thin-film lithium niobate waveguides,” *arXiv*, 2019.
- [106] A. Rao, N. Nader, T. Gerrits, M. J. Stevens, O. S. Magana-Loaiza, G. F. Camacho-Gonzalez, J. Chiles, A. Honardoost, M. Malinowski, R. Mirin, and S. Fathpour, “Spectral resolution of second-order coherence of broadband biphotons,” in *2018 Conference on Lasers and Electro-Optics (CLEO)*, pp. 1–2, 2018.

- [107] J. Leuthold, C. Koos, and W. Freude, “Nonlinear silicon photonics,” *Nature Photonics*, vol. 4, no. 8, 2010.
- [108] K. Liu, C. R. Ye, S. Khan, and V. J. Sorger, “Review and perspective on ultrafast wavelength-size electro-optic modulators,” *Laser & Photonics Reviews*, vol. 9, no. 10, pp. 172–194, 2015.
- [109] W. Heni, Y. Kutuvantavida, C. Haffner, H. Zwickel, C. Kieninger, S. Wolf, M. Lauermann, Y. Fedoryshyn, A. F. Tillack, L. E. Johnson, D. L. Elder, B. H. Robinson, W. Freude, C. Koos, J. Leuthold, and L. R. Dalton, “Silicon–organic and plasmonic–organic hybrid photonics,” *ACS Photonics*, vol. 4, no. 7, pp. 1576–1590, 2017.
- [110] A. Rao, and S. Fathpour, “Compact Lithium Niobate Electrooptic Modulators,” *IEEE Journal of Selected Topics in Quantum Electronics*, vol. 24, no. 4, pp. 1–14, 2018.
- [111] S. Fathpour, “Heterogeneous Nonlinear Integrated Photonics,” *IEEE Journal of Quantum Electronics*, vol. 54, no. 6, pp. 1–16, 2018.
- [112] P. Rabiei, W. H. Steier, “Lithium niobate ridge waveguides and modulators fabricated using smart guide,” *Applied Physics Letters*, vol. 86, no. 16, 2005.
- [113] A. Honardoost, G. F. Camacho-Gonzalez, S. Khan, M. Malinowski, A. Rao, J. Tremblay, A. Yadav, K. Richardson, M. C. Wu, and S. Fathpour, “Cascaded Integration of Optical Waveguides With Third-Order Nonlinearity With Lithium Niobate Waveguides on Silicon Substrates,” *IEEE Photonics Journal*, vol. 10, no. 3, pp. 1–9, 2018.
- [114] I. Bakish, R. Califa, T. Ilovitsh, V. Artel, G. Winzer, K. Voigt, L. Zimmermann, E. Shekel, C. N. Sukenik, and A. Zadok, “Voltage-Induced Phase Shift in a Hybrid LiNbO₃-on-Silicon Mach-Zehnder Interferometer,” in *Advanced Photonics 2013*, pp. IW4A.2, 2013.
- [115] J. Chiles, and S. Fathpour, “Mid-infrared integrated waveguide modulators based on silicon-on-lithium-niobate photonics,” *Optica*, vol. 1, no. 5, pp. 350–355, 2014.

- [116] A. Honardoost, F. Arab Juneghani, R. Safian, and S. Fathpour, “Towards subterahertz bandwidth ultracompact lithium niobate electrooptic modulators,” *Optics Express*, vol. 27, no. 5, pp. 6495–6501, 2019.
- [117] S. Fathpour, A. Honardoost, and S. Khan, “Thin-film integration compatible with silicon photonics foundry production,” *US Patent App. 15/932,800*, 2018.
- [118] M. L. Bortz, and M. M. Fejer, “Annealed proton-exchanged LiNbO₃ waveguides,” *Optics Letters*, vol. 16, no. 23, pp. 1844–1846, 1991.
- [119] L. Chen, and R. M. Reano, “Compact electric field sensors based on indirect bonding of lithium niobate to silicon microrings,” *Optics Express*, vol. 20, no. 4, pp. 4032–4038, 2012.
- [120] T. Nagatsuma, G. Ducournau, C. C. Renaud, “Advances in terahertz communications accelerated by photonics,” *Nature Photonics*, vol. 10, no. 6, 2016.
- [121] D. A. B. Miller, “Optical interconnects to electronic chips,” *Applied Optics*, vol. 49, no. 25, pp. F59–F70, 2010.
- [122] M. Yu, C. Wang, M. Zhang, and M. Loncar, “Chip-Based Lithium-Niobate Frequency Combs,” *IEEE Photonics Technology Letters*, vol. 31, no. 23, pp. 1894–1897, 2019.
- [123] M. R. Escalé, D. Pohl, M. Madi, P. Brotzer, F. Kaufmann, A. Sergeev, U. Meier, E. Alberti, and R. Grange, “Integrated Electro-Optic Spectrometers on Thin-Film Lithium Niobate,” in *Conference on Lasers and Electro-Optics*, pp. SF2J.4, 2019.
- [124] D. Shrekenhamer, C. M. Watts, and W. J. Padilla, “Terahertz single pixel imaging with an optically controlled dynamic spatial light modulator,” *Optics Express*, vol. 21, no. 10, pp. 12507–12518, 2013.

- [125] Y. Shen, N. C. Harris, S. Skirlo, M. Prabhu, T. Baehr-Jones, M. Hochberg, X. Sun, S. Zhao, H. Larochelle, D. Englund, and M. Soljacic, “Deep learning with coherent nanophotonic circuits,” *Nature Photonics*, vol. 11, no. 7, 2017.
- [126] J. L. O’Brien, “Optical Quantum Computing,” *Science*, vol. 318, no. 5856, pp. 1567–1570, 2007.
- [127] K. K. Mehta, G. N. West, and R. J. Ram, “SiN-on-LiNbO₃ integrated optical modulation at visible wavelengths,” in *2017 Conference on Lasers and Electro-Optics (CLEO)*, pp. 1–2, 2017.
- [128] B. Desiatov, A. Shams-Ansari, M. Zhang, C. Wang, and Marko Loncar, “Ultra-low-loss integrated visible photonics using thin-film lithium niobate,” *Optica*, vol. 6, no. 3, pp. 380–384, 2019.
- [129] A. Honardoost, R. Safian, A. Rao, and S. Fathpour, “High-Speed Modeling of Ultracompact Electrooptic Modulators,” *Journal of Lightwave Technology*, vol. 36, no. 24, pp. 5893–5902, 2018.
- [130] M. Jin, J. -Y. Chen, Y. M. Sua, and Y. -P. Huang, “High-extinction electro-optic modulation on lithium niobate thin film,” *Optics Letters*, vol. 44, no. 5, pp. 1265–1268, 2019.
- [131] A. Karim, and J. Devenport, “Noise Figure Reduction in Externally Modulated Analog Fiber-Optic Links,” *IEEE Photonics Technology Letters*, vol. 19, no. 5, pp. 312–314, 2007.
- [132] L. E. Myers, R. C. Eckardt, M. M. Fejer, R. L. Byer, W. R. Bosenberg, J. W. Pierce, “Quasi-phase-matched optical parametric oscillators in bulk periodically poled LiNbO₃,” , vol. 12, no. 11, pp. 2102–2116, 1995.

- [133] J. T. Nagy, and R. M. Reano, “Reducing leakage current during periodic poling of ion-sliced x-cut MgO doped lithium niobate thin films,” *Optical Materials Express*, vol. 9, no. 7, pp. 3146–3155, 2019.
- [134] J. Zhao, M. Rusing, and S. Mookherjea, “Optical diagnostic methods for monitoring the poling of thin-film lithium niobate waveguides,” *Optics Express*, vol. 27, no. 9, pp. 12025–12038, 2019.
- [135] M. Rusing, J. Zhao, and S. Mookherjea, “Second harmonic microscopy of poled x-cut thin film lithium niobate: Understanding the contrast mechanism,” *Journal of Applied Physics*, vol. 126, no. 11, 2019.
- [136] A. Boes, L. Chang, M. Knoerzer, T. G. Nguyen, J. D. Peters, J. E. Bowers, and A. Mitchell, “Improved second harmonic performance in periodically poled LNOI waveguides through engineering of lateral leakage,” *Optics Express*, vol. 27, no. 17, pp. 23919–23928, 2019.
- [137] A. Rao, and S. Fathpour, “Second-Harmonic Generation in Integrated Photonics on Silicon,” *Physica Status Solidi (a)*, vol. 215, no. 4, 2018.
- [138] A. Rao, J. Chiles, S. Khan, S. Toroghi, M. Malinowski, G. F. Camacho-Gonzalez, and S. Fathpour, “Second-harmonic generation in single-mode integrated waveguides based on mode-shape modulation,” *Applied Physics Letters*, vol. 110, no. 11, 2017.
- [139] C. Wang, X. Xiong, N. Andrade, V. Venkataraman, X. -F. Ren, G. -C. Guo, and M. Loncar, “Second harmonic generation in nano-structured thin-film lithium niobate waveguides,” *Optics Express*, vol. 25, no. 6, pp. 6963–6973, 2017.
- [140] A. Rao, T. Sjaardema, G. F. Camacho-Gonzalez, A. Honardoost, M. Malinowski, K. Schep-ler, and S. Fathpour, “Random Quasi-Phase-Matching on a Nanophotonic Heterogeneous Silicon Chip,” in *Conference on Lasers and Electro-Optics*, pp. SM1B.2, 2018.

- [141] L. Cai, Y. Wang, and H. Hu, “Efficient second harmonic generation in $\chi(2)$ profile reconfigured lithium niobate thin film,” *Optics Communication*, vol. 387, pp. 405–408, 2017.
- [142] R. Wolf, I. Breunig, H. Zappe, and K. Buse, “Cascaded second-order optical nonlinearities in on-chip micro rings,” *Optics Express*, vol. 25, no. 24, pp. 29927–29933, 2017.
- [143] R. Luo, H. Jiang, S. Rogers, H. Liang, Y. He, and Q. Lin, “On-chip second-harmonic generation and broadband parametric down-conversion in a lithium niobate microresonator,” *Optics Express*, vol. 25, no. 20, pp. 24531–24539, 2017.
- [144] R. Luo, Y. He, H. Liang, M. Li, and Q. Lin, “Semi-Nonlinear Nanophotonic Waveguides for Highly Efficient Second-Harmonic Generation,” *Laser & Photonics Reviews*, vol. 13, no. 3, 2019.
- [145] R. Luo, Y. He, H. Liang, M. Li, and Q. Lin, “Highly tunable efficient second-harmonic generation in a lithium niobate nanophotonic waveguide,” *Optical*, vol. 5, no. 8, pp. 1006–1011, 2018.
- [146] D. D. Hickstein, D. R. Carlson, A. Kowligy, M. Kirchner, S. R. Domingue, N. Nader, H. Timmers, A. Lind, G. G. Ycas, M. M. Murnane, H. C. Kapteyn, S. B. Papp, and S. A. Diddams, “High-harmonic generation in periodically poled waveguides,” *Optica*, vol. 4, no. 12, pp. 1538–1544, 2017.
- [147] D. A. Bryan, R. Gerson, and H. E. Tomaschke, “Increased optical damage resistance in lithium niobate,” *Applied Physics Letters*, vol. 44, no. 9, pp. 847–849, 1984.
- [148] R. Luo, Y. He, H. Liang, M. Li, J. Ling, and Q. Lin, “Optical parametric generation in a lithium niobate microring with modal phase matching,” *Physical Review Applied*, vol. 11, no. 3, 2019.

- [149] G. Li, Y. Chen, H. Jiang, and X. Chen, “Broadband sum-frequency generation using d33 in periodically poled LiNbO₃ thin film in the telecommunications band,” *Optics Letters*, vol. 42, no. 5, pp. 939–942, 2017.
- [150] X. Ye, S. Liu, Y. Chen, Y. Zheng, and X. Chen, “Sum-frequency generation in lithium-niobate-on-insulator microdisk via modal phase matching,” *Optics Letters*, vol. 45, no. 2, pp. 523–526, 2020.
- [151] S. Liu, Y. Zheng, Z. Fang, X. Ye, Y. Cheng, and X. Chen, “Effective four-wave mixing in the lithium niobate on insulator microdisk by cascading quadratic processes,” *Optics Letters*, vol. 44, no. 6, pp. 1456–1459, 2019.
- [152] T. Sjaardema, M. Malinowski, A. Rao, and S. Fathpour, “,” *under preparation for Optica*, 2020.
- [153] T. Sjaardema, A. Rao, and S. Fathpour, “Third- and Fourth-Harmonic Generation in Cascaded Periodically-Poled Lithium Niobate Ultracompact Waveguides on Silicon,” in *Conference on Lasers and Electro-Optics*, pp. STh1J.1, 2019.
- [154] J. Lin, N. Yao, Z. Hao, J. Zhang, W. Mao, M. Wang, W. Chu, R. Wu, Z. Fang, L. Qiao, W. Fang, F. Bo, and Y. Cheng, “Broadband quasi-phase-matched harmonic generation in an on-chip monocrystalline lithium niobate microdisk resonator,” *Physical Review Letters*, vol. 122, no. 17, 2019.
- [155] S. Liu, Y. Zheng, and X. Chen, “Cascading second-order nonlinear processes in a lithium niobate-on-insulator microdisk,” *Optics Letters*, vol. 42, no. 18, pp. 3626–3629, 2017.
- [156] Y. He, Q. -F. Yang, J. Ling, R. Luo, H. Liang, M. Li, B. Shen, H. Wang, K. Vahala, and Q. Lin, “Self-starting bi-chromatic LiNbO₃ soliton microcomb,” *Optica*, vol. 6, no. 9, pp. 1138–1144, 2019.

- [157] Z. Gong, X. Liu, Y. Xu, M. Xu, J. B. Surya, J. Lu, A. Bruch, C. Zou, H. X. Tang, “Soliton microcomb generation at $2\ \mu\text{m}$ in z -cut lithium niobate microring resonators,” *Optics Letters*, vol. 44, no. 12, pp. 3182–3185, 2019.
- [158] M. Li, H. Liang, R. Luo, Y. He, and Q. Lin, “High-Q 2D Lithium Niobate Photonic Crystal Slab Nanoresonators,” *Laser & Photonics Reviews*, vol. 13, no. 5, 2019.
- [159] G. F. Camacho Gonzalez, M. Malinowski, A. Honardoost, and S. Fathpour, “Design of a hybrid chalcogenide-glass on lithium-niobate waveguide structure for high-performance cascaded third- and second-order optical nonlinearities,” *Applied Optics*, vol. 58, no. 13, pp. D1–D6, 2019.
- [160] K. Abdelsalam, T. Li, J. B. Khurgin, and S. Fathpour, “Linear isolators using wavelength conversion,” *Optica*, vol. 7, no. 3, pp. 209–213, 2020.
- [161] N. Gisin, G. Ribordy, W. Tittel, and H. Zbinden, “Quantum cryptography,” *Reviews of Modern Physics*, vol. 74, no. 1, pp. 145–195, 2002.
- [162] F. Lenzini, J. Janousek, O. Thearle, M. Villa, B. Haylock, S. Kasture, L. Cui, H. -P. Phan, D. V. Dao, H. Yonezawa, P. K. Lam, E. H. Huntington, and M. Lobino, “Integrated photonic platform for quantum information with continuous variables,” *Science Advances*, vol. 4, no. 12, 2018.
- [163] H. Jin, F. M. Liu, P. Xu, J. L. Xia, M. L. Zhong, Y. Yuan, J. W. Zhou, Y. X. Gong, W. Wang, and S. N. Zhu, “On-Chip Generation and Manipulation of Entangled Photons Based on Reconfigurable Lithium-Niobate Waveguide Circuits,” *Physical Review Letters*, vol. 113, no. 10, 2014.

- [164] O. Alibart, V. D’Auria, M. De Micheli, F. Doutre, F. Kaiser, L. Labonté, T. Lunghi, É. Picholle, and S. Tanzilli, “Quantum photonics at telecom wavelengths based on lithium niobate waveguides,” *Journal of Optics*, vol. 18, no. 10, 2016.
- [165] K. -H. Luo, S. Brauner, C. Eigner, P. R. Sharapova, R. Ricken, T. Meier, H. Herrmann, and C. Silberhorn, “Nonlinear integrated quantum electro-optic circuits,” *Science advances*, vol. 5, no. 1, 2019.

CHAPTER 3: HIGH-SPEED MODELING OF ULTRACOMPACT ELECTROOPTIC MODULATORS

The contents of this chapter have been published in: A. Honardoost, R. Safian, A. Rao, and S. Fathpour, "High-speed modeling of ultracompact electrooptic modulators," IEEE J. Light. Technol. 36(24), 5893–5902 (2018).

Abstract– The technology for compact thin-film lithium niobate electrooptic modulators has made significant advances recently. With achieving high levels of maturity for such platforms, a model is now required in order to accurately design the devices and reliably predict their performance limits. In this paper, a general transmission-line model is developed for predicting the frequency-dependent response of the compact modulators. The main radio frequency (RF) parameters of the modulators, such as characteristic impedance, effective index, and attenuation constant are calculated as a function of the coplanar waveguide dimensions, and validated by using numerical simulations. The accuracy of the model in predicting the 3-dB modulation bandwidth of the devices is verified by comparison with experimental results. Finally, guidelines for device design with significant improvement in the attainable modulation bandwidth are also presented by optimization of RF and optical parameters, predicting > 100 GHz modulation bandwidth. The presented model is not limited to emerging thin-film lithium niobate devices, and is applicable to any type of ultracompact electrooptic modulator.

3.1 Introduction

Optical communication systems have been the focus of substantial amount of research over the past few decades [1], [2]. Optical modulators are among the key components of these systems for both digital and analog applications, such as optical interconnects, datacom and telecom, and integrated RF photonics [3]–[6]. Several platforms have been developed in order to pursue high-performance

optical modulators.

Historically, commercial optical modulators have been made on materials with strong electrooptic (EO) effect (e.g., lithium niobate, LN or LiNbO_3) or electroabsorption (EA) effect (particularly, III-V compound semiconductors). More recently, silicon (Si) optical modulators based on free-carrier plasma dispersion effect (FCA) are being widely pursued, as they benefit from compatibility with standard Si foundry processing [6]–[8]. Another recent trend is heterogeneous integration of compound semiconductors as well as silicon germanium (SiGe), on silicon substrates that utilize EA effects such as Franz-Keldysh in bulk semiconductors or quantum-confined Stark effect in quantum-well structures [9]–[12]. Several modulators operating based on FCA or EA have been demonstrated with high data transmission rates up to 50 Gb/s. However, they typically suffer from low extinction ratios [9], [11]–[14].

On the contrary, modulators relying on linear EO or Pockel's effect have demonstrated modulation depth of 20 dB or more [21] as well as up to 100 GHz modulation bandwidth (BW) [16]. With such performance, LN has been well established as the standard material of choice for EO modulators in applications where high BW and extinction ratio are required, e.g., in long-haul communications [17]. Transparency in a broad range of the electromagnetic spectrum (0.4-5 μm), and a large EO coefficient (31 pm/V) are among other reasons which make LN a suitable option for EO modulators [21].

However, the conventional LN EO modulators suffer from a number of drawbacks, as proceeding to high integration levels is demanded. Two methods are traditionally used in order to form optical waveguides in conventional LN modulators, i.e., diffusion of dopants, such as titanium (Ti) [21], or the proton exchange process [18]. The resultant waveguides are generally several microns wide [19], [20], as shown in Figure 3.1(a), and the refractive index contrast is relatively small ($\Delta n < 0.1$) [21] which leads to low optical confinement. Hence, the long Mach-Zehnder (MZ) arm lengths, large half-wave voltage-length product ($V_\pi \cdot l$), as well as high bending loss, restrict the exploitation of bulky LN EO modulators for desired large-scale photonic integration.

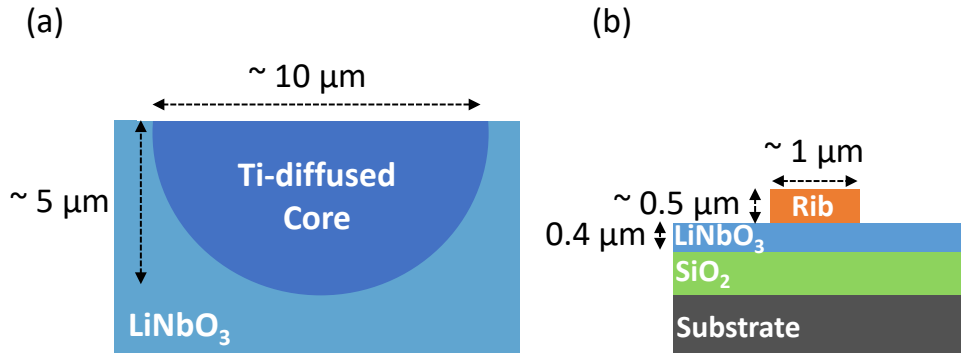


Figure 3.1: (a) Conventional LN waveguide; (b) Compact thin-film LN waveguide.

The heterogeneous integration of thin films of LN on oxidized Si substrates, has been recently demonstrated and pursued towards satisfying the requirement of large-scale integration, e.g., compact waveguide cross-sections, and low bending loss [22]. Our method has been to load the LN thin films with a rib waveguide made out of a refractive-index-matched material (such as tantalum pentoxide (Ta_2O_5) [22], chalcogenide glass (ChG) [23], or silicon nitride (Si_3N_4) [17]–[27]) in order to circumvent the LN etching issues and the associated high loss. It should be noted that low-loss LN etching has been recently demonstrated on LN thin films [10], [29]. Our team has also recently exploited direct etching of thin-film LN for highly efficient nonlinear-optic applications [12]. In any case, high optical confinement and low bending loss have been achieved by rib loading or direct etching, and as shown in Figure 3.1(b), typical waveguide core dimensions have been significantly reduced by almost 30 times, i.e., from $\sim 2 \times 6 \mu\text{m}^2$ for half-intensity widths in conventional LN waveguides [20] to $0.4 \times 1 \mu\text{m}^2$.

As a result of these submicron waveguides, the gap between the electrodes of the MZ modulator can be decreased significantly compared to the conventional LN devices without introducing additional loss due to absorption of the optical mode by metallic electrodes. By utilizing this platform, we have previously demonstrated compact thin-film LN MZ EO modulators on Si substrates with a 3-dB modulation BW of 33 GHz and operating up to 50 GHz [17].

Compact LN modulators are not limited to the rib-loading and thin-film method described above. A variety of other approaches have been pursued [31]–[39]. A detailed review of different approaches and advances in thin-film LN modulator technology is beyond the scope of this work and has been recently published [40].

With achieving this level of maturity for these emerging platforms, an accurate model is now required in order to design high-performance devices and predict their performance limits. Despite some early work in recognizing the effect of frequency-dependent impedance mismatch in travelling-wave EO modulator [41], the commonly employed models in the literature for conventional LN modulators do not consider this effect. In these models, impedance matching is typically assumed between the MZ EO modulator’s transmission line characteristics and the terminating resistive load at all frequencies [42], [43].

In this paper, we report on a much improved model in order to design, analyze and optimize the optical and RF device parameters of these compact (submicron) LN EO modulators. Electrical-optical modeling of the modulator based on coupled-mode theory is presented in Section II. In Section III, RF transmission-line modeling and calculation of its parameters by utilizing COMSOL™ simulations as well as conformal mapping technique is discussed. Moreover, calculations based on the transfer function which is developed by taking the impedance mismatch between the transmission line and the terminating load into account, are presented. Simulation results are presented in Section IV, and design guidelines are discussed. By comparing the developed model with experimental results, the accuracy of the model in predicting the frequency-dependent response of the EO modulators is verified. In addition, design optimizations for both RF and optical parameters of the EO modulator are investigated. The results predict significant improvement in the 3-dB BW of such devices. Finally, concluding remarks are given in Section V.

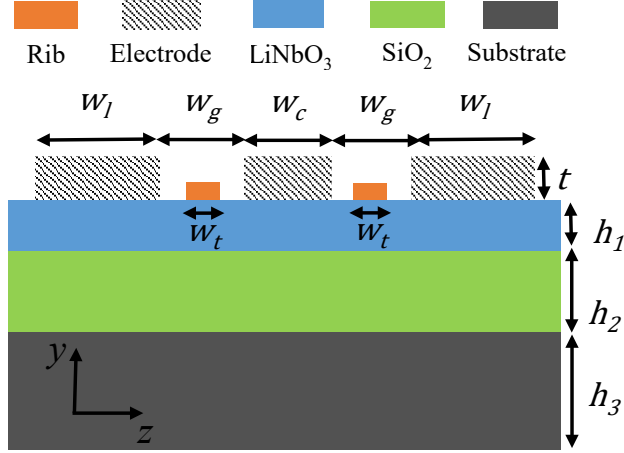


Figure 3.2: Two dimensional schematic of a typical thin-film LN MZ EO modulator.

3.2 Electrical - Optical Modeling

Figure 3.2 depicts the schematic cross-section of a generic thin-film LN MZ modulator in the push-pull configuration. The slab region of the optical waveguide is a X - or Y -cut thin-film of LN bonded to a layer of SiO_2 on silicon or LN substrate. As mentioned before, the thin-film LN is rib-loaded with an index-matched material, or directly etched, to provide lateral confinement for the optical mode. The applied RF electric field is aligned along the z -axis of LN. Hence, the strongest EO coefficient of LN crystal, i.e., $r_{33} \simeq 31$ pm/V [44], will be efficiently utilized.

Although this paper chooses the structure shown in Fig. 3.2 as a working example, the model developed here is more general and, in principle, can be applied to the other aforementioned compact LN platforms [31]–[39].

Based on Fig. 3.2, the effective refractive index along the z -direction is

$$n_z = n_e + \Delta n, \quad (3.1)$$

$$\Delta n = -n_e^3 r_{33} E_z^{RF} / 2, \quad (3.2)$$

where n_e is the extraordinary refractive index of LN, and E_z^{RF} is the total electric field applied along the z direction. Based on the coupled-mode theory, the change in the amplitude of the optical field inside the waveguide can be calculated as

$$E_z^{op}(x) = E_z^{op}(0)e^{-j\tilde{C}_{11}x}, \quad (3.3)$$

where superscript op indicates the optical field, \tilde{C}_{11} is the complex self-coupling coefficient defined as [44]

$$\tilde{C}_{11} = \Delta\tilde{\beta}_{op} = \omega_{op} \frac{\iint_S \Delta\tilde{\epsilon}(y, z)(\mathbf{E}_t^{op} \cdot \mathbf{E}_t^{op*}) ds}{\iint_S \hat{\mathbf{u}}_x \cdot (\mathbf{E}_t^{op*} \times \mathbf{H}_t^{op} + \mathbf{E}_t^{op} \times \mathbf{H}_t^{op*}) ds}, \quad (3.4)$$

and \mathbf{E}_t^{op} and \mathbf{H}_t^{op} are the transverse electric and magnetic field components of the optical wave propagating across the transverse surface S of the optical waveguide. $\hat{\mathbf{u}}_x$ is the unit vector along the direction of wave propagation. $\tilde{\epsilon}$ is the complex permittivity of the optical waveguide, and $\tilde{\beta}_{op}$ is the complex phase constant of the optical wave. Since

$$\tilde{\epsilon} = \epsilon_0 \tilde{n}^2, \quad (3.5)$$

and with $\tilde{n} = n + jn'$, the change in the permittivity is

$$\Delta\tilde{\epsilon} \approx 2n\epsilon_0\Delta n, \quad (3.6)$$

if the perturbation of the imaginary part of the refractive index is ignored. Then, equation (3.4) can be written as

$$\Delta\tilde{\beta}_{op} = \omega_{op} \frac{\iint_S 2n\epsilon_0\Delta n(\mathbf{E}_t^{op} \cdot \mathbf{E}_t^{op*}) ds}{\iint_S \hat{\mathbf{u}}_x \cdot (\mathbf{E}_t^{op*} \times \mathbf{H}_t^{op} + \mathbf{E}_t^{op} \times \mathbf{H}_t^{op*}) ds}. \quad (3.7)$$

For TE polarization

$$\iint_S \hat{\mathbf{u}}_x \cdot (\mathbf{E}_t^{op*} \times \mathbf{H}_t^{op} + \mathbf{E}_t^{op} \times \mathbf{H}_t^{op*}) ds = \frac{2\beta_{op}}{\omega_{op}\mu_0} \iint_S \mathbf{E}_t^{op} \cdot \mathbf{E}_t^{op*}, \quad (3.8)$$

and

$$\Delta\tilde{\beta}_{op} = \frac{-k_0^2 r_{33} n_e^4 \iint_S E_z^{RF} (\mathbf{E}_t^{op} \cdot \mathbf{E}_t^{op*}) ds}{2\beta_{op} \iint_S \mathbf{E}_t^{op} \cdot \mathbf{E}_t^{op*} ds}. \quad (3.9)$$

Since we have neglected the change in the imaginary part of the refractive index, $\Delta\tilde{\beta}_{op}$ is approximately a real value, expressed as

$$\Delta\beta_{op} = \Delta n_{op}^{eff} k_0, \quad (3.10)$$

where k_0 is the vacuum wavenumber. By using equation (3.2) and (3.7), the perturbation to the optical effective index is

$$\Delta n_{op}^{eff} = \frac{-k_0 n_e^4 r_{33} \iint_S E_z^{RF} (\mathbf{E}_t^{op} \cdot \mathbf{E}_t^{op*}) ds}{2\beta_{op} \iint_S \mathbf{E}_t^{op} \cdot \mathbf{E}_t^{op*} ds}. \quad (3.11)$$

In general, the RF field can be written as

$$E_z^{RF}(y, z) = \frac{V}{d} f(y, z). \quad (3.12)$$

The voltage V is a DC voltage for the lumped modulators, and it is a time-varying signal for traveling-wave EO modulators. d is the distance between the two metallic electrodes. $f(y, z)$ is the normalized spatial distribution of the electric field applied at the optical waveguide transverse plane. By defining the overlap of the electrical and optical fields as

$$\Lambda = \frac{\iint_S f(y, z) (\mathbf{E}_t^{op} \cdot \mathbf{E}_t^{op*}) ds}{\iint_S \mathbf{E}_t^{op} \cdot \mathbf{E}_t^{op*} ds}, \quad (3.13)$$

equation (3.11) can be written as

$$\Delta n_{op}^{eff} = \Delta n_0 V, \quad \Delta n_0 = \frac{-k_0 r_{33} n_e^4 \Lambda}{2\beta_{op} d}. \quad (3.14)$$

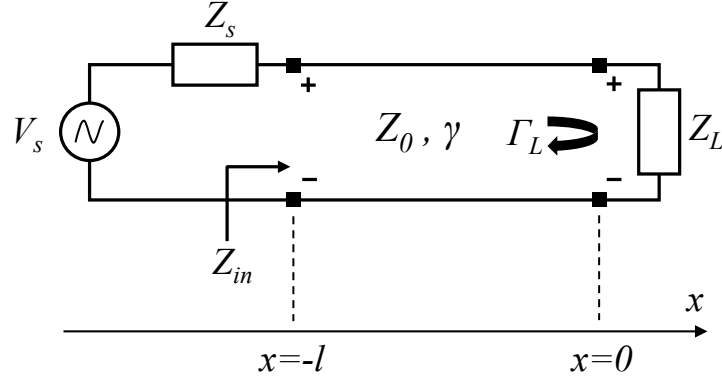


Figure 3.3: Schematic of a general transmission line model. V_s is the source voltage with the impedance Z_S . The transmission line is terminated with a load with impedance Z_L . Z_0 and γ are characteristic impedance and complex propagation constant of the transmission line, respectively. The transmission line is along the x -axis.

3.3 RF Transmission Line Modeling

As shown schematically in Fig. 3.2, the RF transmission line employed in the EO modulators is a symmetric coplanar waveguide (CPW) structure [21]. The signal is applied to the middle conductor and the other two conductors are ground planes (Ground-Signal-Ground (GSG) configuration). The main transmission line parameters of a CPW structure are the characteristic impedance (Z_0), attenuation constant (α_{RF}) and effective phase constant (β_{RF}). The standard lumped-element model of a transmission line [45] can be used to model the RF performance of the travelling-wave EO modulator, as depicted in Fig. 3.3. γ is the complex propagation constant, Z_0 is the characteristic impedance of the transmission line, and Z_{in} is the input impedance seen at the input of the transmission line with length l . Γ_L is the reflection coefficient due to the mismatch between Z_0 and the terminating resistive load (Z_L), and is defined as [45]

$$\Gamma_L = \frac{Z_L - Z_0}{Z_L + Z_0}. \quad (3.15)$$

Based on general transmission line theory, the voltage at each point of the transmission line is

$$V(x) = V_0^+ e^{\gamma x} + V_0^- e^{-\gamma x} = V_0^+ (e^{-\gamma x} + \Gamma_L e^{+\gamma x}). \quad (3.16)$$

The voltage at the beginning of the line is calculated as

$$V(-L) = V_0^+ (e^{\gamma L} + \Gamma_L e^{-\gamma L}) = V_S \frac{Z_{in}}{Z_{in} + Z_S}. \quad (3.17)$$

Then, we can find V_0^+ in terms of the source voltage as

$$V_0^+ = V_S \frac{Z_{in}}{Z_{in} + Z_S} \frac{1}{e^{\gamma l} + \Gamma_L e^{-\gamma l}}. \quad (3.18)$$

In the ideal case, in which both source and load impedances are matched to the line impedance ($Z_L = Z_0, Z_{in} = Z_0$),

$$\Gamma_L = 0, V_0^+ = V_S \frac{Z_0}{Z_0 + Z_S}. \quad (3.19)$$

However, this ideal case is almost impossible to achieve in practice across a broad RF band, as discussed later in Section III. Hence, it is necessary to introduce the effect of the impedance mismatch into the modeling.

As derived in the Appendix, the frequency-dependent transfer function of any EO modulator is

$$H(\omega_{RF}) = \frac{Z_{in}}{Z_{in} + Z_S} \frac{1}{e^{\gamma l} + \Gamma_L e^{-\gamma l}} \left[\frac{\sinh(A/2) e^{-A/2}}{A/2} + \Gamma_L \frac{\sinh(B/2) e^{-B/2}}{B/2} \right], \quad (3.20a)$$

$$A = -\alpha_{RF} - j\omega_{RF}(n_{RF} - n_{op})/c, \quad (3.20b)$$

$$B = +\alpha_{RF} + j\omega_{RF}(n_{RF} + n_{op})/c. \quad (3.20c)$$

where n_{RF} and n_{op} are the RF and optical wave refractive indices, respectively.

Equation (3.20) accounts for the RF attenuation coefficient, the phase velocity mismatch of the RF and optical traveling waves and the impedance mismatch between Z_S and Z_0 . Moreover, unlike the conventional models [43], the impedance mismatch between the transmission line and the terminating load for the operating range has been taken into account.

In comparison, the commonly employed model for predicting the RF frequency response of the EO modulators is [43]

$$H(\omega_{RF}) = \frac{Z_{in}}{Z_{in} + Z_S} e^{-\alpha_{RF}l/2} \left[\frac{\sinh^2(\alpha_{RF}l/2) + \sin^2(\omega_{RF}(n_{RF} - n_{op})l/2c)}{(\alpha_{RF}l/2)^2 + (\omega_{RF}(n_{RF} - n_{op})l/2c)^2} \right]^{1/2}. \quad (3.21)$$

In this conventional model, impedance matching between Z_0 and Z_L is assumed at all frequencies. As shown later in this work, this assumption is not valid for compact EO modulators, and leads to overestimation of the 3-dB BW. The comparison between these two approaches are presented in Section IV.

Next, the main parameters of the RF transmission line, i.e. Z_0 , n_{RF} , and α_{RF} are calculated as follows.

3.3.1 Characteristic Impedance

The characteristic impedance of the modulator is calculated by using COMSOLTM simulations. Based on the quasi-Transverse Electromagnetic analysis of the CPW structure, RF electric and magnetic fields (denoted by \mathbf{E}_{RF} and \mathbf{H}_{RF} respectively) are used to calculate the resistance (R), inductance (L), conductance (G), and capacitance (C) circuit parameters per unit length for the

CPW structure. The standard elements are calculated as [45]

$$\begin{aligned} R &= \frac{R_S}{I^2} \int_l \mathbf{H}_{RF} \cdot \mathbf{H}_{RF}^* dl, L = \frac{\mu_0}{I^2} \int_S \mathbf{H}_{RF} \cdot \mathbf{H}_{RF}^* ds, \\ G &= \frac{\omega_{RF} \epsilon''}{V^2} \int_S \mathbf{E}_{RF} \cdot \mathbf{E}_{RF}^* ds, C = \frac{\tilde{\epsilon}}{V^2} \int_S \mathbf{E}_{RF} \cdot \mathbf{E}_{RF}^* ds \end{aligned} \quad (3.22)$$

where R_S is the surface resistance of the metal electrodes, ϵ'' is the imaginary part $\tilde{\epsilon}$, V is the potential difference between the CPW electrodes, and I is the current flowing in the electrode. Then, the frequency-dependent Z_0 is calculated as

$$Z_0 = \sqrt{\frac{R + j\omega_{RF}L}{G + j\omega_{RF}C}}. \quad (3.23)$$

The characteristic impedance of a CPW with a GSG configuration and multilayered substrate can be also obtained by using the conformal mapping technique as [46]

$$Z_0 = \frac{K'(k)}{4\epsilon_0 c K(k) \sqrt{\epsilon_{RF}^{eff}}}, \quad (3.24)$$

where c is the velocity of electromagnetic waves in free space, ϵ_{RF}^{eff} is the effective dielectric constant of the transmission line and $k = x_a/x_b$, where $x_a = W_c/2$, $x_b = W_c/2 + W_g$, $x_c = W_c/2 + W_g + W_l$. $K(\cdot)$ and $K'(\cdot)$ are the complete elliptic integrals of the first kind and its complement, respectively. The effective dielectric constant is

$$\epsilon_{RF}^{eff} = 1 + \sum_1^3 q_i, \quad (3.25)$$

where q_i is the filling factor, and 1, 2, and 3 correspond to LN, SiO₂ bottom cladding and substrate

layers, respectively, as shown in Fig. 3.2. For $i = 1$ and 2 , q_i is defined as [46], [47]

$$q_i = \frac{1}{2}(\epsilon_{r,i} - \epsilon_{r,i+1}) \frac{K(k)K(k'_i)}{K(k')K(k_i)}, \quad (3.26)$$

where

$$k_i = \frac{\sinh(\pi x_c/2h_i)}{\sinh(\pi x_b/2h_i)} \sqrt{\frac{\sinh^2(\pi x_b/2h_i) - \sinh^2(\pi x_a/2h_i)}{\sinh^2(\pi x_c/2h_i) - \sinh^2(\pi x_a/2h_i)}}, \quad (3.27)$$

$$k'_i = \sqrt{1 - k_i^2},$$

and for the substrate layer

$$q_3 = \frac{1}{2}(\epsilon_{r,3} - 1) \frac{K(k)K(k'_3)}{K(k')K(k_3)}, \quad (3.28)$$

where

$$k = \frac{x_c}{x_b} \sqrt{\frac{x_b^2 - x_a^2}{x_c^2 - x_a^2}}, k' = \sqrt{1 - k^2}. \quad (3.29)$$

The frequency variation of the ϵ_{RF}^{eff} is calculated as

$$\epsilon_{RF}^{eff}(f) = \left[\sqrt{\epsilon_{RF}^{eff}(0)} + \frac{\sqrt{\epsilon_r} - \sqrt{\epsilon_{RF}^{eff}(0)}}{1 + G(f/f_{TE})^{-1.8}} \right]^2, \quad (3.30)$$

where

$$G = \exp(u \ln(W_c/W_g) + v),$$

$$u = 0.54 - 0.64p + 0.015p^2,$$

$$v = 0.43 - 0.86p + 0.54p^2, \quad (3.31)$$

$$p = \ln(W_c/h),$$

$$f_{TE} = c/4h\sqrt{\epsilon_r - 1},$$

and $h = h_1 + h_2 + h_3$ in the current structure and $\epsilon_r = \sum_{i=1}^3 \epsilon_{r,i}/3$.

It is worth mentioning that the values of the characteristic impedance and the effective permittivity obtained here are valid for infinitesimally thin CPW metallic strip conductors. As shown

in Fig. 3.2, in practice, the metallization has a finite thickness t that affects the characteristics. It has been observed that as the metal thickness is increased, characteristic impedance and effective permittivity are both decreased consequently, but in the case $t/w_c \ll 1$, the effect of metal thickness can be neglected [46].

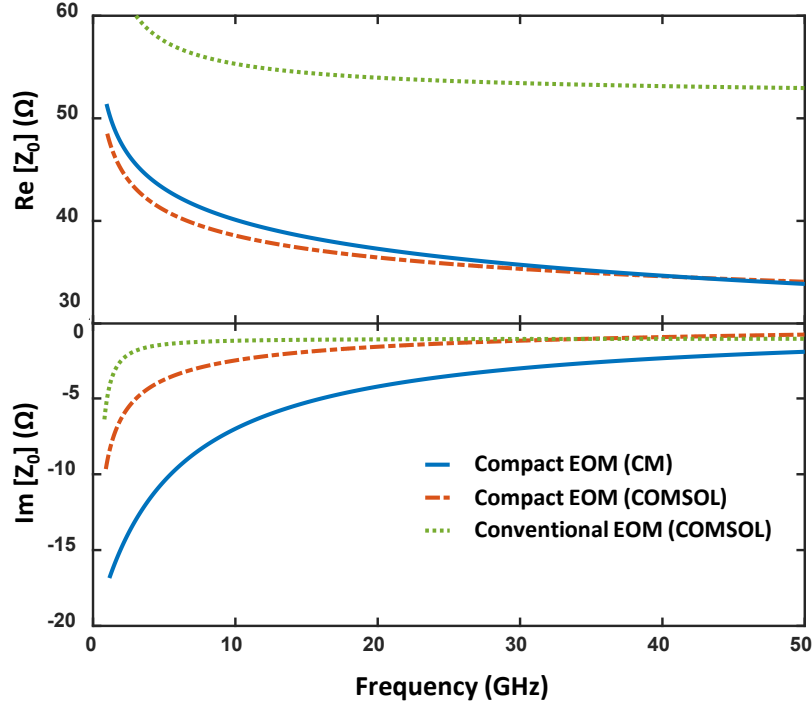


Figure 3.4: Comparison between the calculated real part, and imaginary part of the characteristic impedance (Z_0) of the example electrooptic modulator (EOM) using conformal mapping (CM) and COMSOLTM simulations vs. the conventional bulk modulator for the operating frequency range.

The structure shown in Fig. 3.2 is used as an example with $l = 8$ mm. The characteristic impedance of the modulator with dimensions $W_g = 5.5 \mu\text{m}$, $W_c = 12 \mu\text{m}$, $W_l = 8.5 \mu\text{m}$, $W_t = 1.2 \mu\text{m}$, $t = 2 \mu\text{m}$, $h_1 = 400$ nm, $h_2 = 2 \mu\text{m}$, and $h_3 = 500 \mu\text{m}$ for Si substrate is calculated using COMSOLTM simulations and the conformal mapping method described above with calculated filling factors of 0.35, 0.01, and 0.001 for q_1 , q_2 , and q_3 , respectively, for Si substrate. For the case of LN substrate, $\epsilon_{r,3}$ in Eq. (3.28) is about three times higher than that of Si, but q_3 is still a small factor. The results agree with negligible difference, i.e., $\sim 5\%$ of each other (For example

$Z_0 = 48.38 \Omega$ using COMSOLTM simulations (Eq. (3.23)), and $Z_0 = 50.7 \Omega$ calculated using the conformal mapping method (Eq. (3.24)), both calculated at 1 GHz frequency). The trends versus RF frequency (0 to 50 GHz) are presented in Fig. 3.4, and Fig. 3.5 for Z_0 and n_{RF} , respectively.

It is evident that the Z_0 of the compact modulator in the example varies from $\sim 50 \Omega$ to $\sim 35 \Omega$ as the frequency is increased from DC to 50 GHz, whereas the characteristic impedance of the conventional bulk LN modulators remains almost invariant for the most part of the operating frequency range [48]. This is confirmed through our COMSOLTM simulations by using structure in Fig. 3.2 with $W_g = W_l = W_c = 20 \mu\text{m}$, and $t = 5 \mu\text{m}$ on bulk LN substrate which resembles a typical conventional LN modulator. Shown also in Fig. 3.4, this clearly shows the importance of impedance matching between the modulator and the terminating load, in the case of the compact modulators.

3.3.2 RF Attenuation Constant

The RF attenuation constant is another important design parameter which should be carefully studied. As discussed later in Section IV, it plays an important role in predicting the frequency response of the EO modulator and its BW. The attenuation constant of the CPW structure is generally defined as

$$\alpha_{RF} = \alpha_c + \alpha_d + \alpha_r, \quad (3.32)$$

where α_c is the ohmic or metallic conductor attenuation constant, α_d is the dielectric attenuation constant and α_r is the radiation attenuation constant. The dimensions of α_c , α_d and α_r are dB per unit length. Here, with smooth metal deposition for electrodes, α_r is neglected. The expressions for the attenuation constant due to dielectric loss in CPW structure is the same as that for a microstrip, which is [46]

$$\alpha_d = \frac{2.73}{c} \frac{\epsilon_r}{\sqrt{\epsilon_{RF}^{eff}}} \frac{\epsilon_{RF}^{eff} - 1}{\epsilon_r - 1} (\tan \delta) f, \quad (3.33)$$

where $\tan \delta$ is called the dielectric loss tangent, and it is taken from [49], [50], and [51] for SiN, LN, and SiO₂, respectively.

The ohmic loss is calculated by evaluating the power dissipated in the line through conformal mapping of the current density in the finite metal thickness structure [52] as $\alpha_c = \alpha_{c0}\sqrt{f}$, where α_{c0} is defined as

$$\alpha_{c0} = \frac{R_{s0}\sqrt{\epsilon_{RF}^{eff}}}{480\pi K(k)K'(k)(1-k^2)} \left[\frac{1}{x_b} \left(\pi + \ln \left(\frac{8\pi x_a(1-k)}{t(1+k)} \right) \right) + \frac{1}{x_b} \left(\pi + \ln \left(\frac{8\pi x_b(1-k)}{t(1+k)} \right) \right) \right], \quad (3.34)$$

where R_{s0} is the surface resistance of the strip conductor at low frequencies. The transformation rule used for calculating elliptic integrals is

$$K(k) = (1+k_s)K(k_s), K(k') = \frac{1+k_s}{2}K(k'_s), \quad (3.35)$$

where

$$k_s = x_a/x_b, k'_s = \sqrt{1-k_s^2}, k = \frac{2\sqrt{k_s}}{1+k_s}, k' = \frac{1-k_s}{1+k_s}. \quad (3.36)$$

The RF attenuation and both parts of it, i.e., α_c and α_d , are depicted in Fig. 3.5 for the example modulator discussed in the previous section $l = 8$ mm. Clearly, α_d cannot be neglected at high frequencies.

3.4 Simulation Results and Discussions

RF and optical mode profiles of the EO modulator structure of Fig. 3.2 are simulated using COMSOLTM and presented in Fig. 3.6. In this structure, more than 70% of the optical mode is confined within the LN thin film for Si₃N₄ rib with an index of 1.93 at 1550 nm. The evident high lateral optical confinement compared to conventional LN devices allows for reduced electrode gaps of 5.5 μ m,

and reduction in device's overall footprint, without introducing additional absorption of the optical mode by metallic electrodes. Meanwhile, the high lateral confinement of the electric field in LN provides negligible optical loss at the sharp Y -junctions of the MZ modulator, and more importantly, a desired overlap of the RF and optical field, which leads to lower drive voltages compared to traditional bulky LN modulators, and consequently a lower $V_{\pi} \cdot l$, which is an important figure of merit for EO modulators. By further increasing the optical mode overlap in LN, the drive voltage can be reduced. However, this simultaneously results in lower lateral confinement and can potentially increase the electrode-induced optical loss, and consequently degrades the overall performance of the device [40]. Therefore, this trade-off should be considered carefully in the design procedure.

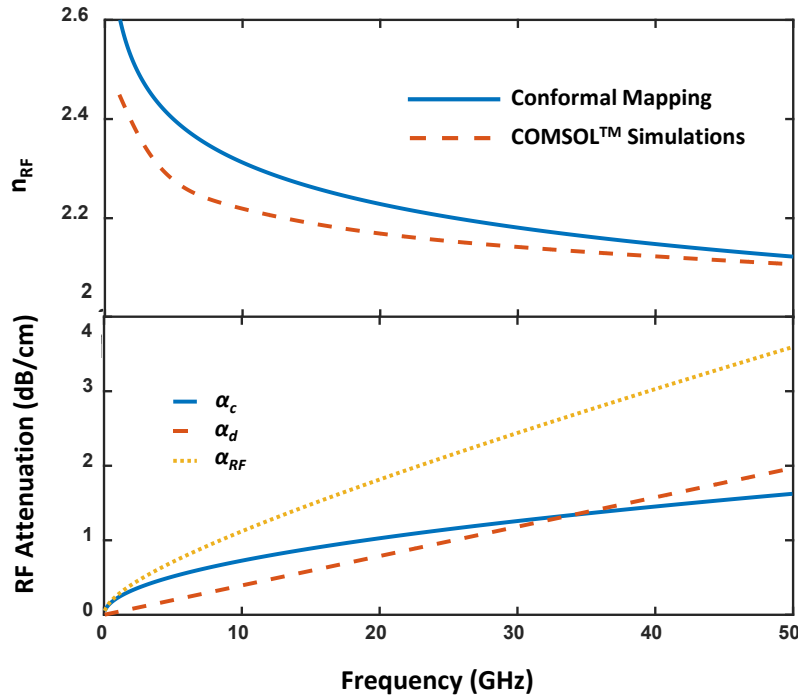


Figure 3.5: Calculated RF refractive index (n_{RF}) of the example modulator using conformal mapping and COMSOL[™] simulations, and α_c , α_d , and α_{RF} by using conformal mapping method.

It is observed that the effective refractive index of the optical waveguide plays an important role in the final RF performance of the modulator, i.e., in the frequency-dependent velocity

mismatch between the RF and optical modes (see Eq. (3.20)). Since the effective refractive index of the RF guided mode (n_{RF}) decreases with RF frequency, as depicted in Fig. 3.5, while the optical refractive index (n_{op}^{eff}) remains constant, the mismatch between these two indices should be minimized as much as possible, by using the n_{rib} value to tune n_{op}^{eff} (see Figs. 3.7 and 3.8(a)).

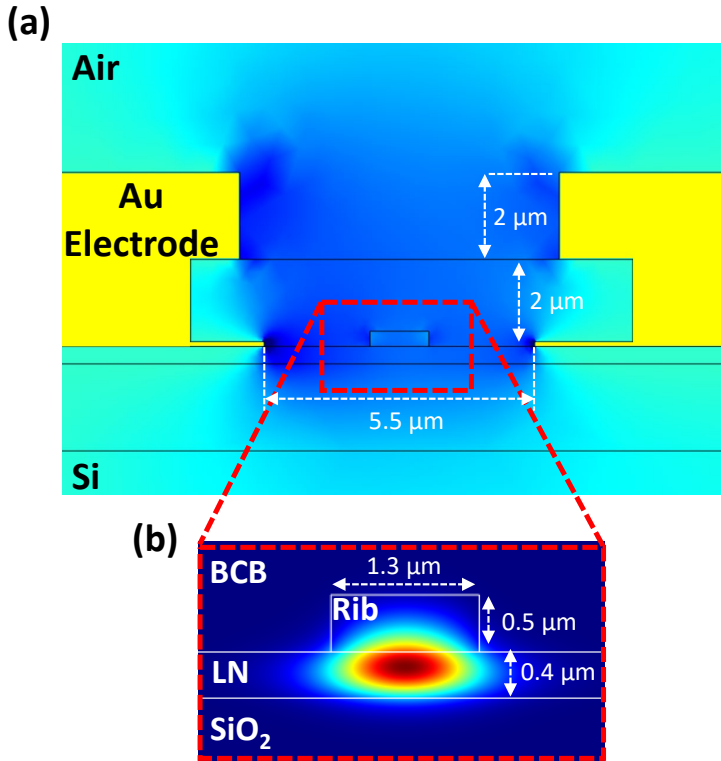


Figure 3.6: (a) Simulated RF mode profile of MZ modulator with 5.5 μm gap between the electrodes at 10 GHz.; (b) Simulated optical mode profile of the hybrid ridge waveguide with Si₃N₄ rib.

In order to study the range of achievable values for n_{op}^{eff} , the optical waveguide region of the compact EO modulator in Fig. 3.6 is simulated using COMSOLTM and the results are presented in Fig. 3.7. The height and width of the rib is varied for three different rib-loading materials with optical refractive indices of $n_{rib} = 1.9, 2.0,$ and 2.2 , as an example (the case $n_{rib} = 2.2$ corresponds to LN). The height of the thin-film LN is fixed at 400 nm in the simulations. The acquired values for n_{op}^{eff} are utilized in Eq. (3.20) for $l = 8$ mm, and the EO frequency response of the modulator

is depicted in Fig. 3.8(a). With the same waveguide cross-section, increasing n_{rib} results in higher BW and lower W_g , as observed in Fig. 3.8(a), and Fig. 3.8(b). For example, an all-LN platform, achieved by direct etching of LN ($n_{rib} = 2.2$) has higher BW compared to rib-loaded LN with rib indices lower than 2.2, while rib-loading with a material with a higher index of 2.3 would offer the highest BW.

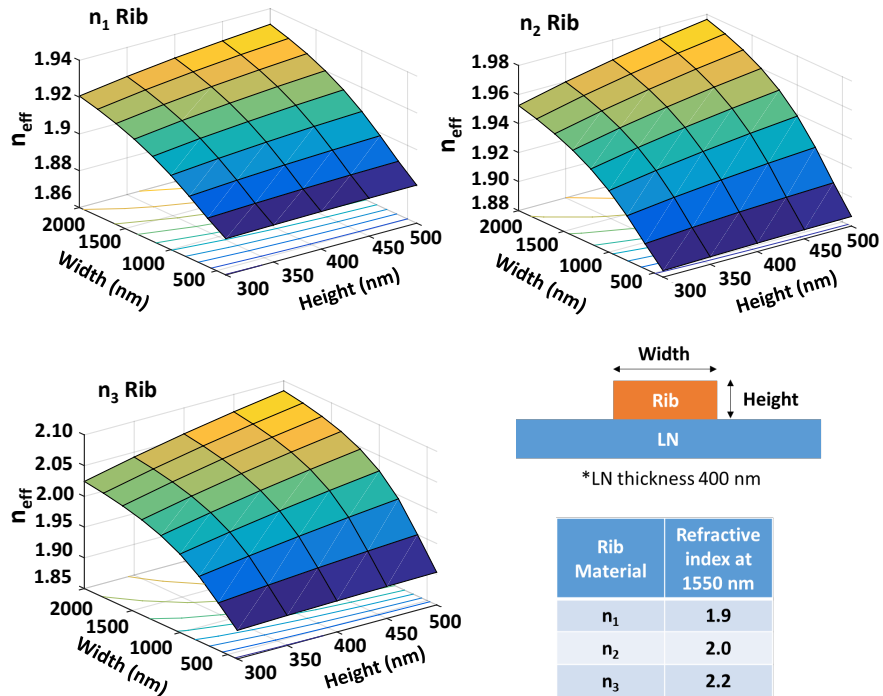


Figure 3.7: Calculated effective refractive indices of optical waveguide of the modulator for 3 different rib-loading materials as examples. The height and width of the rib is varied. The thin-film LN thickness is 400 nm. The inset table shows the assumed refractive indices of rib-loading materials.

It is evident that by employing the appropriate rib-loading material and optical waveguide dimensions, the 3-dB BW of the modulator can be improved significantly. It is observed that these degrees of freedom in using waveguide index, and dimensions are not easily attainable in traditional diffused LN modulators. As discussed later, the device length is also an important parameter, and 100 GHz BW is predicted with $l = 3$ mm (see Fig. 3.9(b)).

It should be noted that these simulation results are for the particular CPW electrode struc-

ture of Fig. 3.2. Other configurations for electrodes will vary the n_{RF} of the device and hence, require appropriate re-designing of the optical parameters. It is also important to mention that by changing the rib-loading material or the optical waveguide dimensions, the lateral confinement of the optical mode will vary. Therefore, the gap between the electrodes has to be designed accordingly in order to avoid the metal-induced additional loss.

Figure 3.8(b) presents optical loss vs. W_g for different rib-loading materials to show the trade-off between loss and confinement. It is stressed that optical loss values only account for the metallic electrodes and ignore the material loss of LN and the rib-loading materials, as well as any fabrication-dependent sidewall scattering loss. Figure 3.8(b) suggests that employing a rib-loading material with higher refractive index yields shorter gaps and consequently more compact and lower-voltage devices. With large enough W_g , metal-induced absorption loss is negligible, and the overall transmission of the EO modulator is maximized. Meanwhile, the optical propagation loss does not affect the frequency response of the modulator, and its 3-dB BW. On the other hand, the RF loss plays a key role in determining the performance limits of the modulator, and as mentioned before, it should be carefully studied.

Here, a comparison between the driving voltage of rib-loading versus direct etching of LN is presented. Directly-etched LN waveguides clearly have higher optical mode overlap with the active region and the mode is more confined. Also, with an index of 2.2 for LN, directly-etched devices can afford smaller W_g compared to $n_{rib} < 2.2$ for the same metallic loss. For example, the data in Fig. 3.8(b) suggests that for a loss of 1 dB/cm, $W_g = 3.7 \mu\text{m}$ for $n_{rib} = 2.2$ (LN) and $W_g = 5.1 \mu\text{m}$ for $n_{rib} = 2.0$. However, as also pointed out elsewhere [40], the RF electric field drops in both the rib and the LN active region, as the dielectric constant of the rib material increases. Consequently, the overlap of the electric and optical fields, Λ in Eq. 3.13, drops and to some extent counteracts the shorter W_g in $V_\pi \cdot l$ calculations. For instance, in the same example described above, Λ is 64% for $n_{rib} = 2.2$ (LN) and 67% for $n_{rib} = 2.0$. Accordingly, the final $V_\pi \cdot l$ values are 2.93 and 3.82 V.cm, respectively.

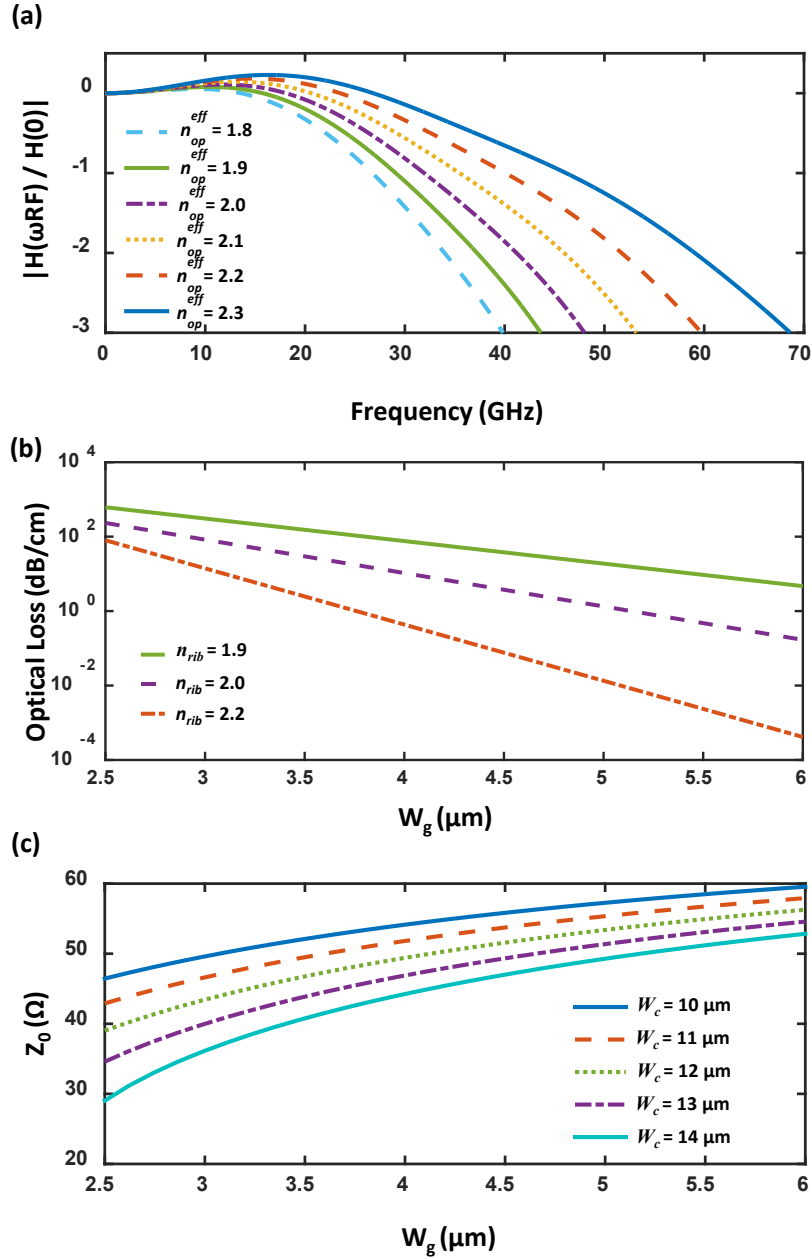


Figure 3.8: (a) Variation of the normalized frequency dependent response of the EO modulator for different values of effective optical refractive index, n_{op}^{eff} .; (b) Simulated optical loss vs. the gap between the electrodes (W_g) for 3 different rib-loading materials as an example.; (c) Characteristic impedance (Z_0) vs. the gap between the electrodes (W_g) for different values of the center electrode's width (W_c).

As discussed earlier, one important issue neglected in traditional models is the impedance mismatch between the characteristic impedance of the modulator (Z_0) and the terminating $50\text{-}\Omega$ resistive load. This mismatch has been taken into account in our developed model as denoted by Γ_L in Eq. (3.20). While Z_0 varies with RF frequency, the CPW electrodes structure of the modulator is designed in such a way to maintain characteristic impedance as close as possible to $50\ \Omega$. Figure 3.8(c) shows the variation of Z_0 versus W_g for different widths of the center electrode, denoted by W_c in Fig. 3.2.

Finally, for the purpose of verification, the developed model is utilized to compare with the frequency-dependent response of a fabricated device in our previous work [17], i.e., the device with the cross-section shown in Fig. 3.6 and with $l = 8\ \text{mm}$. As shown in Fig. 3.9(a), the proposed model follows the experimental data and is capable of accurately predicting the 3-dB BW of the modulator. However, it can be observed that the characterization data and the frequency response resulted from the developed model do not match at low frequencies. One possible reason is that the wavelength of the RF signal is much greater than the transverse dimensions of the EO modulator in this frequency range. Hence, the peripheral apparatus such as the metallic holders or the optical test bench below can potentially affect the measured RF response of the device. Since these parasitic elements are not considered in this model, the accuracy of the model at lower frequencies could have been compromised. Further investigation of this attribution requires more detailed modeling, which is beyond the scope of this work.

The discrepancy between the conventional [43] and the proposed model (see Eq. (3.20)) is clearly apparent in Fig. 3.9(a). The result from conventional modeling considerably overestimates the 3-dB BW of the modulator. It is also observed that if α_d is neglected in the models, the performance predictions are no longer valid.

Accurate calculation of RF loss and refractive index, as well as taking the mismatch between Z_0 and Z_L into account are both required in order to properly predict the frequency response of the compact EO modulators.

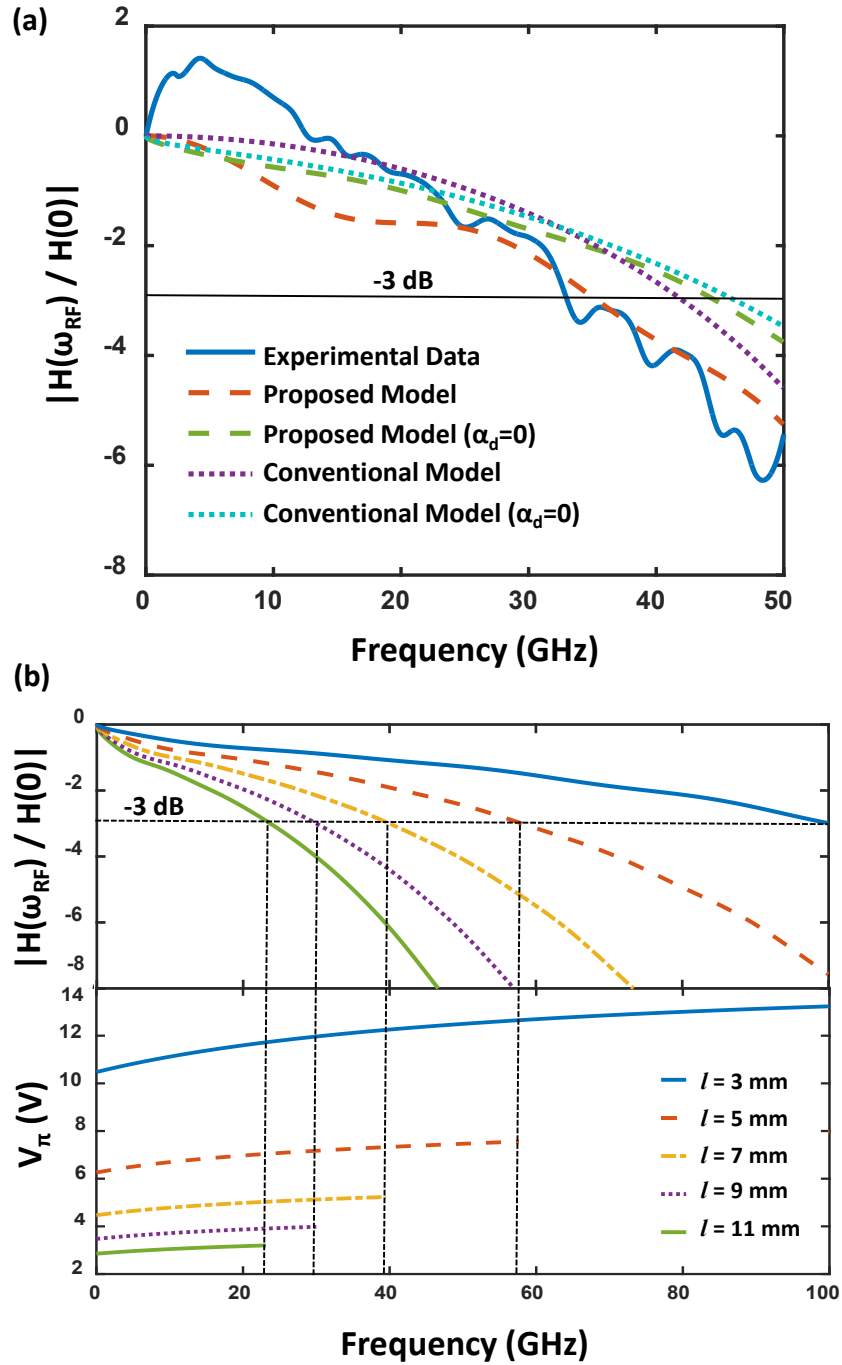


Figure 3.9: (a) Comparison between the experimental data [17] vs. the performance prediction from the developed (see Eq. (3.20)) as well as the conventional model [43].; (b) Variation of the simulated frequency response, and half-wave voltage (V_π) of the modulators for different lengths of RF electrodes vs. the RF frequency.

Finally, in order to further improve the 3-dB BW of the modulator, the optimized device length is studied. As shown in Fig. 3.9(b), shorter electrode lengths provide larger BW for the same designed structure of Fig. 3.6 [17], but with different l values. The results predict the potential for achieving 3-dB BW of 100 GHz for $l = 3$ mm. However, it should be noted that larger BW is attainable at the cost of increased half-wave voltage (V_π). The variation of V_π vs. RF frequency (DC to 3-dB BW) is depicted in Fig. 3.9(b) for different values of l .

3.5 Conclusions

In summary, we have developed a general transmission-line model that accurately predicts the frequency-dependent response of ultracompact (submicron) and high-speed electrooptic modulators. The major RF parameters of such devices are calculated as a function of coplanar waveguide dimensions. The design procedure of these compact modulators in terms of RF, as well as optical parameters are presented, and the model is utilized to analyze and optimize the high-speed performance of such devices. Finally, the accuracy of the model is verified by comparing the results with the characterization data obtained from fabricated devices. Unlike conventional models, the developed model presented in this work, is capable of accurately predicting the 3-dB bandwidth of ultracompact LN EO modulators. By utilizing this model, and with proper design of such compact EO modulators, the 3-dB modulation bandwidth can be improved to > 100 GHz, which is an important attribution for advanced optical communication systems.

3.6 Appendix

Formulations for calculating the proposed frequency-dependent transfer function of the EO modulator, Eq. (3.20), are developed in the following.

The complex propagation constant of the RF transmission line is defined as

$$\gamma = \alpha_{RF} + j\beta_{RF}. \quad (\text{A.1})$$

where the real part of the propagation constant, α_{RF} , is the attenuation constant and the imaginary part, β_{RF} , is the phase constant of the transmission line.

In general, the total phase shift of the optical field along the the electrode length l which the RF transmission line is presented is

$$\Delta\Phi_{op} = \Delta\Phi(\omega_{RF}, t) = \int_{-l}^0 \Delta\beta_{op} dx, \quad (\text{A.2})$$

where $\Delta\beta_{op}$ is defined as

$$\Delta\beta_{op} = k_0 \Delta n_{op}^{eff}. \quad (\text{A.3})$$

Then, using Eq. (3.14)

$$\Delta\beta_{op} = k_0 \Delta n_0 V(x, t + \frac{x}{v_{op}^p}), \quad (\text{A.4})$$

where v_{op}^p is the phase velocity of the optical wave and is defined as

$$v_{op}^p = \omega_{op} / \beta_{op} = c / n_{op}^{eff}. \quad (\text{A.5})$$

The voltage of the transmission line in Fig. 3.3 which is time- and frequency-dependent can be written as

$$V(x, t + \frac{x}{v_{op}^p}) = V_0^+ [e^{-\gamma x} + \Gamma_L e^{+\gamma x}] e^{j\omega_{RF}(t+x/v_{op}^p)}. \quad (\text{A.6})$$

If we define the transfer function, $H(\omega_{RF})$, via

$$\Delta\Phi_{op} = k_0 \Delta n_0 H(\omega_{RF}) e^{j\omega_{RF} t} V_S, \quad (\text{A.7})$$

then, $H(\omega_{RF})$ is

$$H(\omega_{RF}) = \int_{-l}^0 V_0^+ / V_S \left[e^{-\alpha_{RF}x} e^{-j\omega_{RF}(n_{RF}-n_{op})x/c} + \Gamma_L \left(e^{-\alpha_{RF}x} e^{+j\omega_{RF}(n_{RF}+n_{op})x/c} \right) \right] dx. \quad (\text{A.8})$$

After integration, Eq. (3.20) is derived.

3.7 References

- [1] D. Botez and G. J. Herskowitz, “Components for optical communications systems: A review,” *Proc. IEEE*, vol. 68, no. 6, pp. 689–731, 1980.
- [2] R. -J. Essiambre and R. W. Tkach, “Capacity trends and limits of optical communication networks,” *Proc. IEEE*, vol. 100, no. 5, pp. 1035–1055, 2012.
- [3] D. A. B. Miller, “Optical interconnects to electronic chips,” *Appl. Opt.*, vol. 49, no. 25, pp. F59–F70, 2010.
- [4] L. A. Eldada, “Advances in telecom and datacom optical components,” *Opt. Eng.*, vol. 40, no. 7, pp. 1165–1178, 2001.
- [5] R. Williamson and R. Esman, “RF Photonics,” *J. Lightwave Technol.*, vol. 26, no. 9, pp. 1145–1153, 2008.
- [6] B. Jalali and S. Fathpour, “Silicon photonics,” *IEEE J. Light. Technol.*, vol. 24, no. 12, pp. 4600–4615, 2006.
- [7] G. T. Reed, G. Z. Mashanovich, F. Y. Gardes, M. Nedeljkovic, Y. Hu, D. J. Thomson, K. Li, P. R. Wilson, S. -W. Chen, and S. S. Hsu, “Recent breakthroughs in carrier depletion based silicon optical modulators,” *Nanophotonics*, vol. 3, no. 4–5, pp. 229–245, 2014.
- [8] R. A. Soref and B. R. Bennett, “Electrooptical effects in silicon,” *IEEE J. Quantum Electron.*, vol. 23, no. 1, pp. 123–129, 1987.

- [9] Y. Tang, H. -W. Chen, S. Jain, J. D. Peters, U. Westergren, and J. E. Bowers, “50 Gb/s hybrid silicon traveling-wave electroabsorption modulator,” *Opt. Exp.*, vol. 19, no. 7, pp. 5811–5816, 2011.
- [10] O. Qasaimeh, P. Bhattacharya, and E. T. Croke, “SiGe-Si quantum-well electroabsorption modulators,” *IEEE Photon. Technol. Lett.*, vol. 10, no. 6, pp. 807–809, 1998.
- [11] J. Liu, M. Beals, A. Pomerene, S. Bernardis, R. Sun, J. Cheng, L. C. Kimerling, and J. Michel, “Waveguide-integrated ultralow-energy GeSi electro-absorption modulators,” *Nat. Photon.*, vol. 2, pp. 433–437, 2008.
- [12] S. Fathpour, “Emerging heterogeneous integrated photonic platforms on silicon,” *Nanophotonics*, vol. 4, no. 1, pp. 143–164, 2015.
- [13] X. Tu, T. Liow, J. Song, X. Luo, Q. Fang, M. Yu, and G. Lo, “50-Gb/s silicon optical modulator with traveling-wave electrodes,” *Opt. Express*, vol. 21, no. 10, pp. 12776–12782, 2013.
- [14] Y. Yang, Q. Fang, M. Yu, X. Tu, R. Rusli, and G. Lo, “High-efficiency Si optical modulator using Cu travelling-wave electrode,” *Opt. Express*, vol. 22, no. 24, pp. 29978–29985, 2014.
- [15] E. L. Wooten, K. M. Kissa, A. Yi-Yan, E. J. Murphy, D. A. Lafaw, P. F. Hallemeier, D. Maack, D. V. Attanasio, D. J. Fritz, G. J. McBrien, and D. E. Bossi, “A review of lithium niobate modulators for fiber-optic communications systems,” *IEEE J. Quant. Elec.*, vol. 6, no. 1, pp. 69–82, 2000.
- [16] K. Noguchi, O. Mitomi, and H. Miyazawa, “Millimeter-wave Ti:LiNbO₃ optical modulators,” *IEEE J. Light. Technol.*, vol. 16, no. 4, pp. 615–619, 1998.
- [17] M. Doi, M. Sugiyama, K. Tanaka, and M. Kawai, “Advanced LiNbO₃ optical modulators for broadband optical communications,” *IEEE J. Sel. Top. Quantum Electron.*, vol. 12, no. 4, pp. 745–750, 2006.

- [18] J. L. Jackel, C. E. Rice, and J. J. Veselka, "Proton exchange for high-index waveguides in LiNbO₃," *Appl. Phys. Lett.*, vol. 41, no. 7, pp. 607–608, 1982.
- [19] P. G. Suchoski, T. K. Findakly, and J. Leonberger, "Stable low-loss proton-exchanged LiNbO₃ waveguide devices with no electro-optic degradation," *Opt. Lett.*, vol. 13, no. 11, pp. 1050–1052, 1988.
- [20] M. Fukuma, and J. Noda, "Optical properties of titanium-diffused LiNbO₃ strip waveguides and their coupling-to-a-fiber characteristics," *Appl. Opt.*, vol. 19, no. 4, pp. 591–597, 1980.
- [21] A. Yi-Yan, "Index instabilities in proton-exchanged LiNbO₃ waveguides," *Appl. Phys. Lett.*, vol. 42, no. 8, pp. 633–635, 1983.
- [22] P. Rabiei, J. Ma, S. Khan, J. Chiles, and S. Fathpour, "Heterogeneous lithium niobate photonics on silicon substrates," *Opt. Express*, vol. 21, no. 21, pp. 25573–25581, 2013.
- [23] A. Rao, A. Patil, J. Chiles, M. Malinowski, S. Novak, K. Richardson, P. Rabiei, and S. Fathpour, "Heterogeneous microring and Mach-Zehnder modulators based on lithium niobate and chalcogenide glasses on silicon," *Opt. Express*, vol. 23, no. 17, pp. 22746–22752, 2015.
- [24] A. Rao, A. Patil, P. Rabiei, A. Honardoost, R. DeSalvo, A. Paoella, and S. Fathpour, "High-performance and linear thin-film lithium niobate Mach-Zehnder modulators on silicon up to 50 GHz," *Opt. Lett.*, vol. 41, no. 24, pp. 5700–5703, 2016.
- [25] A. Rao, M. Malinowski, A. Honardoost, J. R. Talukder, P. Rabiei, P. Delfyett, and S. Fathpour, "Second-harmonic generation in periodically-poled thin film lithium niobate wafer-bonded on silicon," *Opt. Express*, vol. 24, no. 26, pp. 29941–29947, 2016.
- [26] A. Rao, J. Chiles, S. Khan, S. Toroghi, M. Malinowski, G. F. Camacho Gonzalez, and S. Fathpour, "Second-harmonic generation in single-mode integrated waveguides based on mode-shape modulation," *Appl. Phys. Lett.*, vol. 110, Art. no. 111109, 2017.

- [27] A. Honardoost, G. F. Camacho Gonzalez, S. Khan, M. Malinowski, A. Rao, J. -E. Tremblay, A. Yadav, K. A. Richardson, M. C. Wu, and S. Fathpour, “Cascaded integration of optical waveguides with third-order nonlinearity with lithium niobate waveguides on silicon substrates,” *IEEE Photon. J.*, vol. 10, no. 3, Art. no. 4500909, 2018.
- [28] I. Krasnokutska, J. Tambasco, X. Li, and A. Peruzzo, “Ultra-low loss photonic circuits in lithium niobate on insulator,” *Opt. Express*, vol. 26, no. 2, pp. 897–904, 2018.
- [29] M. Zhang, C. Wang, R. Cheng, A. Shams-Ansari, and M. Loncar, “Monolithic ultra-high-Q lithium niobate microring resonator,” *Optica*, vol. 4, no. 12, pp. 1536–1537, 2018.
- [30] A. Rao, K. Abdelsalam, T. Sjaardema, G. F. Camacho Gonzalez, A. Honardoost, and S. Fathpour, “Highly efficient nonlinear integrated photonics in ultracompact periodically-poled lithium niobate on silicon,” *OSA Frontiers in Optics (FiO) Annual Meeting 2018, Washington, DC*, 2018.
- [31] L. Cao, A. Aboketaf, Z. Wang, and S. Preble, “Hybrid amorphous silicon (a-Si:H)-LiNbO₃ electro-optic modulator,” *Opt. Commun.*, vol. 330, pp. 40–44, 2014.
- [32] L. Chen, J. Chen, J. Nagy, and R. M. Reano, “Highly linear ring modulator from hybrid silicon and lithium niobate,” *Opt. Express*, vol. 23, no. 10, pp. 13255–13264, 2015.
- [33] A. J. Mercante, P. Yao, S. Shi, G. Schneider, J. Murakowski, and D. W. Prather, “110 GHz CMOS compatible thin film LiNbO₃ modulator on silicon,” *Opt. Express*, vol. 24, no. 14, pp. 15590–15595, 2016.
- [34] S. Jin, L. Xu, H. Zhang, and Y. Li, “LiNbO₃ thin-film modulators using silicon nitride surface ridge waveguides,” *IEEE Photon. Technol. Lett.*, vol. 28, no. 7, pp. 736–739, 2016.

- [35] L. Cai, Y. Kang, and H. Hu, “Electric-optical property of the proton exchanged phase modulator in single-crystal lithium niobate thin film,” *Opt. Express*, vol. 24, no. 5, pp. 4640–4647, 2016.
- [36] C. Wang, M. Zhang, B. Stern, M. Lipson, and M. Loncar, “Nanophotonic lithium niobate electro-optic modulators,” *Opt. Express*, vol. 26, no. 2, pp. 1547–1555, 2018.
- [37] P. O. Weigel, J. Zhao, K. Fang, H. Al-Rubaye, D. Trotter, D. Hood, J. Mudrick, C. Dallo, A. T. Pomerene, A. L. Starbuck, C. T. DeRose, A. L. Lentine, G. Rebeiz, and S. Mookherjea, “Hybrid silicon photonic-lithium niobate electro-optic Mach-Zehnder modulator beyond 100 GHz,” *arXiv:1803.10365*, 2018.
- [38] A.J. Mercante, S. Shi, P. Yao, L. Xie, R. M. Weikle, and D. W. Prather, “Thin film lithium niobate electro-optic modulator with terahertz operating bandwidth,” *Opt. Express*, vol. 26, no. 11, pp. 14810–14816, 2018.
- [39] C. Wang, M. Zhang, X. Chen, M. Bertrand, A. Shams-Ansari, S. Chandrasekhar, P. Winzer, and M. Loncar, “100-GHz low voltage integrated lithium niobate modulators,” *Conference on Lasers and Electro-Optics, (OSA CLEO)*, paper SM3B.4., 2018.
- [40] A. Rao, and S. Fathpour, “Compact lithium niobate electrooptic modulators,” *IEEE J. Sel. Top. Quantum Electron.*, vol. 24, no. 4, pp. 1–14, 2018.
- [41] K. Kubota, J. Noda, and O. Mikami, “Travelling wave optical modulator using a directional coupler LiNbO₃ waveguide,” *IEEE J. Quantum Electron.*, vol. 16, no. 7, pp. 754–760, 1980.
- [42] G. K. Gopalakrishnan and W. K. Burns, “Performance and modeling of resonantly enhanced LiNbO₃ modulators for low-loss analog fiber-optic links,” *IEEE Trans. Microwave Theory and Tech.*, vol. 42, no. 12, pp. 2650–2656, 1994.

- [43] H. Chung, W. S. C. Chang, and E. L. Adler, "Modeling and optimization of traveling-wave LiNbO₃ interferometric modulators," *IEEE J. Quantum Electron.*, vol. 27, no. 23, pp. 608–617, 1991.
- [44] J. M. Liu, *Photonic Devices*, Cambridge University Press, 2005.
- [45] D. M. Pozar, *Microwave Engineering*, Fourth Edition, Wiley, 2012.
- [46] R. Garg, I. Bahl, and M. Bozzi, *Microstrip Lines and Slotlines*, Third Edition, Artech House, 2013.
- [47] E. Chen, and S. Y. Chou, "Characteristics of coplanar transmission lines on multilayer substrates: modeling and experiments," *IEEE Trans. Microwave Theory and Tech.*, vol. 45, no. 6, pp. 939–945, 1997.
- [48] G. Chione, M. Goano, G. Madonna, G. Omegna, M. Pirola, S. Bosso, D. Frassati, and A. Perasso, "Microwave modeling and characterization of thick coplanar waveguides on oxide-coated lithium niobate substrates for electrooptical applications," *IEEE Trans. Microwave Theory and Tech.*, vol. 47, no. 12, pp. 2287–2293, 1999.
- [49] J. Baker-Jarvis, M. D. Janezic, B. Riddle, C. L. Holloway, and N. Paulter, "Dielectric and conductor-loss characterization and measurements on electronic packaging materials," *NIST*, Nist Tech. Note 1520, 2001.
- [50] C. Cochard, T. Spielmann, N. Bahlawane, A. Halpin, and T. Granzow, "Broadband characterization of congruent lithium niobate from mHz to optical frequencies," *J. Phys. D: Appl. Phys.*, vol. 50, no. 36, LT01, 2017.
- [51] W. B. Westphal, and A. Sils, "Dielectric constant and loss data," *Tech. Rep.*, AFML-TR-72-39, 1972.

- [52] G. Chione, "A CAD-oriented analytical model for the losses of general asymmetric coplanar lines in hybrid and monolithic MICs," *IEEE Trans. Microwave Theory and Tech.*, vol. 41, no. 9, pp. 1499–1510, 1993.

CHAPTER 4: TOWARDS SUBTERAHERTZ BANDWIDTH ULTRACOMPACT LITHIUM NIOBATE ELECTROOPTIC MODULATOR

The contents of this chapter have been published in: A. Honardoost, F. A. Juneghani, R. Safian, and S. Fathpour, "Towards subterahertz bandwidth ultracompact lithium niobate electrooptic modulator," Opt. Express 27(5), 6495–6501 (2019).

Abstract– Achieving ultrahigh-speed electrooptic modulators (subterahertz modulation bandwidths) is shown feasible in the thin-film lithium niobate integrated photonic platform. Design guidelines for optimization of the main radio-frequency and optical parameters are presented and 3-dB modulation bandwidth up to 400 GHz is proved attainable in 3-mm-long devices. Such unprecedented bandwidths pave the path towards utilizing the devices in advanced optical communication systems.

4.1 Introduction

High-performance optical modulation is an essential part of modern communication systems. Ultrahigh-speed modulators are of great interest for ever-increasing aggregate bandwidth requirements of optical communication systems. Due to increased complexity of the electronic and photonic systems, reduction in power consumption, manufacturing cost, device footprint, and overall packaged size are also demanded for analog and digital applications [1]–[3]. Among platform candidates, Mach-Zehnder (MZ) modulators, operating based on the linear electrooptic (EO) or Pockel's effect, have been demonstrated to be superior, boasting up to ~ 100 GHz modulation bandwidth (BW), as well as > 20 dB extinction ratios [4, 5]. Indeed, lithium niobate (LiNbO_3 , LN) has been the standard material for the EO modulators (EOM) used in long-haul optical networks, due to its large EO coefficient ($r_{33} = 31$ pm/V) and fabrication maturity [4]. However, conventional

LN waveguides (formed by in-diffusion of dopants or proton exchange processes) are bulky, i.e., their low index-contrast (< 0.1) yields weak optical confinement. As a result, high bending loss, long MZ electrode lengths, and low power efficiency due to large half-wave voltage-length product ($V_{\pi} \cdot L$), render the EOMs unattractive for large-scale integration demands of advanced optical networks [4, 5].

Thin-film approaches have been alternatively pursued to overcome these drawbacks of conventional LN devices and achieve ultracompact (submicron-scale) devices [6]. Particularly, exploiting heterogeneous integration techniques led to the emergence of ultracompact EOMs on silicon (Si) substrates [18]. This technology is potentially compatible with silicon photonics due to the choice of Si substrate. In order to attain lateral optical confinement and form submicron 2-D waveguides, one method is to rib-load the LN thin films with a refractive-index-matched material [18]–[17]. By utilizing the rib-loading method, difficulties of directly etching LN are avoided. However, it should be noted that, more recently, promising works have been reported on direct-etched LN thin films [10]–[12]. At any rate, high-speed thin-film LN EOMs with 3-dB BWs of 33 GHz and an extinction ratio of 18 dB have been reported on Si substrates [17]. Also recently, thin-film LN MZ EOMs with 3-dB BWs up to ~ 100 GHz have been demonstrated [13, 14].

With this stage of maturity, accurate design of the ultracompact EOMs and reliable prediction of their high-speed performance limits demanded an elaborate model. We have recently reported on such a general transmission-line model [15] and verified its accuracy by comparing the simulated results with prior experimental data [17].

In this work, novel designs are investigated in order to attain ultrahigh-BW (up to 400 GHz) MZ EOMs. Radio-frequency (RF) and optical parameters of the devices have been studied, and design guidelines and optimization procedures are presented for such unprecedented 3-dB modulation BWs for both rib-loaded and direct-etched thin-film LN EOMs. The present work paves the path towards exploiting the ultracompact devices in advanced integrated photonic circuits targeting futuristic optical communication applications, analog or digital, where subterahertz (sub-THz)

BWs are desired. It is finally noted that optically-assisted characterization of EOMs in the sub-THz range is feasible [16]. However, full realization of functioning analog or digital communication systems will require development of ultrahigh-speed electronic and photodetection components, which are obviously beyond the scope of this work.

4.2 Design optimization

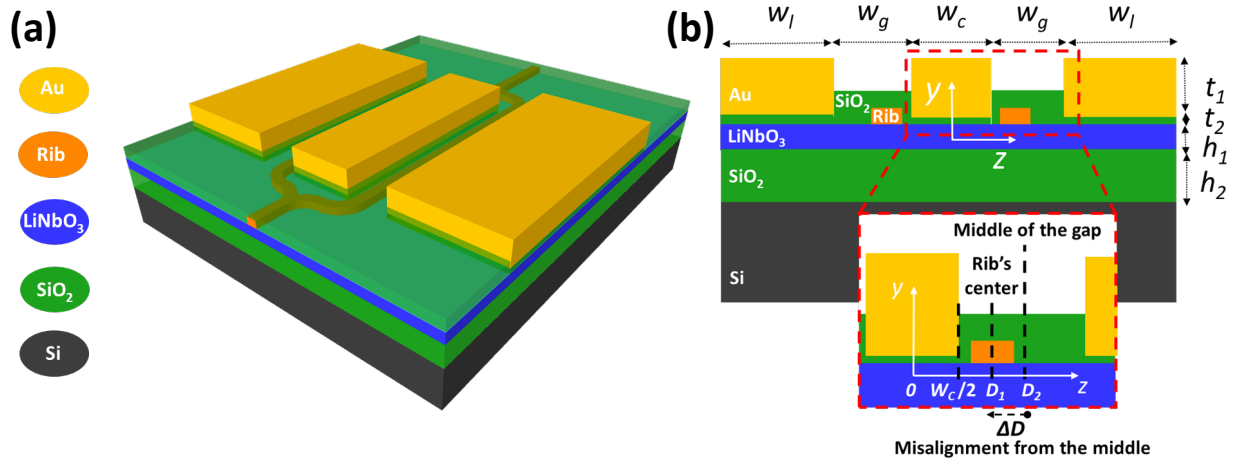


Figure 4.1: (a) 3-D schematic of the thin-film LN MZ EOMs; (b) Cross-section of the EOMs in the lateral y - z plane. The zoomed section shows the misalignment ($\Delta D = D_2 - D_1$) of the rib's center (D_1) from the middle of the gap between the electrodes (D_2).

The 3-D schematic of the thin-film LN MZ EOM in the push-pull configuration is depicted in Fig. 4.1(a). The slab region of the optical waveguide is an X - or Y -cut LN thin film bonded to a thick SiO₂ buffer layer on a Si substrate. The thin film can be prepared through ion-implantation, wafer bonding, and thermal slicing processes [6, 18]. The applied radio-frequency (RF) field, via the gold (Au) electrodes, is aligned along the Z -axis of the LN, in order to efficiently utilize the strongest EO coefficient of LN crystal (r_{33}). The thin-film LN is rib-loaded with a refractive-index-matched material, silicon nitride (SiN) for example [17], in order to provide lateral confinement for the optical mode. As mentioned, this method circumvents the need for direct etching of LN. However, it is important to note that the present work is not limited to rib-loaded waveguides.

Designs for both optical waveguide platforms, i.e., rib-loaded LN and direct-etched LN (all-LN), are investigated and the results, along with the discussion on pros and cons of each method, are presented at the end of Section 2.

By using ANSYS HFSS and COMSOLTM commercial simulators, the main parameters of the EOM are investigated in order to optimize the structure for ultrahigh BWs. The three main parameters are the RF loss, the effective index mismatch between the RF and optical guided modes ($\Delta n = |n_{RF} - n_{op}|$), and the characteristic impedance of the electrodes (Z_0). Simulation results suggest that the key parameters that play an important role in defining the RF properties of the device are the thickness of the electrodes (t_2), the gap between the electrodes (w_g), and the middle electrode's width (w_c). As evident in Figs. 4.2(a) and 4.2(b), by increasing t_2 , w_g , and w_c , RF loss decreases, and hence the final BW of the device is enhanced.

Another important parameter for BW enhancement is Δn . As n_{op} is constant within the concerned RF frequency (see Section 3 for example values), only the variations of n_{RF} versus t_2 , w_g , and w_c are presented in Figs. 4.2(c) and 4.2(d). Depending on the optical waveguide structure and its calculated invariant n_{op} , n_{RF} can be appropriately tuned in order to minimize Δn .

It is well-known that Z_0 should be kept as close as possible to the 50- Ω terminating resistive load in order to reduce the impedance mismatch. The results for variation of Z_0 , depicted in Figs. 4.2(e) and 4.2(f), suggest that this goal is achievable by varying the device dimensions for a specific RF frequency (e.g., 100 GHz in this case). However, as discussed later in Section 3, the frequency-dependence of Z_0 must be also considered in the overall design.

As the results in Fig. 4.2 imply, a larger w_g overall provides a more optimized design in terms of the RF loss. However, this increases $V_\pi \cdot L$, and consequently lowers the power efficiency of the EOM. Meanwhile, as is evident in Figs. 4.3(a) and 4.3(b), the magnitude of the applied RF field is much larger at the edges of the middle electrode. In order to compensate for the increase in $V_\pi \cdot L$, a solution is to place the optical waveguides closer to the middle electrode, instead of positioning them at the center of the gap between the electrodes, as is common practice.

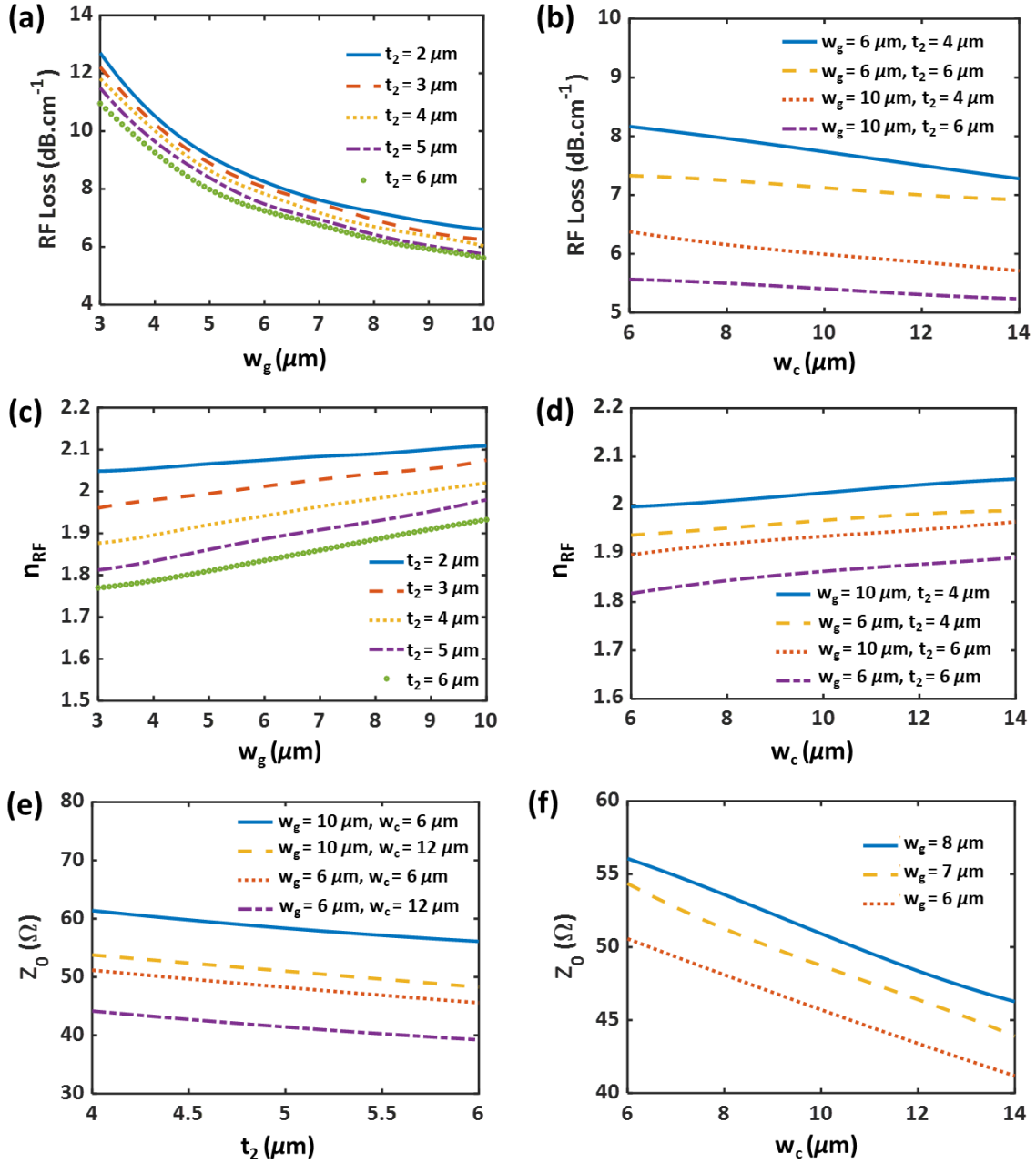


Figure 4.2: RF design considerations (all performed at 100 GHz for $w_l = 12.0 \mu\text{m}$ ($w_c = 8.0 \mu\text{m}$ for (a), (c), and (e))): Variation of (a) RF loss vs. w_g for different values of t_2 ; (b) RF loss vs. w_c for different values of w_g and t_2 ; (c) n_{RF} vs. w_g for different values of t_2 ; (d) n_{RF} vs. w_c for different values of w_g and t_2 ; (e) Z_0 vs. t_2 for different values of w_g and w_c ; and (f) Z_0 vs. w_c for different values of w_g .

This has been studied in bulk LN devices in the past [17, 18] and is applied to thin-film devices here. As depicted in Fig. 4.4 for both rib-loaded and all-LN structures, employing this asymmetric placement (see the inset of Fig. 4.1(b)) increases the overlap of the RF and optical field (Γ), while $V_\pi \cdot L$ decreases accordingly, for any chosen value of w_g . As an example, for fixed w_c and w_g (both equal to $8.0 \mu\text{m}$) and $D_1 = 6.0 \mu\text{m}$ in Fig. 4.1, corresponding to $\Delta D = D_2 - D_1 = +2 \mu\text{m}$ (instead of placing the waveguide in the center of the gap between the electrodes, giving $\Delta D = 0$), Γ increases by $\sim 17\%$ and $\sim 19\%$, for rib-loaded and all-LN devices, respectively.

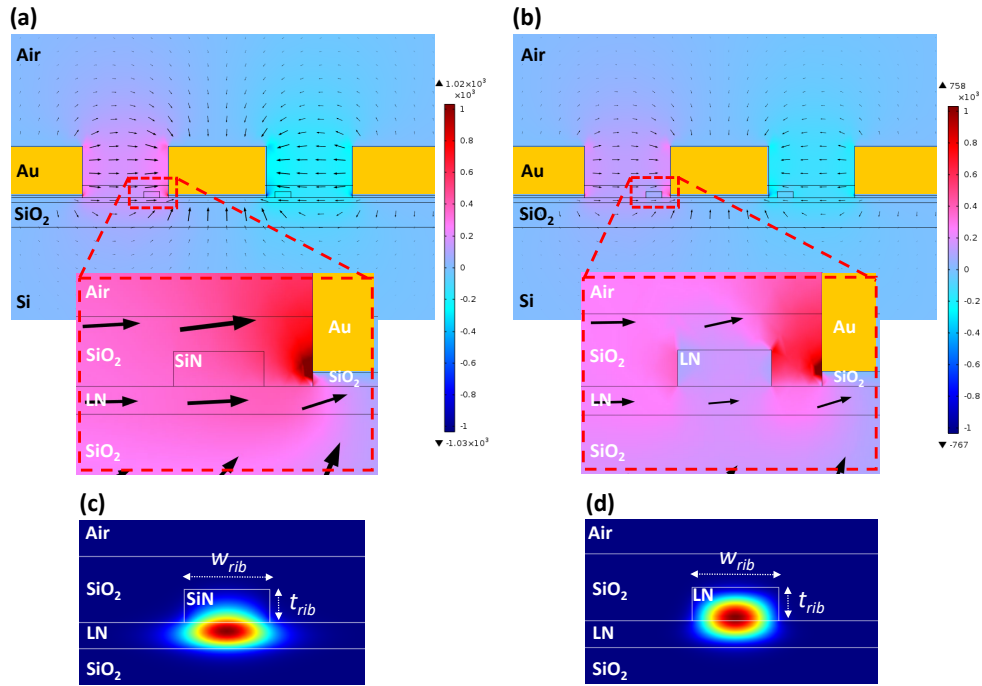


Figure 4.3: Simulated RF mode profile for (a) rib-loaded and (b) all-LN EOMs with identical dimensions. Arrows are proportional to the magnitude of the field. Identical plot settings have been employed for COMSOL™ plots in both cases. Simulated TE optical mode profile for (c) rib-loaded and (d) all-LN waveguides with the same $w_{rib} = 1.3 \mu\text{m}$, $t_{rib} = 0.5 \mu\text{m}$, and a $1\text{-}\mu\text{m}$ -thick top cladding SiO_2 layer.

However, by moving the optical waveguides closer to the middle electrode, the metal-induced optical loss can increase significantly. This issue can be addressed by adding a thin SiO_2 buffer layer between the electrodes and the LN thin film, as schematically shown in Figs. 4.1 and 4.3. This decreases the additional loss dramatically, making it negligible, as depicted in Fig. 4.5.

Specifically, for $w_g = 7.0 \mu\text{m}$ ($D_2 = 7.5 \mu\text{m}$), adding a 200-nm-thick buffer layer reduces the optical loss from ~ 100 to 0.1, and from ~ 1 to 0.001, all in dB/cm, for ΔD values of $+2.0 \mu\text{m}$ and $+0.5 \mu\text{m}$, respectively.

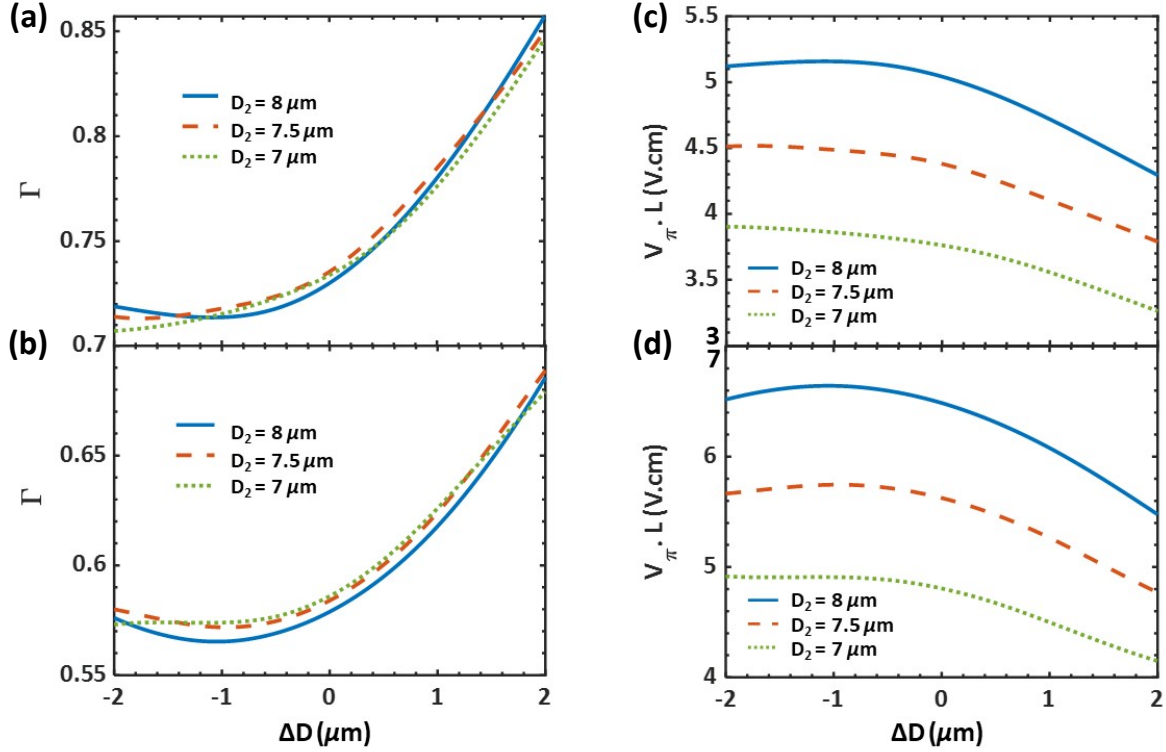


Figure 4.4: Γ for (a) rib-loaded; (b) all-LN EOMs; $V_{\pi} \cdot L$ for (c) rib-loaded; (d) all-LN EOMs, vs. ΔD (see Fig. 4.1(b)).

Here, the pros and cons of rib-loaded versus all-LN designs are discussed. As first reported in [15, 6], and reconfirmed here in Figs. 4.3(a) and 4.3(b), the magnitude of the RF field in the LN region is relatively larger in the rib-loaded case compared to the all-LN case, due to the lower dielectric constant of SiN (~ 4) compared to LN (~ 40). This can be simply explained through the electromagnetic boundary conditions, i.e., the continuity of the normal component of the electric displacement field leads to a higher electric field in the medium with the lower dielectric constant. To attain high Γ , this advantage of the rib-loaded case is partially counteracted by its lower optical confinement. The transverse-electric (TE) optical mode profiles for both waveguides are presented

in Figs. 4.3(c) and 4.3(d). Although $\sim 65\%$ of the optical mode is confined in the thin-film LN for the rib-loaded structure, the optical mode overlap with the LN region is higher ($\sim 95\%$) in the all-LN waveguide. This might allow for smaller gaps (w_g) between the electrodes in the all-LN EOM case compared to the rib-loaded counterpart, the issue of higher RF loss notwithstanding (see Fig. 4.2(a)). However, while the all-LN design can provide this stronger optical confinement and potential for smaller w_g , the aforementioned drop of the RF field in this case leads to a smaller Γ and a higher $V_\pi \cdot L$ compared to the rib-loaded device, for the same w_g and hence low RF loss. As an example, for $w_g = 7.0 \mu\text{m}$ ($D_2 = 7.5 \mu\text{m}$) and $\Delta D = +2.0 \mu\text{m}$, the rib-loaded design provides $\Gamma = 0.825$, which is 25% larger than that of all-LN design ($\Gamma = 0.65$), with corresponding $V_\pi \cdot L$ values of 3.7 and 4.9 V.cm, respectively.

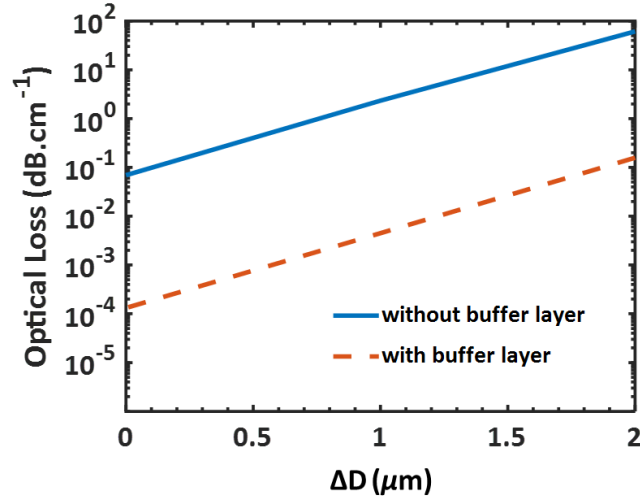


Figure 4.5: Metal-induced optical propagation loss vs. ΔD (see Fig. 4.1(b)) for $D_2 = 7.5 \mu\text{m}$.

4.3 Final results and discussions

Based on the design considerations in Section 2, the final optimized design for the dimensions shown in Fig. 4.1 are summarized in Table 1. The optical waveguide dimensions w_{rib} and t_{rib} (defined in Fig. 4.3) are 1.3 and 0.5 μm for the rib-loaded, and 1.0 and 0.4 μm for the all-LN EOM, respectively. Different dimensions are chosen for the optical waveguide of each structure in

order to minimize Δn and maximize Γ for both cases. The former helps to achieve the maximum possible final BW, while the latter improves the power efficiency of the device by reducing $V_\pi \cdot L$.

Variations of different device metrics versus RF frequency are presented in Fig. 4.6. It is evident that n_{RF} drops sharply in the sub-GHz region, but remains fairly close to n_{op} , i.e., 1.91 and 1.96 for the rib-loaded and all-LN EOM, respectively, up to sub-THz frequencies, thus Δn remains small. As shown in Fig. 4.6(b), the RF loss of the optimized design is kept < 18 dB/cm up to 400 GHz, while Z_0 is kept close to 50Ω for most of the frequency range.

Table 4.1: Values of the geometrical dimensions in Fig. 1(b) for the optimized EOMs.

Parameter	w_l	w_g	ΔD	w_c	t_1	t_2	h_1	h_2
Value (μm)	12.0	7.0	2.0	8.0	0.2	4.0	0.4	2.0

Finally, by exploiting Eqn. (20) in [15], for the optimized design parameters presented in Table 1, the EO frequency responses of the rib-loaded as well as all-LN EOMs are summarized in Fig. 4.6(c) for three different electrode lengths, L . It is clear that shorter electrode lengths provide a larger 3-dB BW at the expense of increased V_π . The results predict that if sub-THz applications are desired and high voltages can be afforded (see Figs. 4.4(c) and (d)), an impressively high 3-dB BW of 395 and 368 GHz with corresponding V_π values of 12.3 V and 16.3 V can be attained for the rib-loaded and all-LN EOM cases, respectively, both with $L = 3$ mm. For $L = 5$ mm, a BW of ~ 250 GHz is exhibited which is 2.5 times larger than what is reported in [13, 14] for the same length and with comparable $V_\pi \cdot L$. A comparison between rib-loaded and all-LN design for a fixed drive voltage is given in Table 2.

The higher BW in the rib-loaded design is worthy of discussion. The comparison between Δn of the rib-loaded versus all-LN EOM is depicted in the inset of Fig. 4.6(a). As the frequency is increased, the RF field concentration shifts more towards lower index materials (SiO_2 and air), and therefore the effective permittivity of the field decreases. As the figure implies, n_{RF} is virtually identical in both cases, while they possess different n_{op} values. Up to ~ 250 GHz, marked with an "A," n_{RF} remains close to the value of n_{op} in the all-LN design, and thus provides a slightly larger

3-dB BW compared to the rib-loaded counterpart. However, n_{RF} drops from ~ 1.95 at 250 GHz to ~ 1.83 at 400 GHz. Hence, in this region, Δn is smaller for the rib-loaded EOM which results in a larger BW.

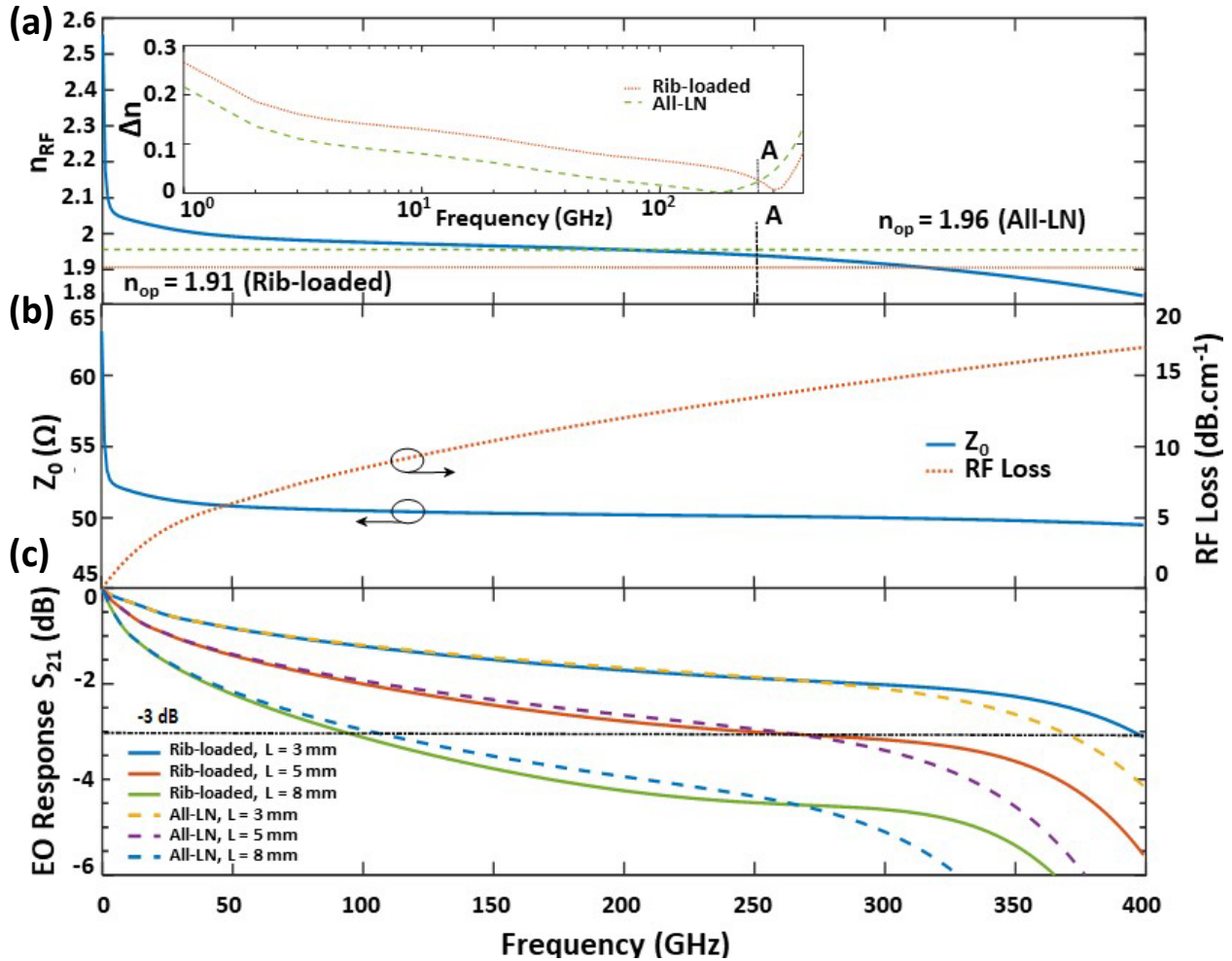


Figure 4.6: (a) n_{RF} ; (b) Z_0 and RF loss; (c) EO response (S_{21}) of the EOMs for different lengths. The horizontal dashed line shows the 3-dB electrical BW, and the inset depicts Δn .

In principle, choosing another rib-loading material with a different optical index and optimizing the RF and optical properties of the corresponding structure could lead to even higher BWs for the same L . In other words, the ~ 400 GHz given here for $L = 3$ mm is not necessarily the ultimate BW attainable in thin-film LN EOMs.

Table 4.2: Comparison between rib-loaded and all-LN design for a fixed drive voltage.

Drive Voltage (V)	L (cm)		BW (GHz)	
	Rib-loaded	All-LN	Rib-loaded	All-LN
1	3.7	4.9	5	3
5	0.74	0.98	110	66
10	0.37	0.49	362	256
15	0.24	0.32	420	340

4.4 Conclusion

We report on a novel design for ultracompact thin-film LN EOMs on Si substrates capable of operating up to ~ 400 GHz 3-dB modulation bandwidths for 3-mm-long MZ arms. Detailed design guidelines and optimization procedures for such an impressive performance are presented for future subterahertz optical communication system applications.

4.5 References

- [1] J. Yao, “Microwave photonics,” *IEEE J. Light. Technol.* **27**(3), 314–335 (2009).
- [2] J. Capmany, and D. Novak, “Microwave photonics combines two worlds,” *Nat. Photon.* **1**, 319–330 (2007).
- [3] J. Yu, X. Li, and W. Zhou, “Tutorial: Broadband fiber-wireless integration for 5G+ communication,” *APL Phot.* **3**(11), 111101 (2018).
- [4] E. L. Wooten, K. M. Kissa, A. Yi-Yan, E. J. Murphy, D. A. Lafaw, P. F. Hallemeier, D. Maack, D. V. Attanasio, D. J. Fritz, G. J. McBrien, and D. E. Bossi, “A review of lithium niobate modulators for fiber-optic communications systems,” *IEEE J. Quant. Elec.*, **6**(1), 69–82 (2000).
- [5] K. Noguchi, O. Mitomi, and H. Miyazawa, “Millimeter-wave Ti:LiNbO₃ optical modulators,” *IEEE J. Light. Technol.*, **16**(4), 615–619 (1998).

- [6] A. Rao, and S. Fathpour, “Compact lithium niobate electrooptic modulators,” *IEEE J. Sel. Top. Quantum Electron.*, **24**(4), 1–14 (2018).
- [7] P. Rabiei, J. Ma, S. Khan, J. Chiles, and S. Fathpour, “Heterogeneous lithium niobate photonics on silicon substrates,” *Opt. Express*, **21**(21), 25573–25581 (2013).
- [8] A. Rao, A. Patil, J. Chiles, M. Malinowski, S. Novak, K. Richardson, P. Rabiei, and S. Fathpour, “Heterogeneous microring and Mach-Zehnder modulators based on lithium niobate and chalcogenide glasses on silicon,” *Opt. Express*, **23**(17), 22746–22752 (2015).
- [9] A. Rao, A. Patil, P. Rabiei, A. Honardoost, R. DeSalvo, A. Paoella, and S. Fathpour, “High-performance and linear thin-film lithium niobate Mach-Zehnder modulators on silicon up to 50 GHz,” *Opt. Lett.*, **41**(24), 5700–5703 (2016).
- [10] I. Krasnokutska, J. Tambasco, X. Li, and A. Peruzzo, “Ultra-low loss photonic circuits in lithium niobate on insulator,” *Opt. Express*, **26**(2), 897–904 (2018).
- [11] M. Zhang, C. Wang, R. Cheng, A. Shams-Ansari, and M. Loncar, “Monolithic ultra-high-Q lithium niobate microring resonator,” *Optica*, **4**(12), 1536–1537 (2018).
- [12] A. Rao, K. Abdelsalam, T. Sjaardema, G. F. Camacho Gonzalez, A. Honardoost, and S. Fathpour, “Highly efficient nonlinear integrated photonics in ultracompact periodically-poled lithium niobate on silicon,” in *Proc. OSA Frontiers Opt. Annu. Meeting*, Washington, DC, USA, 2018, Paper JTU3A.59.
- [13] P. O. Weigel, J. Zhao, K. Fang, H. Al-Rubaye, D. Trotter, D. Hood, J. Mudrick, C. Dallo, A. T. Pomerene, A. L. Starbuck, C. T. DeRose, A. L. Lentine, G. Rebeiz, and S. Mookherjea, “Bonded thin film lithium niobate modulator on a silicon photonics platform exceeding 100 GHz 3-dB electrical modulation bandwidth,” *Opt. Express*, **26**(18), 23728–23739 (2018).

- [14] C. Wang, M. Zhang, X. Chen, M. Bertrand, A. Shams-Ansari, S. Chandrasekhar, P. Winzer, and M. Loncar, “Integrated lithium niobate electro-optic modulators operating at CMOS-compatible voltages,” *Nature*, **562**, 101–104 (2018).
- [15] A. Honardoost, R. Safian, A. Rao, and S. Fathpour, “High-speed modeling of ultracompact electrooptic modulators,” *IEEE J. Light. Technol.* **36**(24), 5893–5902 (2018).
- [16] A. J. Mercante, S. Shi, P. Yao, L. Xie, R. M. Weikle, and D. W. Prather, “Thin film lithium niobate electro-optic modulator with terahertz operating bandwidth,” *Opt. Express*, **26**(11), 14810–14816 (2018).
- [17] R. A. Becker, and B. E. Kincaid, “Improved electrooptic efficiency in guided-wave modulators,” *IEEE J. Light. Technol.* **11**(12), 2076–2079 (1993).
- [18] S. -J. Chang, C. -L. Tsi, Y. -B. Lin, J. -F. Liu, and W. -S. Wang “Improved electrooptic modulator with ridge structure in X-cut LiNbO₃,” *IEEE J. Light. Technol.* **17**(5), 843–847 (1999).

CHAPTER 5: CASCADED INTEGRATION OF OPTICAL WAVEGUIDES WITH THIRD-ORDER NONLINEARITY WITH LITHIUM NIOBATE WAVEGUIDES ON SILICON SUBSTRATES

The contents of this chapter have been published in: A. Honardoost, G. F. Camacho Gonzalez, S. Khan, M. Malinowski, A. Rao, J. -E. Tremblay, A. Yadav, K. A. Richardson, M. C. Wu, and S. Fathpour, “Cascaded integration of optical waveguides with third-order nonlinearity with lithium niobate waveguides on silicon substrates,” IEEE Photon. J., vol. 10, no. 3, Art. no. 4500909, 2018.

Abstract– The cascaded integration of optical waveguides with third-order optical nonlinearity ($\chi^{(3)}$ susceptibility) with lithium niobate (LiNbO_3) waveguides is demonstrated on the same chip. Thin-film (LiNbO_3) and chalcogenide (ChG) glass ($\text{Ge}_{23}\text{Sb}_7\text{S}_{70}$) waveguides are integrated on silicon (Si) substrates. An optical mode transition between the two waveguides is achieved through low-loss mode-converting tapers, with a measured loss of ~ 1.5 dB for transverse-electric (TE) and ~ 1.75 dB for transverse-magnetic (TM) input polarizations. For nonlinear characterization, wavelength conversion via four-wave mixing (FWM) is demonstrated on the ChG-LN waveguides. This platform provides an efficient method for the utilization of second- and third-order optical nonlinearities on the same chip, rendering it ideal for nonlinear applications such as stabilized octave-spanning optical frequency comb generation.

5.1 Introduction

There has been a dramatic increase of interest in Silicon (Si) photonics since the late 1980s [1]–[3]. Silicon photonics has been widely pursued as a promising technology for a variety of applications such as in datacom transceivers [2]. However, several shortcomings are well-known for Si, when it comes to nonlinear optical applications. For example, Si inherently lacks second-order optical sus-

ceptibility ($\chi^{(2)}$) due to its centrosymmetric lattice structure. This restricts convenient utilization of standard silicon photonics for applications such as second-harmonic generation (SHG). Also, the presences of two-photon and free-carrier absorptions (TPA and FCA), at the required high optical intensities, limit the exploitation of silicon's large third-order optical susceptibility ($\chi^{(3)}$), at least at telecom wavelengths [2], [4].

Several approaches have been pursued in order to circumvent silicon photonics lack of $\chi^{(2)}$ -based optical nonlinearity. Heterogeneous integration of other materials on Si with second-order nonlinearity, e.g., lithium niobate (LN) [5], [6], and aluminum nitride (AlN) [7], [8] is one approach. Electric field-induced $\chi^{(2)}$ nonlinearity [9], as well as waveguides stressed under silicon nitride (Si_3N_4 or SiN) [10] are other approaches. A detailed review of all these approaches has been recently published [11]. Similarly, heterogeneous integration of materials with high $\chi^{(3)}$ and insignificant TPA have been pursued to avoid silicon's shortcoming for third-order nonlinear integrated optics. Si_3N_4 , chalcogenide (ChG) glass, hydrogenated amorphous Si (a-Si:H), and HydexTM are some of the major non-organic example materials [4]. Organic materials and hybrid silicon-organic structures have been long pursued as well [12]–[14].

Evidently, there has been several works on integration of other nonlinear materials on silicon. However, the efforts have been primarily limited to integrating a "single" material. Naturally, the new frontline of research should target monolithic integration of "multiple" materials/devices for more advanced functionalities on the same chip. For example, it is very important to "co-integrate" cascaded waveguides with $\chi^{(2)}$ and $\chi^{(3)}$ properties in the context of frequency-stabilized optical comb generation. The $\chi^{(3)}$ waveguide provides octave-spanning supercontinuum generation (SCG), while second-harmonic generation in the $\chi^{(2)}$ device is used for stabilization by f -to- $2f$ carrier-envelope offset (CEO) locking [15], [16]. The present work is the first effort in paving the path towards integration of two example materials, namely ChG ($\chi^{(3)}$) and lithium niobate (LiNbO_3 , LN) ($\chi^{(2)}$) waveguides, towards this goal.

LN is one of the most widely used materials for nonlinear optical applications. Trans-

parency in a broad range of the electromagnetic spectrum (0.4-5 μm), strong second-order nonlinearity, as well as a large electrooptic coefficient [4] make LN an ideal material for integration with Si photonics for applications such as SHG [5], [6], and optical modulation [17], [18]. Potential future demonstrations on silicon may include generation of entangled photon pairs for quantum-optic applications [19], [20]. However, conventional LN devices (fabricated using dopant diffusion [21], or proton-exchange processes [22]) are bulky in general and exhibit low efficiency in terms of power consumption and device footprint, hence hampering the desired large-scale integration capability. Compact LN waveguides, based on bonding of thin films of LN on oxidized Si substrates, have been demonstrated and pursued towards satisfying the requirement of large-scale integration [18]. Moreover, by loading the LN thin films with a rib waveguide made out of a refractive-index-matched material (such as tantalum pentoxide (Ta_2O_5) [18], ChG [23], or Si_3N_4 [17]), high optical confinement and low loss has been achieved. Consequently, these submicron rib-loaded (hybrid) waveguides have rendered themselves useful for compact $\chi^{(2)}$ -based nonlinear-optic applications [5], [6], as well as high-performance electrooptic modulation [17], [18], [23]. Coincidentally and as mentioned above, Si_3N_4 and ChG are also among commonly employed materials fabricated on oxidized Si for their strong $\chi^{(3)}$ -based nonlinearities [4]. Recently, the heterogeneous integration of Si_3N_4 waveguides with thin-film LN on Si has been demonstrated, but no nonlinear measurement was reported [24]. Moreover, nonlinear refractive index of ChG ($3.71 \times 10^{-18} \text{ m}^2/\text{W}$) [25] is almost 15 times larger than that of Si_3N_4 ($0.24 \times 10^{-18} \text{ m}^2/\text{W}$) [26]. These properties combined with the possibility of obtaining high optical confinement and low-loss waveguides make ChG an attractive candidate for various nonlinear applications [25], [27]–[30].

This work reports on cascaded integration of ChG glass and thin-film LN waveguides on the same Si chip. Carefully designed mode-converting tapers are employed for adiabatic optical mode transition from ChG to hybrid LN waveguides and vice versa. In comparison to the previous report on integration of Si_3N_4 waveguides with thin-film LN [24], our proposed platform has the advantages of eliminating the need for LN bonding at the final stages of the processing, and offers

a simpler fabrication process. Also, as proof of concept, we provide four-wave mixing (FWM) results on the ChG portion of the ChG-LN integrated devices.

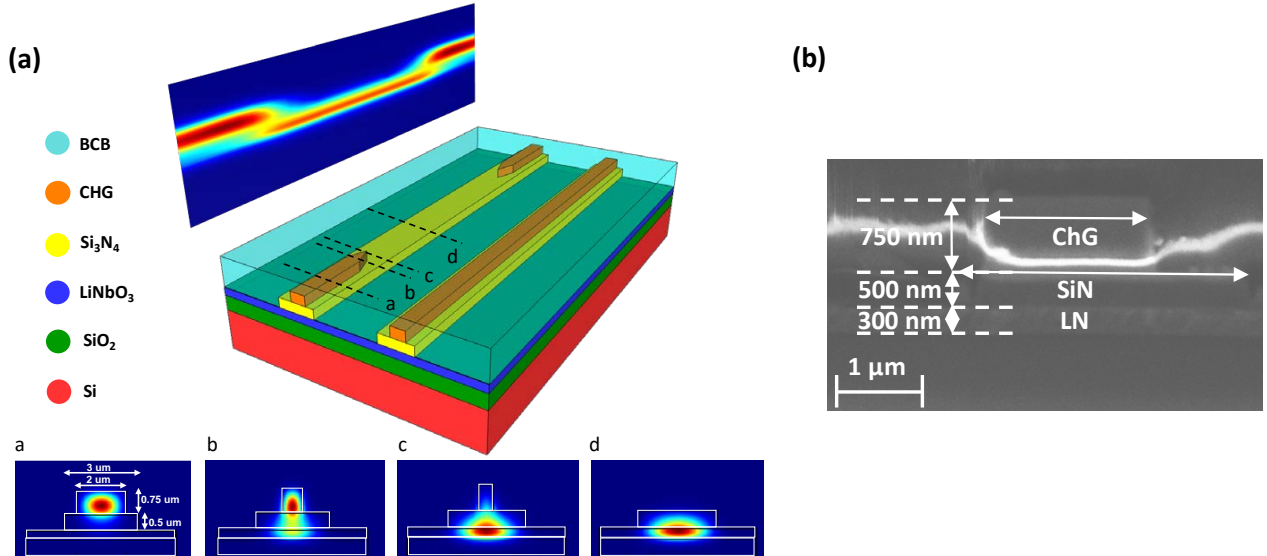


Figure 5.1: (a) Schematic of the integrated ChG-LN as well as the reference waveguides. Simulated optical mode profiles of the structure are also shown for fundamental TE input at 1550 nm for different cross-sections. Adiabatic mode transition is shown in the inset. (b) A cross-section SEM image of the fabricated devices at position b of the taper.

5.2 Design and Simulation

The schematic of the integrated platform is shown in Fig. 5.1(a). The optical mode profiles of the structure are simulated by using LumericalTM Mode Solutions. The fundamental transverse-electric (TE) mode at 1550 nm is shown at different cross-sections of the structure. The input mode is mainly distributed in the ChG rib, due to its higher refractive index compared to Si_3N_4 's. By introducing the tapered region, the optical mode gradually transfers into the Si_3N_4 -LN lower waveguide, where $\sim 50\%$ of the mode distribution is confined within the LN thin film. The top-left inset depicts the adiabatic TE-mode transition from the upper waveguide region (ChG) to the lower

one (Si_3N_4 -LN) by the 500- μm length of the taper and vice versa. Adiabatic mode transition for negligible TE-mode coupling loss is found to be occurring at taper lengths of $> 100 \mu\text{m}$, according to the LumericalTM simulations depicted in Fig. 5.2(a). Meanwhile, similar simulations show that the coupling efficiency for the transverse-magnetic (TM) input mode is $\sim 90\%$. This lower coupling efficiency is due to the fact that the TM mode is less confined than the TE mode. This behavioral difference between TE and TM modes in tapers has been observed in other waveguide platforms [31].

It should be stressed that the Si_3N_4 waveguide, between the ChG waveguide and the LN slab, plays an important role. By inserting the lower-index Si_3N_4 layer, $\chi^{(3)}$ and $\chi^{(2)}$ (i.e., ChG and LN) are uncoupled in the untapered regions. In other words, the Si_3N_4 buffer ensures that the LN slab does not interfere with the mode in the ChG waveguide, which is engineered to achieve the desired dispersion.

It is also noted that the present cascaded integration of ChG and/or Si_3N_4 and LN waveguides should not be confused with the aforementioned rib-loading of LN with similar materials for hybrid waveguide formation [5], [6], [17], [18], [23]. In those works, ChG, Si_3N_4 or any other index-matched material is solely used as a rib-loading layer on top of LN thin films for lateral optical confinement in order to avoid the difficulties of etching LN. That is, exploiting the $\chi^{(3)}$ nonlinearity of the rib-loading material is not intended in those works.

Figure 5.2(b) shows the simulated coupling efficiency of the tapers versus wavelength, suggesting a large bandwidth for the proposed structure. In addition to the large optical bandwidth, high error tolerance is also predicted by the simulation results. Figure 5.2(c) depicts the coupling efficiency of the taper versus the width of its tip. Coupling efficiency is also shown versus the misalignment between the centers of the ChG waveguide/taper and the underneath Si_3N_4 -LN waveguide in Fig. 5.2(d).

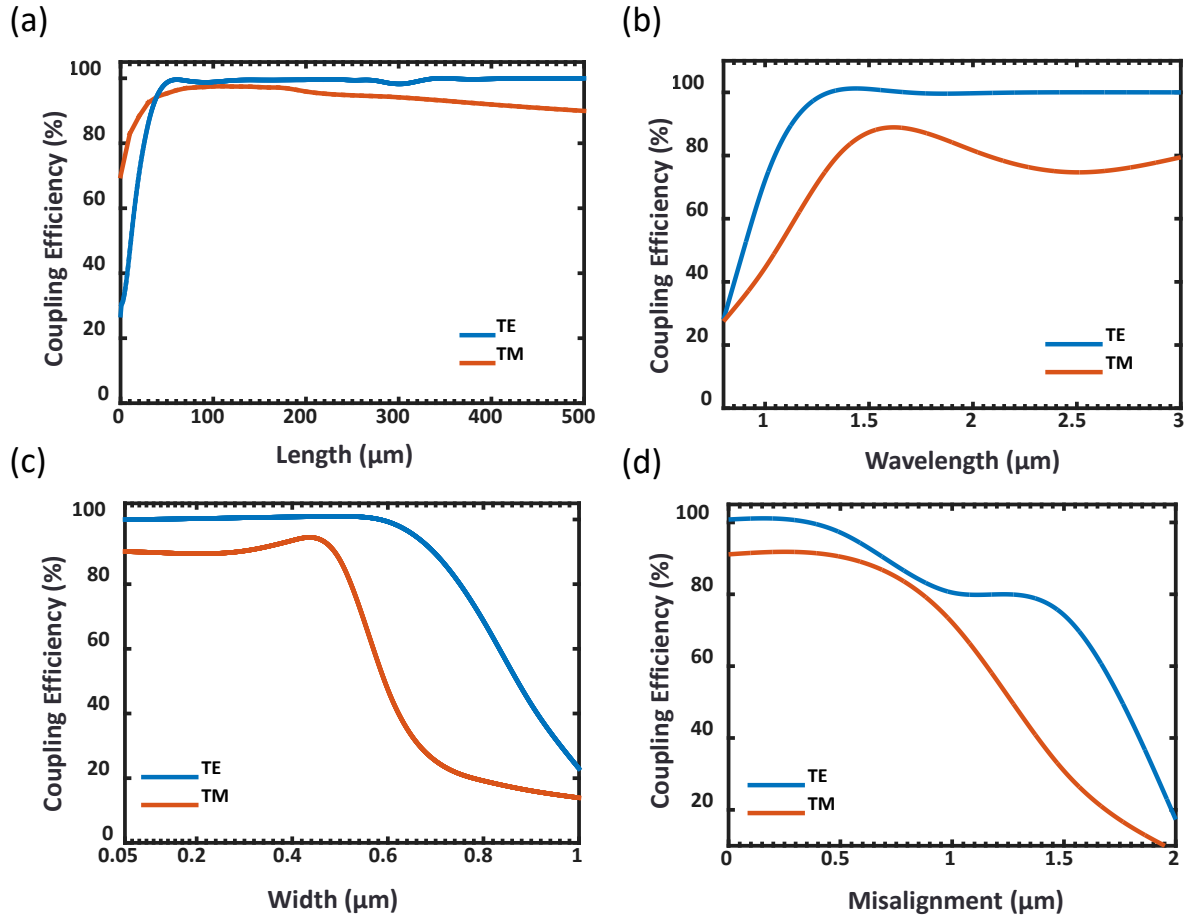


Figure 5.2: Simulated coupling efficiency of the mode-converting tapers vs. (a) Length of the taper; (b) Wavelength; (c) Width of the taper’s tip; and (d) Misalignment between the centers of the ChG waveguide/taper and Si_3N_4 -LN waveguide.

5.3 Fabrication

The fabrication process begins with a 300-nm-thick *X*-cut LN thin film wafers from NanoLN. A 500-nm-thick layer of Si_3N_4 was deposited on the LN thin films, using plasma-enhanced chemical vapor deposition (PECVD). The deposition was performed at 750 mTorr pressure and 300°C temperature, with a gas mixture of 2% silane and nitrogen, flowing at 2000 and 10 sccm, respectively. The 3- μm -wide ribs were patterned using electron-beam lithography (EBL), followed by dry etching using inductively-coupled plasma reactive-ion etching (ICP-RIE). The process parameters of

20 and 5 sccm for flows of CHF_3 and Ar, respectively, biasing power of 70 W, ICP power of 300 W and pressure of 7 mTorr were used. Then, a 750-nm-thick layer of ChG glass, $\text{Ge}_{23}\text{Sb}_7\text{S}_{70}$, was deposited using a thermal evaporator. The ChG glass was patterned and etched to form the waveguides along with the mode-converting tapers, on top of the Si_3N_4 rib waveguides. Same gases and flow rates were used as in the Si_3N_4 etch, but at a lower pressure of 5 mTorr. The biasing and ICP powers were 300 and 100 W, respectively.

The particular glass composition of $\text{Ge}_{23}\text{Sb}_7\text{S}_{70}$ has been used in our previous works and optimized for low-loss waveguides and the required refractive index [28], [29]. The film refractive indices at 1550 nm wavelength were measured to be 2.21, 1.93, and 2.24 for LN, Si_3N_4 and ChG respectively, using the prism-coupling method. The lengths of the two ChG straight sections, shown in Fig. 5.1(a), are 4.0 mm, each, and the corresponding lengths of the tapered regions are 0.5 mm, each, with a 1-mm Si_3N_4 gap in between. 10-mm-long reference waveguides without tapers were also fabricated on the same chip (as shown in Fig. 5.1(a)) which are used to isolate the mode transition losses, induced by the tapers. Finally, a 2- μm -thick layer of benzocyclobutene (BCB) was spun and cured on top to serve as a passivation layer, as well as the top cladding for the devices. Figure 5.1(b) shows a scanning-electron microscopy (SEM) image of the cross-section of a fabricated waveguide with labeled material regions. The lateral asymmetry of the ChG and Si_3N_4 waveguides is due to lithography misalignment. The measured LN, Si_3N_4 and ChG layer thicknesses are in agreement with the targeted values reported in the fabrication steps.

5.4 Characterization

5.4.1 Linear Characterization

The devices are characterized by using a tunable single-mode continuous-wave (CW) laser source. The TE output from a polarization controller is end-butt coupled into the waveguides through a lensed fiber. Another lensed fiber couples the light out of the waveguides into a photodetector in

order to measure the output optical power and hence the insertion loss. Both the ChG-Si₃N₄-LN integrated devices as well as the reference waveguides (with no tapers) are characterized. The measurements are also done for the TM input polarization. The results are presented in Fig. 5.3(a) over the wavelength range of 1550-1560 nm for 10 dBm input power. The evident ~ 22 dB insertion is mostly attributed to not incorporating optical mode-converters at the chips' input and output facets.

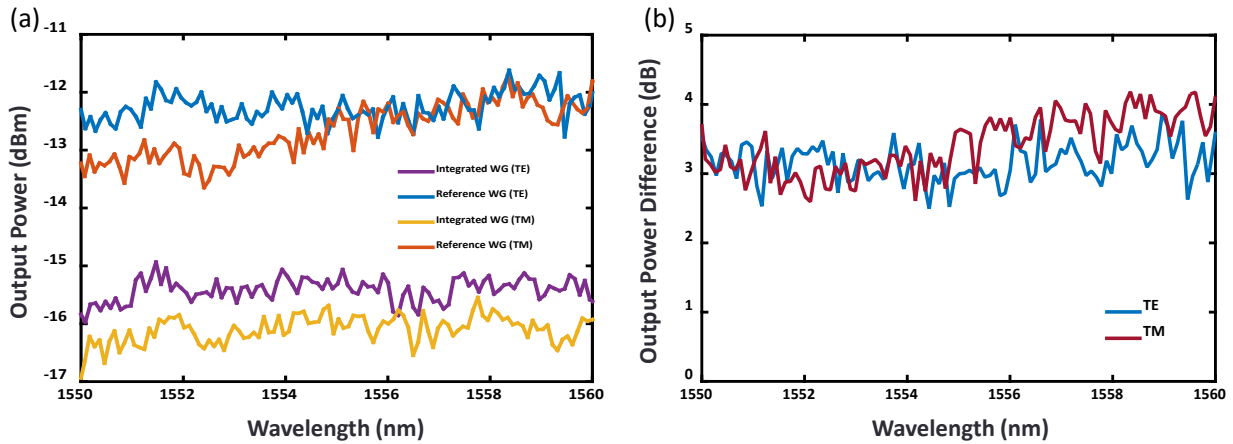


Figure 5.3: (a) Optical spectra of output power (10 dBm input power) for the integrated as well as the reference waveguides for both TE and TM input polarizations in the 1550-1560 nm wavelength range; (b) Output power difference between the integrated and reference waveguides for TE and TM input polarizations for the same wavelength range.

Figure 5.3(b) shows the output power difference between the integrated and reference waveguides for TE and TM polarizations in the same wavelength range. The results confirm that for TE polarization, there is only ~ 3 dB power difference between the integrated and reference waveguides, i.e., ~ 1.5 dB loss per mode-converting tapers. Similar coupling loss values have been reported in the past [32]. The measurements for the TM input polarization (when numerically averaged over the 10-nm wavelength range) result in an average of ~ 0.5 dB higher loss compared to the TE measurement. This result is qualitatively consistent with the simulated lower coupling efficiency of $\sim 90\%$ for the TM mode.

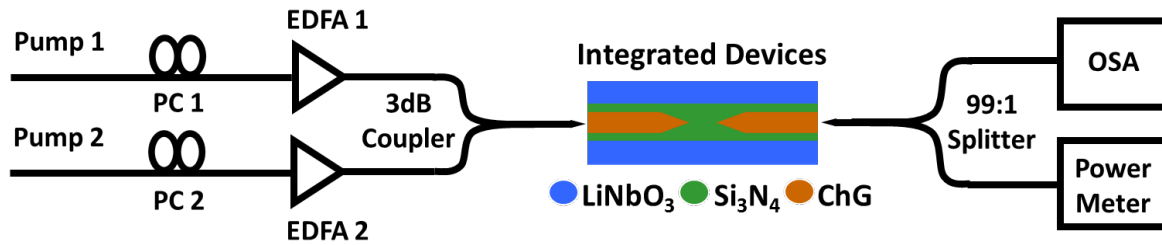


Figure 5.4: Schematic of the experimental setup for wavelength conversion via FWM. PC: Polarization Controller, EDFA: Erbium-doped fiber amplifier, OSA: Optical spectrum analyzer.

5.4.2 Nonlinear Characterization

For nonlinear characterization, wavelength conversion via FWM is measured for the integrated waveguides of the chip. The setup for this experiment is depicted in Fig. 5.4. Two tunable single-mode CW laser sources (Pumps 1 and 2 with spectral ranges of 1490-1630 nm and 1515-1565 nm, respectively) are used for the input. Two polarization controllers are connected at the output of the laser sources in order to make the polarizations collinear. Both laser signals are amplified using erbium-doped fiber amplifiers (EDFAs) and then combined in a 3-dB coupler. End-but coupling with lensed fibers is used to couple the combined signals into and out of the waveguides. The output signal is then followed by a 99:1 splitter, where one percent goes to the power meter for monitoring the alignment and ninety-nine percent is received by an optical spectrum analyzer (OSA).

Both input lasers are used as pumps and idlers simultaneously, generating two FWM converted signals with higher intensity. This nonlinear experiment was performed in the integrated ChG-LN waveguides to confirm both the light coupling into ChG and the capability of the chip to generate third-order nonlinearities. The result of the experiment is shown in Fig. 5.5. The two higher peaks correspond to the amplified tunable lasers at 1562.29 ± 0.01 and 1562.56 ± 0.01 nm. The observed signals at the sides correspond to FWM generation at 1562.01 ± 0.01 and 1562.84 ± 0.01 nm. Although the nonlinearity in the Si₃N₄ gap may have contributed to the FWM signal,

but since the length of the gap is only 1 mm, compared to 9 mm of ChG, it is expected that Si_3N_4 's contribution is small, as verified by the following simulation.

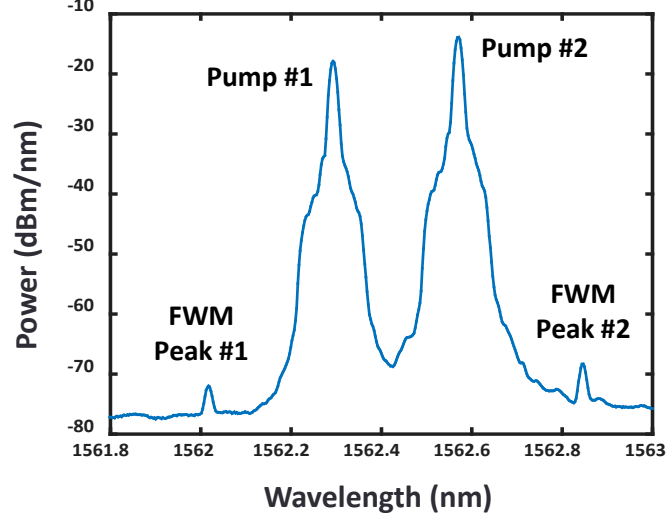


Figure 5.5: Measured output spectrum from the integrated ChG-LN waveguides from the OSA at a resolution of 0.02 nm.

Numerical study of the FWM results was performed by solving the nonlinear coupled equations [33]:

$$\frac{dA_1}{dz} = -\frac{\alpha}{2}A_1 + i\gamma(|A_1|^2 + 2\sum_{i \neq 1}^4 |A_i|^2)A_1 + i2\gamma A_2 A_3 A_4^* e^{i\Delta k_1 z} + i\gamma(A_2)^2 A_3^* e^{i\Delta k_2 z}, \quad (\text{A.1})$$

$$\begin{aligned} \frac{dA_2}{dz} = & -\frac{\alpha}{2}A_2 + i\gamma(|A_2|^2 + 2\sum_{i \neq 2}^4 |A_i|^2)A_2 + i2\gamma[A_1 A_4 A_3^* e^{-i\Delta k_1 z} + A_1 A_3 A_2^* e^{-i\Delta k_2 z}] \\ & + i\gamma(A_3)^2 A_4^* e^{i\Delta k_3 z}, \end{aligned} \quad (\text{A.2})$$

$$\begin{aligned} \frac{dA_3}{dz} = & -\frac{\alpha}{2}A_3 + i\gamma(|A_3|^2 + 2 \sum_{i \neq 3}^4 |A_i|^2)A_3 + i2\gamma[A_1A_4A_2^*e^{-i\Delta k_1 z} + A_2A_4A_3^*e^{-i\Delta k_3 z}] \\ & + i\gamma(A_2)^2A_1^*e^{i\Delta k_2 z}, \end{aligned} \quad (\text{A.3})$$

$$\frac{dA_4}{dz} = -\frac{\alpha}{2}A_4 + i\gamma(|A_4|^2 + 2 \sum_{i \neq 4}^4 |A_i|^2)A_4 + i2\gamma A_2A_3A_1^*e^{i\Delta k_1 z} + i\gamma(A_3)^2A_2^*e^{i\Delta k_3 z}, \quad (\text{A.4})$$

where A_1 , A_2 , A_3 , and A_4 are the field amplitudes corresponding to FWM#1, Pump#1, Pump#2 and FWM#2 in Fig. 5, respectively. α is the linear propagation loss and $\gamma = n_2\omega/cA_{eff}$ is the nonlinear parameter. These equations are obtained by solving $P^{(3)} = \frac{1}{2}\chi^{(3)}\epsilon_0 EE^*E + c. c.$ for $E = \sum_{n=1}^4 A_n e^{i(\omega t - k_n z)}$, and considering three phase matching conditions:

$$\Delta k_1 = k_2 + k_3 - k_1 - k_4, \quad (\text{A.5})$$

$$\Delta k_2 = 2k_2 - k_1 - k_3, \quad (\text{A.6})$$

$$\Delta k_3 = 2k_3 - k_2 - k_4, \quad (\text{A.7})$$

corresponding to the exchange of energy among the involved waves, in order to create a photon of either k_1 or k_4 wavevector.

The equations (A.1)-(A.4) are numerically solved by using Runge-Kutta-Fehlberg method for solving ordinary differential equations. The wavevectors k_n are obtained from COMSOLTM simulations, where the effective refractive indices of the employed waveguides were calculated. Propagation loss of 0.8 dB/cm is assumed based on our previous work on ChG waveguides with

similar processing conditions [28]. An estimated γ of $15.4 \text{ m}^{-1}\text{W}^{-1}$ is assumed, according to a reported n_2 value of $3.71 \times 10^{-18} \text{ m}^2/\text{W}$ [25]. The coupling losses were inferred from measurements similar to those presented in Fig. 5.3. Figure 5.6 shows the measured peak power of FWM#1 signal versus Pump#1 for different input powers with a linear fit, compared to the numerical values obtained from simulations.

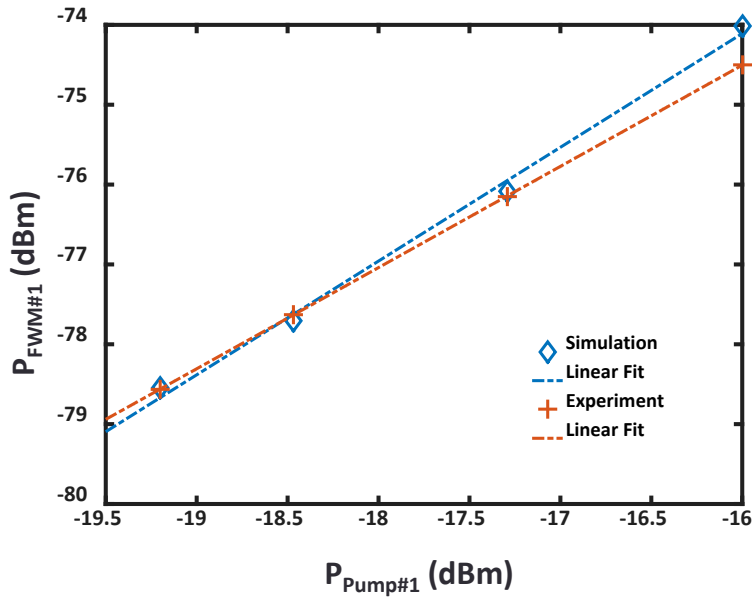


Figure 5.6: Measured peak power of FWM#1 signal vs. Pump#1 power. The result is also compared with the data obtained from simulation.

It should be finally noted that the relatively low conversion efficiency of the FWM experiment is due to the discussed high coupling losses and the normal dispersion of the waveguides. Simulations on the employed waveguides suggest dispersion parameters of ~ -105 and $-220 \text{ ps}/(\text{nm}\cdot\text{km})$ for TE and TM modes, respectively. It is expected that if waveguides with anomalous dispersion [29] are employed higher FWM efficiency, as well as SCG can be achieved. SHG can also be potentially demonstrated by periodically polling [5] or mode-shape modulation [6] of the thin-film LN waveguides. Efforts to make these demonstrations are underway.

5.5 Conclusion

In summary, a heterogeneous platform is demonstrated by integrating $\text{Ge}_{23}\text{Sb}_7\text{S}_{70}$ ChG glass and Si_3N_4 -LN waveguides on Si substrates. Adiabatic optical mode transition from ChG to Si_3N_4 -LN is achieved through carefully designed mode-converting tapers with measured ~ 1.5 dB loss for TE and ~ 1.75 dB loss for TM input polarization in the 1550-nm wavelength range. Wavelength conversion via FWM is measured and compared with theory for the integrated waveguides. The straightforward and high error-tolerant fabrication process combined with the corresponding large nonlinear coefficients of LN and ChG, make this a promising platform for a variety of nonlinear optical applications. Particularly and in conjunction with reports on octave-spanning SCG [30] and SHG in thin-film LN [5], [6], the present work paves the path to demonstration of fully-integrated optical frequency combs stabilized by f -to- $2f$ CEO locking.

Acknowledgements

We thank P. -K. Hsu, S. Fortuna, and K. Han for assistance in ChG deposition and electron-beam lithography.

5.6 References

- [1] R. Soref and J. Lorenzo, "All-silicon active and passive guided-wave components for $\lambda = 1.3$ and $1.6 \mu\text{m}$," *IEEE J. Quant. Elec.*, vol. 22, no. 6, pp. 873–879, 1986.
- [2] B. Jalali and S. Fathpour, "Silicon photonics," *IEEE J. Light. Technol.*, vol. 24, no. 12, pp. 4600–4615, 2006.
- [3] J. Chiles and S. Fathpour, "Silicon photonics beyond silicon-on-insulator," *J. Opt.*, vol. 19, Art. no. 053001, 2017.

- [4] S. Fathpour, “Emerging heterogeneous integrated photonic platforms on silicon,” *Nanophotonics*, vol. 4, no. 1, pp. 143–164, 2015.
- [5] A. Rao, M. Malinowski, A. Honardoost, J. R. Talukder, P. Rabiei, P. Delfyett, and S. Fathpour, “Second-harmonic generation in periodically-poled thin film lithium niobate wafer-bonded on silicon,” *Opt. Express*, vol. 24, no. 26, pp. 29941–29947, 2016.
- [6] A. Rao, J. Chiles, S. Khan, S. Toroghi, M. Malinowski, G. F. Camacho Gonzalez, and S. Fathpour, “Second-harmonic generation in single-mode integrated waveguides based on mode-shape modulation,” *Appl. Phys. Lett.*, vol. 110, Art. no. 111109, 2017.
- [7] X. Guo, C. –L. Zou, and H. X. Tang, “Second-harmonic generation in aluminum nitride microrings with 2500%/W conversion efficiency,” *Optica* vol. 3, pp. 1126–1131, 2016.
- [8] W. H. P. Pernice, C. Xiong, C. Schuck, and H. X. Tang, “High-Q aluminum nitride photonic crystal nanobeam cavities,” *Appl. Phys. Lett.* vol. 100, Art. no. 091105, 2012.
- [9] E. Timurdogan, C. V. Poulton, M. J. Byrd, and M. R. Watts “Electric field-induced second-order nonlinear optical effects in silicon waveguides,” *Nat. Photonics*, vol. 11, pp. 200–206, 2017.
- [10] M. Cazzanelli, F. Bianco, E. Borga1, G. Pucker, M. Ghulinyan, E. Degoli, E. Luppi, V. Vénard, S. Ossicini, D. Modotto, S. Wabnitz, R. Pierobon, and L. Pavesi, “Second-harmonic generation in silicon waveguides strained by silicon nitride,” *Nat. Materials*, vol. 11, pp. 148–154, 2012.
- [11] A. Rao, and S. Fathpour, “Second-harmonic generation in integrated photonics on silicon,” *Phys. Status Solidi A*, 2017.

- [12] A. Driessen, H. J. W. M. Hoekstra, F. C. Blom, F. Horst, G. J. M. Krijnen, J. B. P. van Schoot, P.V. Lambeck, Th. J. A. Popma, and M. B. Diemeer, “Evaluation of polymer based third order nonlinear integrated optics devices,” *Opt. Mater.*, vol. 9, pp. 329–333, 1998.
- [13] B. Esembeson, M. L. Scimeca, T. Michinobu, F. Diederich, and I. Biaggio, “A high-optical quality supramolecular assembly for third-order integrated nonlinear optics,” *Adv. Mater.*, vol. 20, no. 23, pp. 4584–4587, 2008.
- [14] C. Koos, P. Vorreau, T. Vallaitis, P. Dumon, W. Bogaerts, R. Baets, B. Esembeson, I. Biaggio, T. Michinobu, F. Diederich, W. Freude, and J. Leuthold, “All-optical high-speed signal processing with silicon–organic hybrid slot waveguides,” *Nat. Photonics*, vol. 3, pp. 216–219, 2009.
- [15] T. J. Kippenberg, R. Holzwarth, and S. A. Diddams, “Microresonator-based optical frequency combs,” *Science*, vol. 332, no. 6029, pp. 555–559, 2011.
- [16] A. S. Mayer, A. Klenner, A. R. Johnson, K. Luke, M. R. E. Lamont, Y. Okawachi, M. Lipson, A. L. Gaeta, and U. Keller, “Frequency comb offset detection using supercontinuum generation in silicon nitride waveguides,” *Opt. Express*, vol. 23, no. 12, pp. 15440–15451, 2015.
- [17] A. Rao, A. Patil, P. Rabiei, A. Honardoost, R. DeSalvo, A. Paoella, and S. Fathpour, “High-performance and linear thin-film lithium niobate Mach-Zehnder modulators on silicon up to 50 GHz,” *Opt. Lett.*, vol. 41, no. 24, pp. 5700, 2016.
- [18] P. Rabiei, J. Ma, S. Khan, J. Chiles, and S. Fathpour, “Heterogeneous lithium niobate photonics on silicon substrates,” *Opt. Express*, vol. 21, no. 21, pp. 25573–25581, 2013.
- [19] H. Jin, F. M. Liu, P. Xu, J. L. Xia, M. L. Zhong, Y. Yuan, J. W. Zhou, Y. X. Gong, W. Wang, and S. N. Zhu, “On-Chip generation and manipulation of entangled photons based on recon-

- figurable lithium-niobate waveguide circuits,” *Phys. Rev. Lett.*, vol. 113, no. 24, pp. 103601, 2014.
- [20] Y. -K. Jiang and A. Tomita, “The generation of polarization-entangled photon pairs using periodically poled lithium niobate waveguides in a fibre loop,” *J. Phys. B: At. Mol. Opt. Phys.*, vol. 40, Art. no. 437, 2007.
- [21] E. L. Wooten, K. M. Kissa, A. Yi-Yan, E. J. Murphy, D. A. Lafaw, P. F. Hallemeier, D. Maack, D. V. Attanasio, D. J. Fritz, G. J. McBrien, and D. E. Bossi, “A review of lithium niobate modulators for fiber-optic communications systems,” *IEEE J. Quant. Elec.*, vol. 6, no. 1, pp. 69–82 2000.
- [22] J. L. Jackel, C. E. Rice, and J. J. Veselka, “Proton exchange for high-index waveguides in LiNbO_3 ,” *Appl. Phys. Lett.*, vol. 41, no. 7, pp. 607–608, 1982.
- [23] A. Rao, A. Patil, J. Chiles, M. Malinowski, S. Novak, K. Richardson, P. Rabiei, and S. Fathpour, “Heterogeneous microring and Mach-Zehnder modulators based on lithium niobate and chalcogenide glasses on silicon,” *Opt. Express*, vol. 23, no. 17, pp. 22746–22752, 2015.
- [24] L. Chang, M. H. P. Pfeiffer, N. Volet, M. Zervas, J. D. Peters, C. L. Manganelli, E. J. Stanton, Y. Li, T. J. Kippenberg, and J. E. Bowers, “Heterogeneous integration of lithium niobate and silicon nitride waveguides for wafer-scale photonic integrated circuits on silicon,” *Opt. Lett.*, vol. 42, no. 4, pp. 803, 2017.
- [25] J. W. Choi, Z. Han, B. -U. Sohn, G. F. R. Chen, C. Smith, L. C. Kimerling, K. A. Richardson, A. M. Agrawal, D. T. H. Tan, “Nonlinear characterization of GeSbS chalcogenide glass waveguides,” *Sci. Rep.*, vol. 6, Art. no. 39234, 2016.

- [26] K. Ikeda, R. E. Saperstein, N. Alic, and Y. Fainman, “Thermal and Kerr nonlinear properties of plasma-deposited silicon nitride/silicon dioxide waveguides,” *Opt. Express*, vol. 16, no. 17, pp. 12987–12994, 2008.
- [27] B. J. Eggleton, B. Luther-Davis, and K. Richardson, “Chalcogenide photonics,” *Nat. Photonics*, vol. 5, pp. 141–148, 2011.
- [28] J. Chiles, M. Malinowski, A. Rao, S. Novak, K. Richardson, and S. Fathpour, “Low-loss, submicron chalcogenide integrated photonics with chlorine plasma etching,” *Appl. Phys. Lett.*, vol. 106, no. 11, Art. no. 11110, 2015.
- [29] J. -E. Tremblay, Y. -H. Lin, M. N. Sakib, M. Malinowski, S. Novak, P. Qiao, C. Chang-Hasnain, K. Richardson, S. Fathpour, and M. C. Wu, “High-Q and low-loss chalcogenide waveguide for nonlinear supercontinuum generation,” in *Proceedings of IEEE Photonics Conference (IEEE, 2016)*, pp. 158–159.
- [30] M. Malinowski, J. Tremblay, G. Gonzales, A. Rao, S. Khan, P. Hsu, A. Yadav, K. Richardson, P. Delfyett, M. Wu, and S. Fathpour, “Amplified octave-spanning supercontinuum from chalcogenide waveguides for second-harmonic generation,” in *Proceedings of IEEE Photonics Conference (IEEE, 2017)*, pp. 261–262.
- [31] T. Barwicz, and Y. Taira, “Low-cost interfacing of fibers to nanophotonic waveguides: design for fabrication and assembly tolerances,” *IEEE Phot. J.*, vol. 6, no. 4, Art. no. 6600818, 2014.
- [32] T. Alto, K. Solehmainen, M. Harjanne, M. Kappulainen, and P. Heimala, “Low-loss converters between optical silicon waveguides of different sizes and types,” *IEEE Phot. Tech. Lett.* vol. 18, no. 5, pp. 709–711, 2006.
- [33] G. P. Agrawal, “Nonlinear fiber optics,” 4th edition, *Academic Press*, 2017.

CHAPTER 6: FUTURE WORK AND PRELIMINARY RESULTS

Here, the extension of the results presented in the previous chapters are discussed. Some preliminary results are also presented.

6.1 Ultralow-Power Thin-Film Lithium Niobate Electrooptic Modulators

As discussed previously, the technology for standard TFLN EOMs has been matured recently. However, in order to efficiently exploit on-chip electronic drivers for such devices, the switching voltage of the TFLN EOMs are required to be around 1 V or less. This will circumvent the need for additional amplifier circuits and reduce complexity, power consumption, manufacturing cost, and overall footprint of integrated chips.

The half-wave voltage-length product of MZ EOMs, $V_{\pi} \cdot L$, can be expressed as

$$V_{\pi} \cdot L = \frac{\lambda d n_{eff}}{r_{33} n^4 \Gamma} \quad (6.1)$$

where λ denotes the operating wavelength, d represents the gap between the electrodes, n_{eff} and n stand for the waveguide's effective optical refractive index, and refractive index of the EO material (extraordinary refractive index in case of LN EOMs), respectively, r_{33} is the largest EO coefficient of LN, and Γ is the electrical-optical overlap value in the active region of the EOM.

It can be observed in Eq. 6.1, that the $V_{\pi} \cdot L$ has a direct relationship with the gap between the electrodes (d). However, reduction in d is limited by the additional metallic-induced absorption of the optical mode by the EOM's electrodes which contribute to the overall insertion loss of the device and should be minimized as much as possible.

In order to efficiently address this trad-off and reduce the $V_{\pi} \cdot L$, our proposed novel design includes a thin layer of SiO_2 , as depicted in Fig. 6.1.

As evident from Fig. 6.2(a), in the standard structure (Fig. 6.1(a)), as the gap is reduced

from the typical $6 \mu\text{m}$ to $2 \mu\text{m}$, the tails of the optical TE mode get closer to the metallic electrodes and the absorption starts to increase dramatically. Whereas, in the proposed structure depicted in Fig. 6.1(b) the thin insulating layer allows for the gap to be reduced to values as low as $2 \mu\text{m}$ (see Fig. 6.2(b)). However another trade-off that arises here is the EO overlap, Γ , value which decreases by adding the thin oxide layer. The simulation results for the aforementioned trade-offs are summarized in Table 6.1.

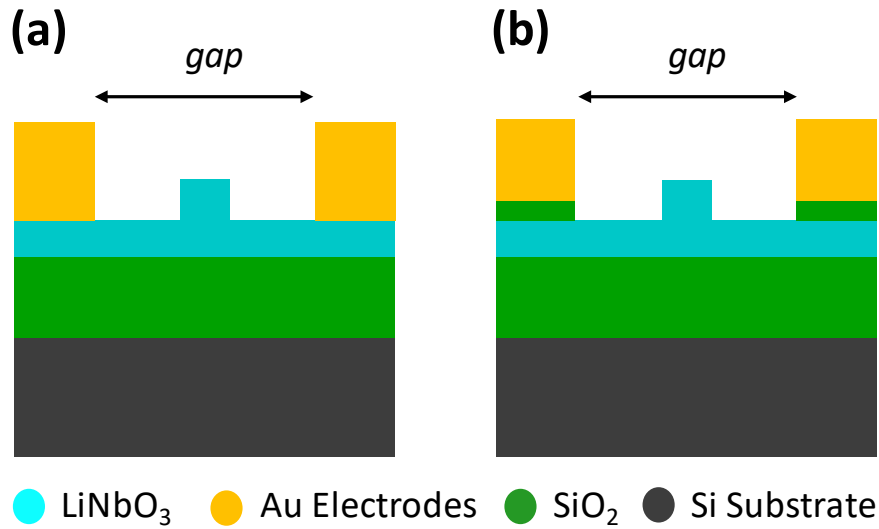


Figure 6.1: (a) Standard TFLN MZ EOM structure; (b) Proposed novel structure for ultralow-power TFLN MZ EOMs.

Table 6.1: Simulated results of Γ and $V_{\pi} \cdot L$ for the structure of Figs. 6.1 and 6.2.

Gap [μm]	Γ (Fig. 6.2(b))	$V_{\pi} \cdot L$ (Fig. 6.2(b)) [V.cm]	Γ (Fig. 6.2(a))	$V_{\pi} \cdot L$ (Fig. 6.2(a)) [V.cm]
1.5	0.47	1.24	0.83	0.72
2	0.51	1.53	0.81	0.97
3	0.57	2.08	0.80	1.47
4	0.59	2.67	0.78	2.01
5	0.6	3.29	0.76	2.57
6	0.6	3.93	0.74	3.19

As mentioned, metallic induced optical absorption is another important criteria for EOMs. Table 6.2 summarizes the difference between structures of Figs. 6.1 and 6.2 in this regard.

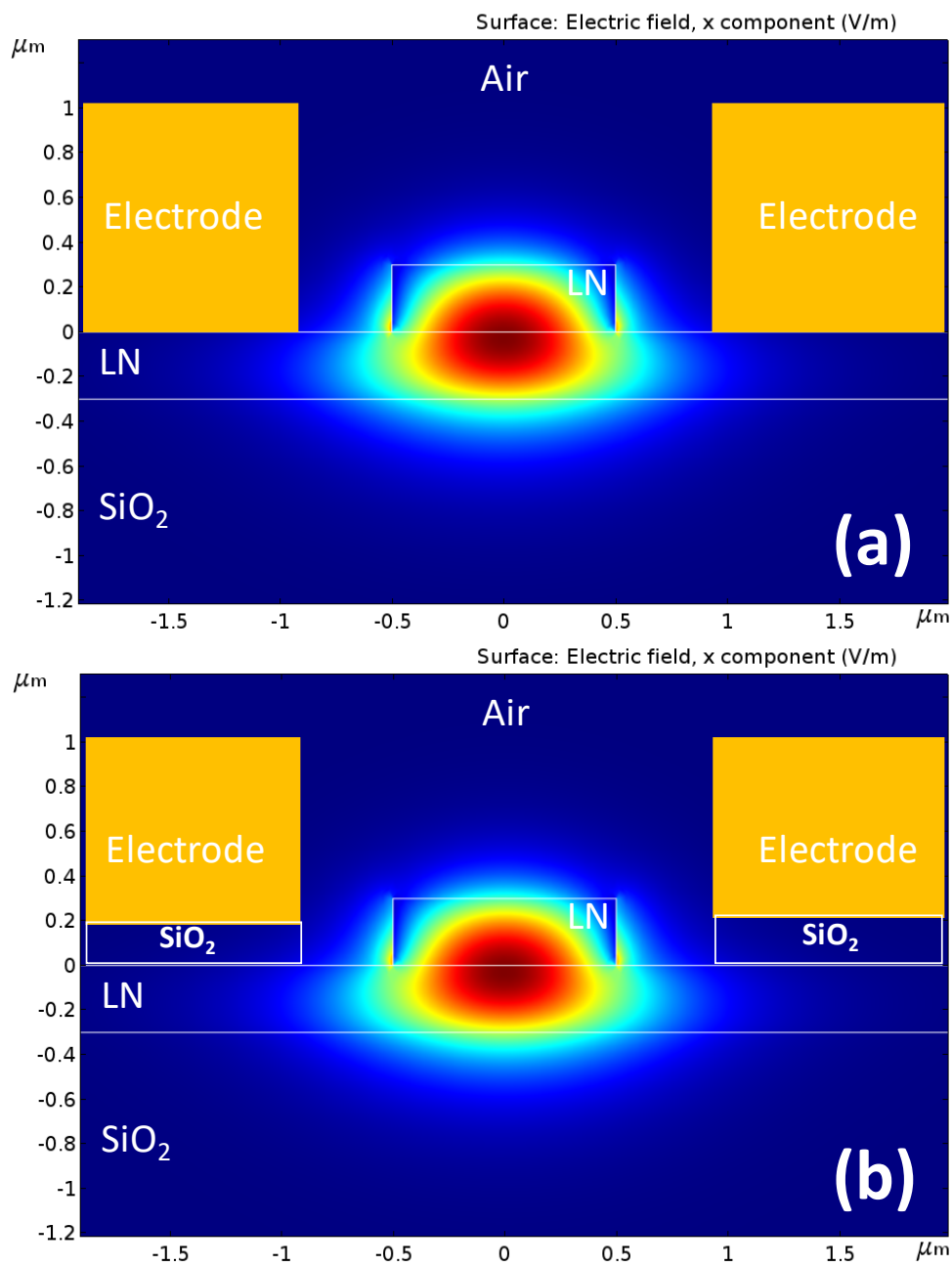


Figure 6.2: (a) Standard TFLN MZ EOM structure; (b) Proposed novel structure for ultralow-power TFLN MZ EOMs. The optical mode is TE polarized.

Considering the above mentioned trade-offs, a chip with multiple variations for gap, for both structures of Figs. 6.1, is designed and fabricated, as presented in Fig. 6.3(a). Two types of

devices for low-, and high-frequency operation are fabricated as shown in Figs. 6.3(b) and 6.3(c), respectively.

Table 6.2: Simulated results of metallic-induced optical absorption for the structure of Figs. 6.1 and 6.2.

Gap [μm]	Loss (Fig. 6.2(b)) [dB/cm]	Loss (Fig. 6.2(b)) [dB/cm]
1.5	6.5	2300
2	1.2	490
3	0.07	31
4	0	2.1
5	0	0.1

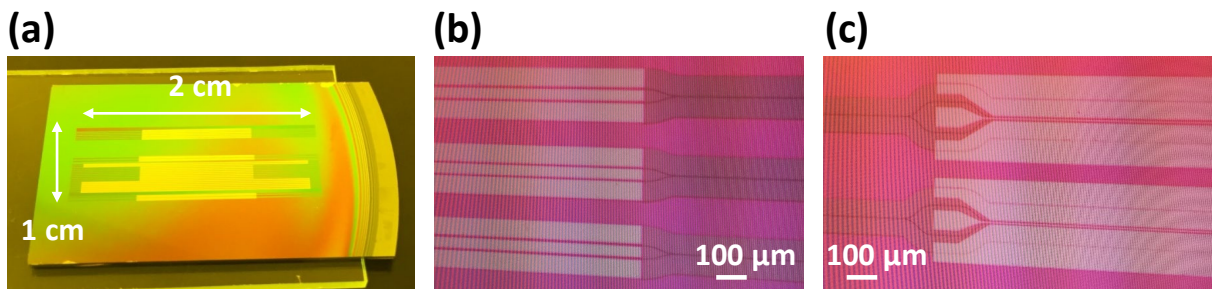


Figure 6.3: (a) Image of the fabricated chip; Microimages of the devices for (b) low-, and (c) high-frequency operation. The high-frequency design poses narrower middle electrode.

The chip is currently laser diced for input/output coupling and measurements are underway, as shown in Fig. 6.4.

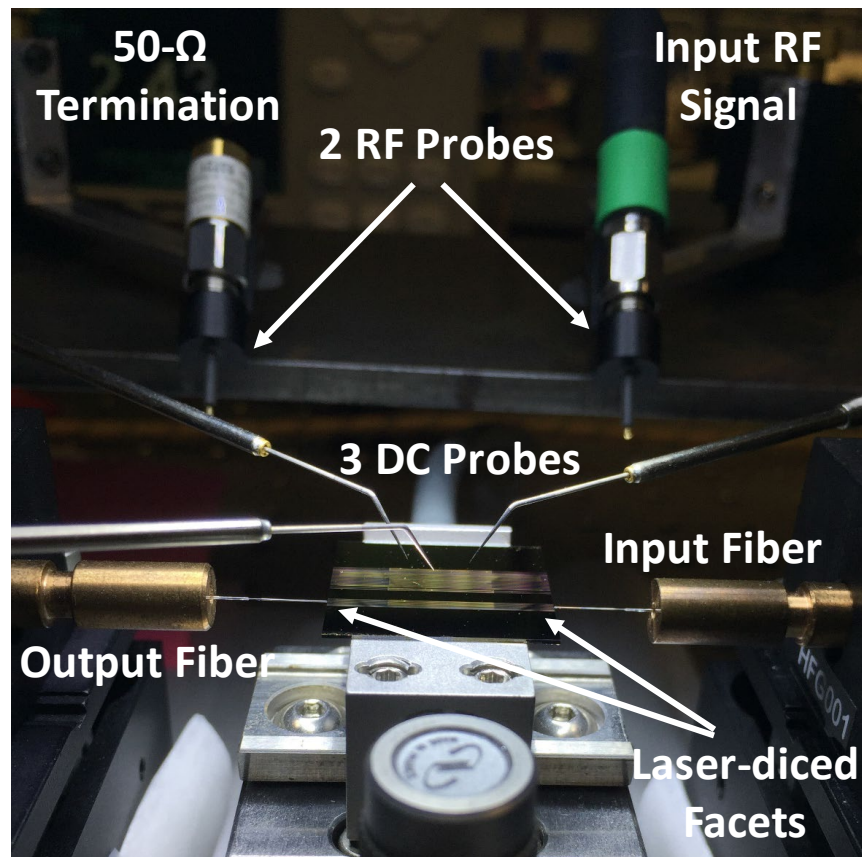


Figure 6.4: (a) Experimental setup for low-, and high-frequency measurements.

6.2 Coherent Modulation in Thin-Film Lithium Niobate Electrooptic Modulators

With achieving high levels of maturity for TFLN EOMs discussed in the previous section, the next step is to demonstrate higher modulation schemes, such as Quadrature Phase-Shift Keying (QPSK), which is required for coherent communication in advanced optical networks.

In a QPSK modulator, transmission of phase information is utilized instead of amplitude modulation. In advanced optical communication systems, this results in lower transmitted optical power, and signal-to-noise ratio requirements. QPSK modulation principle and the schematic of a single QPSK modulator are depicted in Fig. 6.5 [1]. 2 nested Mach-Zehnder modulators (MZM) followed by a phase modulator (PM) are required in order to produce the $\pi/2$ phase shift.

While this has been previously reported for bulk LN [1] and all-Si modulators [2], to the best of our knowledge, the work presented here is the first demonstration of such devices on TFLN platform.

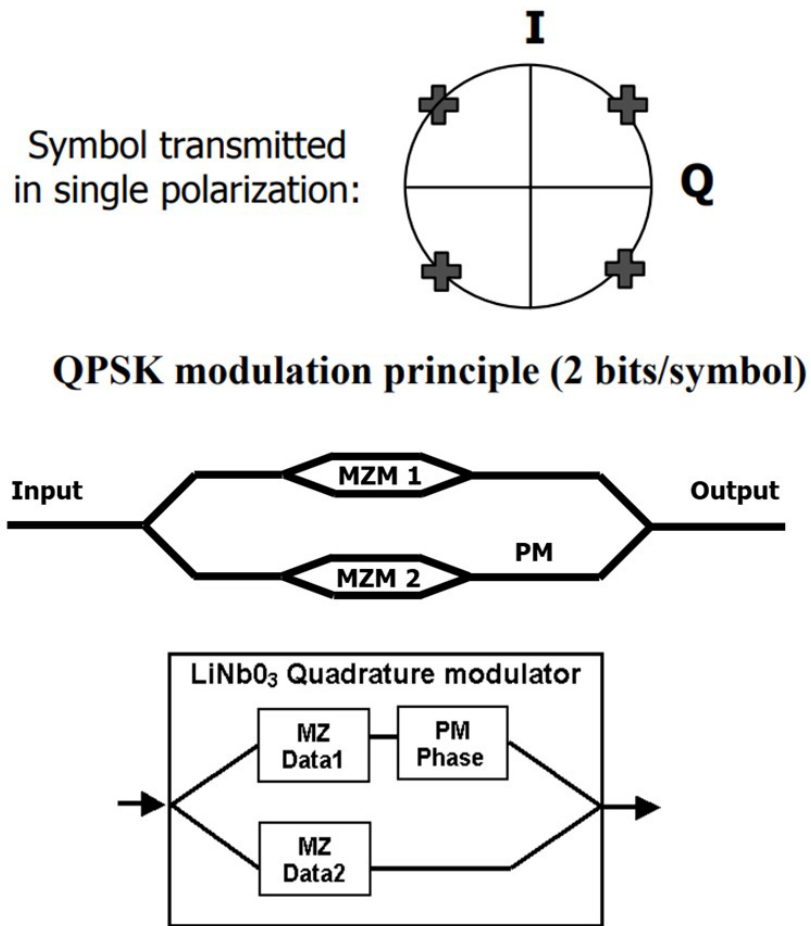


Figure 6.5: Operation principle of a QPSK modulator and its schematic diagram.

A chip for the experimental demonstration is designed and fabricated, as presented in Fig. 6.6. The chip is laser diced for input/output coupling and the measurement are underway. Our preliminary results show high values of 22 dB for low-frequency ER in 7-mm-long devices, and a low $V_{\pi} \cdot L$ value of about 2.6 V.cm for 5-mm-long EOMs. The preliminary results are sum-

marized in Fig. 6.6.

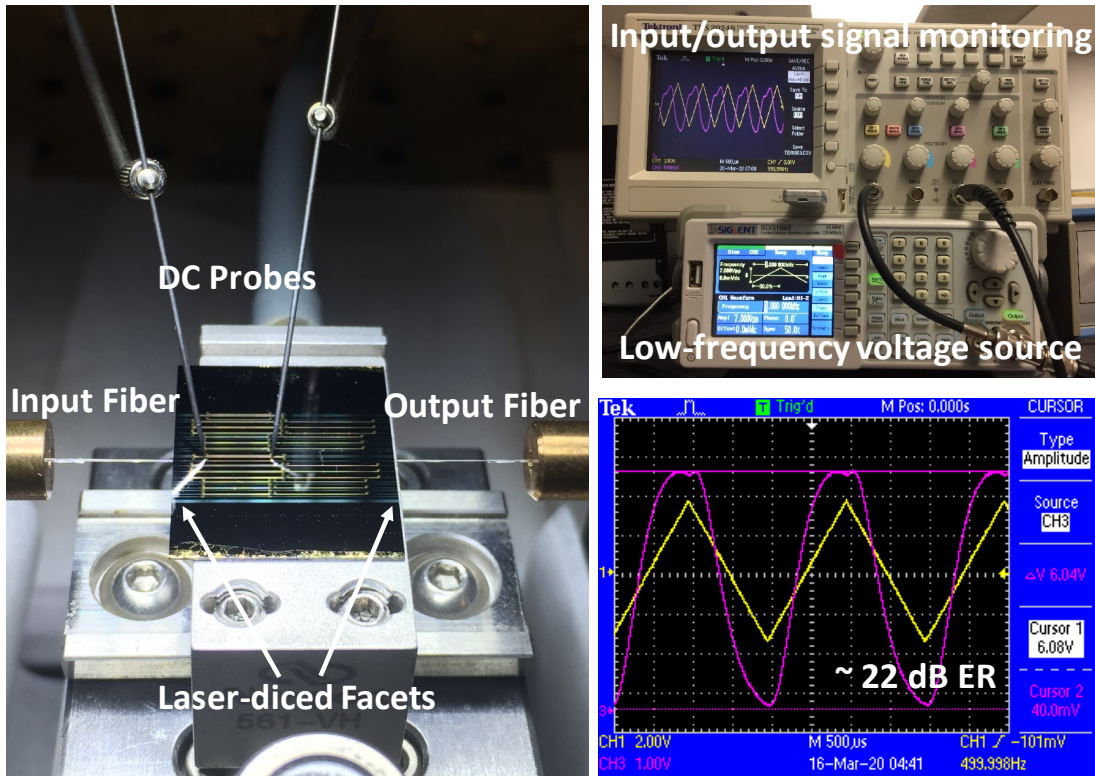


Figure 6.6: Experimental setup and preliminary measurement results.

6.3 Cascaded Second-, and Third-Order Optical Nonlinearities on a Single Chip

As an extension of the work discussed in Chapter 5, we have recently reported on design of such high-performance cascaded nonlinearities in order to demonstrate both SCG and SHG on a single Si chip. The simulation results suggest over over 1.25 octave spanning SCG and an adiabatic optical mode transition between the two sections on the chip, as depicted in Fig. 6.7 [3].

For experimental demonstration, a fully-integrated chip is designed and fabricated, as shown in Fig. 6.8. The chip is laser diced for input/output coupling and the measurement are currently underway.

Next step for applications such as on-chip self-referenced optical frequency comb gen-

eration, as discussed in Chapter 5, passive waveguide filters or other means of filtering can be employed in order to achieve f -to- $2f$ referencing, as depicted in Fig. 6.9. Moreover, EOMs can also be utilized in future work in order to attain tunability of phase delays on the same chip [4].

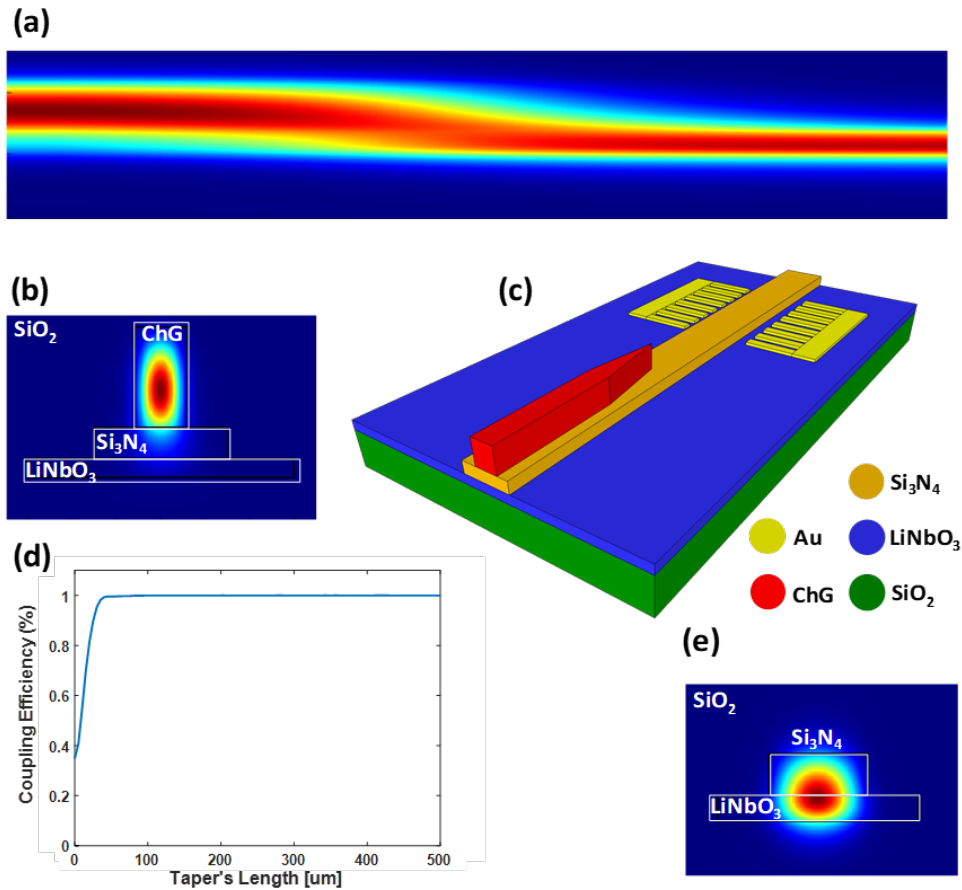


Figure 6.7: (a) Quasi-TE optical mode transition from ChG waveguides (left) to TFLN waveguides (right) through carefully designed mode-converting tapers; (b) Fundamental optical mode distribution in ChG waveguide for SCG; (c) 3-D schematic of the fully-integrated chip; (d) Simulation results for adiabatic mode transition for tapers with length above $100 \mu\text{m}$; (e) Fundamental optical mode distribution in TFLN waveguide (rib-loaded with SiN) for SHG. Reproduced with permission from [3].

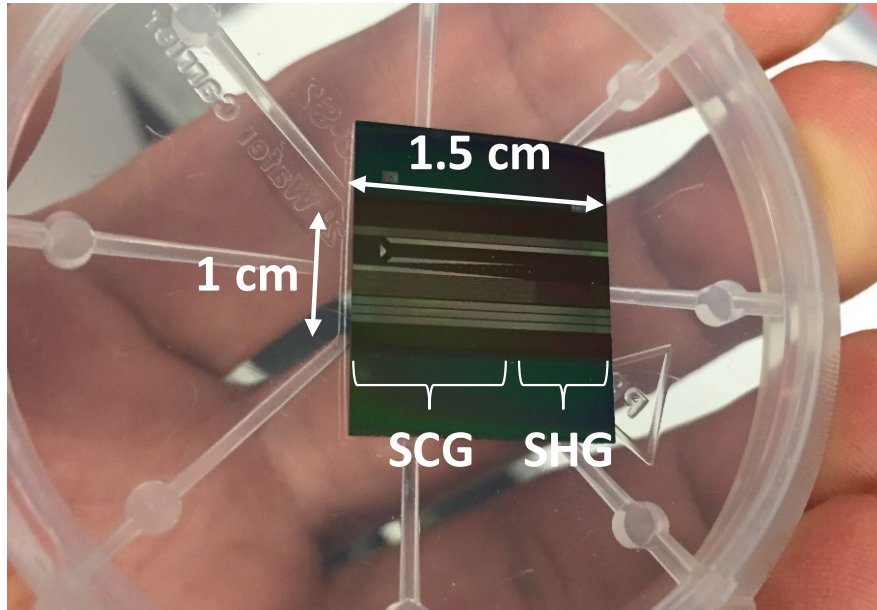


Figure 6.8: Image of the fabricated chip.

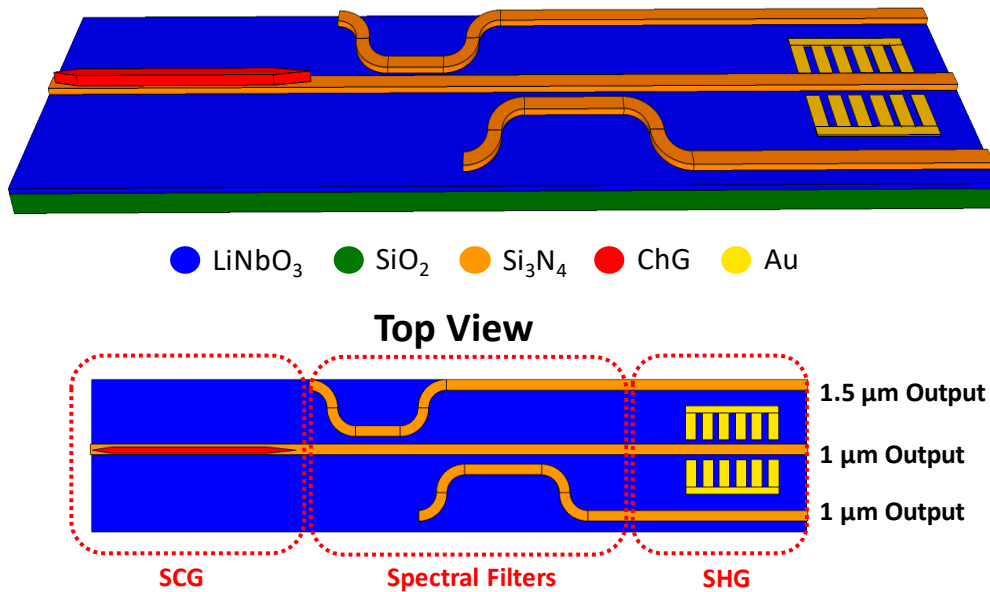


Figure 6.9: Conceptual 3-D schematic of a fully-integrated chip for frequency-stabilized optical comb generation application. [4]

6.4 Foundry-Compatible Integration of Thin-Film Lithium Niobate with Silicon Photonics

As discussed in the previous sections, the technology for TFLN devices has been matured recently. However the LN itself is not Si-foundry compatible yet. Hence, in order to exploit benefits of the mature Si photonic industry, namely its standard low-cost foundry-compatible processing and tightly-confined waveguides, a novel integration scheme is proposed in which the thin films of LN, wafer-scale or individual dies, are integrated at back end of the line [5]. A short description can also be found in Chapter 2, Section 2.2.2 (see Fig. 2.5).

It should be noted that the proposed scheme can be applied to a host of materials as summarized in Fig. 6.10(a). Figure 6.10(b) depicts an example of such integration by providing design dimensions.

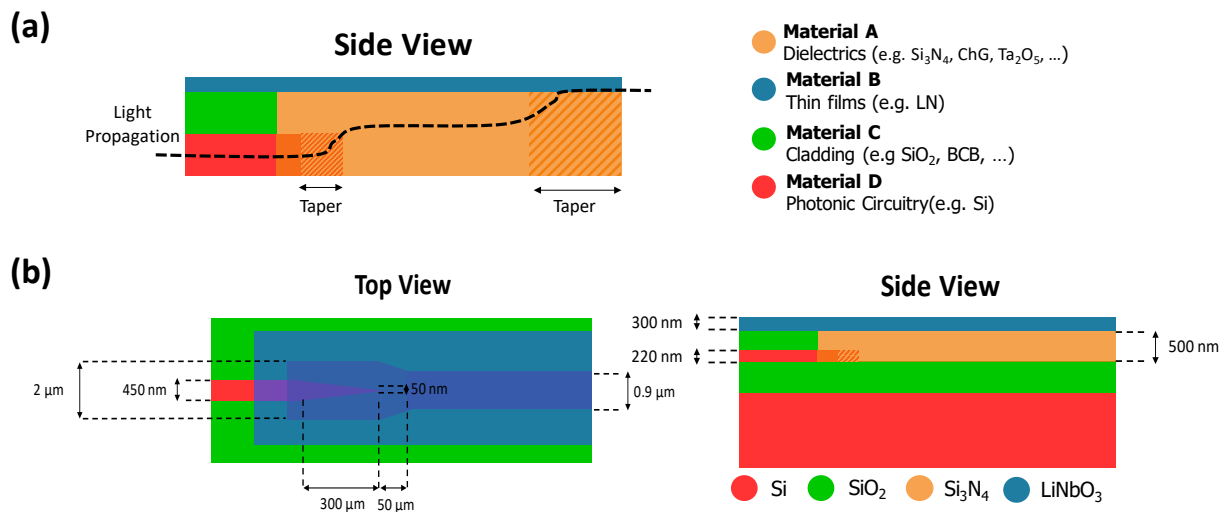


Figure 6.10: (a) Schematic of the proposed structure for thin-film integration. As presented in (a), a host of different materials can be used in this approach; (b) An example of designed dimension for TFLN integration with standard Si photonic waveguides. [5]

As an extension of high-performance TFLN EOMs discussed in this dissertation, a fully-integrated chip including laser source and detection components are presented in Figs. 6.11. The intermediate SiN layer serves as an adiabatic mode converter as well as a rib, in order to efficiently transfer the optical mode from standard Si-on-insulator (SOI) waveguides into LN region. While

the schematic here represents a MZ EOM, this approach can be applied to other TFLN devices such as PPLN for nonlinear optical applications, and other device for quantum optics, as discussed in Chapter 2.

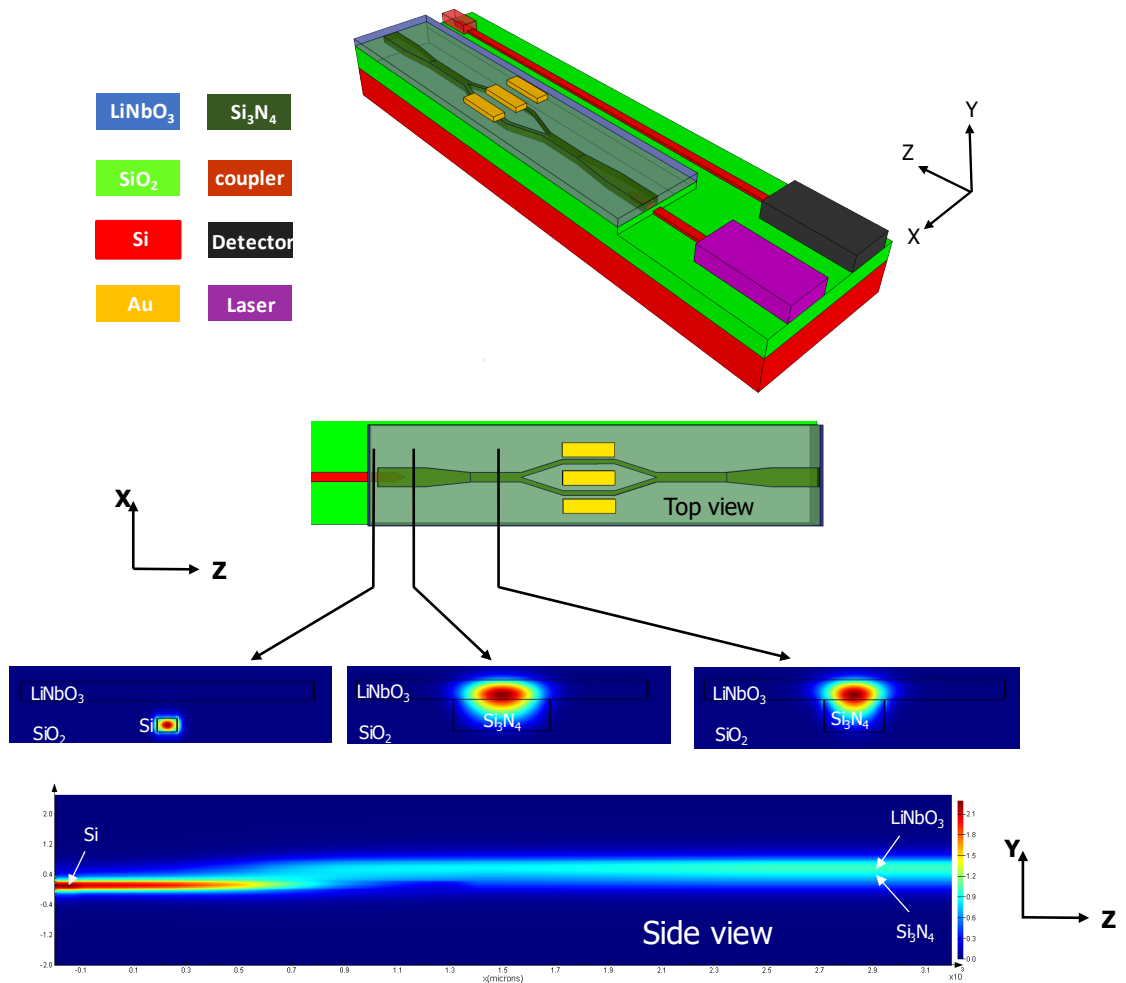


Figure 6.11: 3-D schematic of a conceptual fully-integrated TFLN EOM with Si photonic circuitry including on-chip laser source and detection components. The simulated optical mode is provided at different positions of the circuit. An adiabatic mode transition from Si waveguide (left) to TFLN region (right) is shown as well. [5]

The fabrication steps for this scheme are summarized in Figs. 6.12–6.14. While direct bonding with SiO₂ is preferred over bonding via adhesive polymers, such as BCB, as discussed in Chapter 2, nevertheless, either materials can be employed in the proposed scheme.

Foundry processing

Back end of line processing



Figure 6.12: Summary of the fabrication steps using TFLN-on-Si wafers [5]

Foundry processing

Back end of line processing

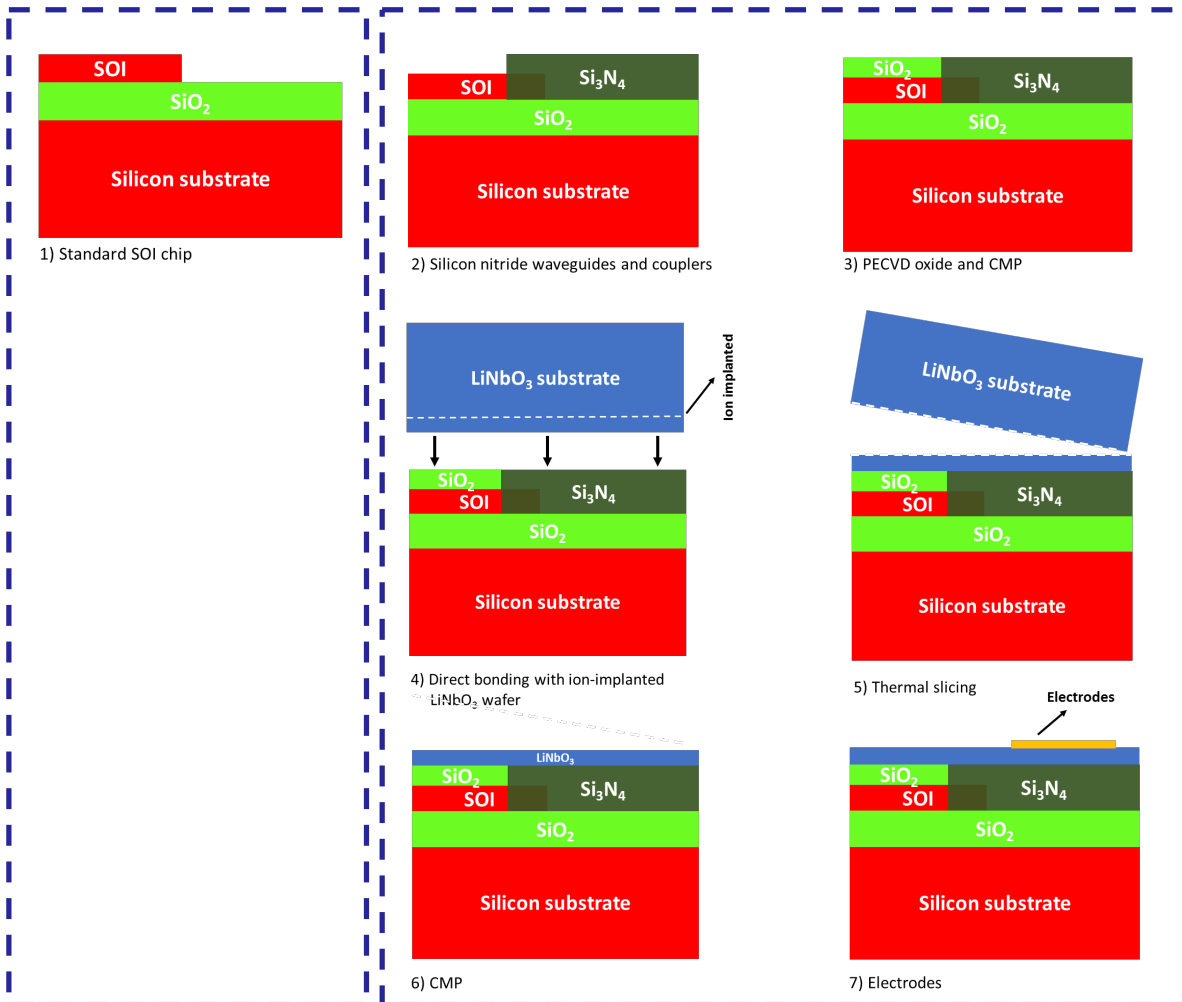


Figure 6.13: Summary of the fabrication steps using TFLN-on-LN (LNOI) wafers [5]

Foundry processing

Back end of line processing

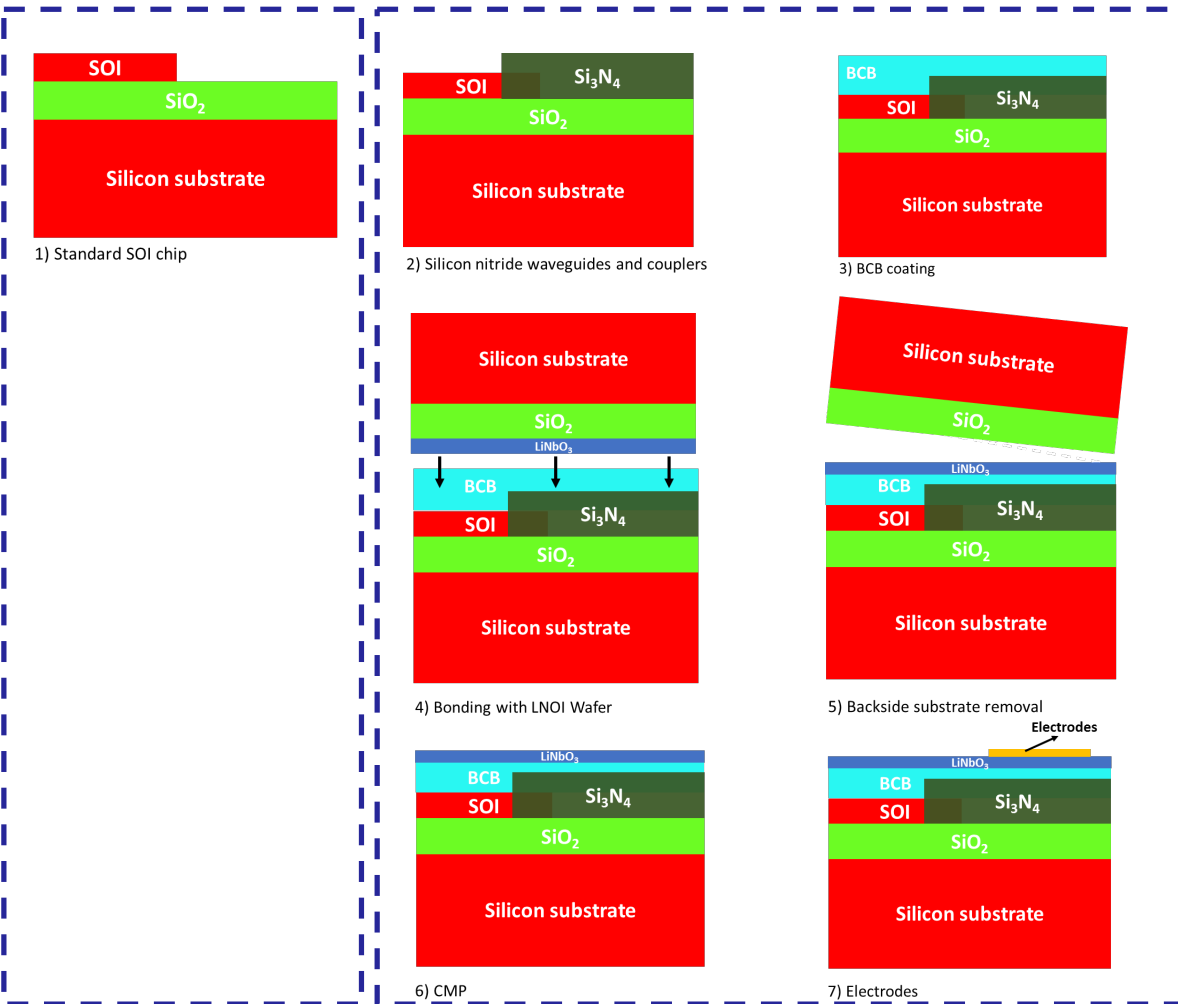


Figure 6.14: Summary of the fabrication steps using TFLN-on-Si wafers and BCB bonding [5]

6.5 Summary

Various contribution to the thin-film LN technology have been covered in this dissertation for electro-, and nonlinear-optic applications, as outlined in Chapter 1. In the second Chapter, a comprehensive review is provided on TFLN technology history, its state of the art, and the strides made toward ultracompact LN devices for electro-, nonlinear-, and quantum-optic applications.

A general transmission-line model is developed in Chapter 3 in order to efficiently design ultracompact EOMs and accurately predict their high-speed performance. The accuracy of the model has been verified by comparison with experimental results. Chapter 4 presents detailed design techniques for radio-frequency and optical parameters of TFLN EOMs, and novel optimized structures are reported in order to achieve subterahertz BW in such devices. This paves the path towards utilization of ultracompact EOMs in advanced communication systems.

In order to co-integrate multiple optical nonlinearities on a single Si chip, an efficient platform is presented in Chapter 5. In this work, by employing carefully-designed adiabatic optical mode converters, ChG and TFLN waveguides, possessing large third-, and second-order optical nonlinearity, respectively, are monolithically integrated on a Si chip for the first time. As a proof of concept, nonlinear four-wave-mixing experiment is successfully demonstrated on the same chip.

In Chapter 6, extension of the works discussed in Chapters 2–5 with some preliminary result are presented for future work. A novel design is proposed and fabricated for ultracompact TFLN EOMs suitable for applications such as optical interconnects. Coherent modulation is also pursued on the TFLN platform and QPSK EOMs are fabricated. For applications such as on-chip self-stabilized frequency comb generation, cascaded integration of ChG and TFLN waveguides are pursued in order to achieve above an octave SCG and efficient SHG on a single Si chip. Also, an innovative platform is proposed in order to efficiently integrate TFLN with Si photonic circuitry suitable for large-scale, low-cost, and foundry-compatible production of integrated photonic circuits.

6.6 References

- [1] A. Kaplan, K. Achiam, A. Greenblatt, G. Harston, and P. S. Cho, “LiNbO₃ Integrated Optical QPSK Modulator and Coherent Receiver,” *Proc. Eur. Conf. Integrated Optics (ECIO)*, pp. 79–82, 2003.
- [2] P. Dong, L. Chen, C. Xie, L. L. Buhl, and Y. -K. Chen, “50-Gb/s silicon quadrature phase-shift keying modulator,” *Opt. Express*, vol. 20, no. 19, pp. 21181–21186, 2012.
- [3] G. F. Camacho Gonzalez, M. Malinowski, A. Honardoost, and S. Fathpour, “Design of a hybrid chalcogenide-glass on lithium-niobate waveguide structure for high-performance cascaded third- and second-order optical nonlinearities,” *Applied Optics*, vol. 58, no. 13, pp. D1–D6, 2019.
- [4] S. Fathpour, “Heterogeneous Nonlinear Integrated Photonics,” *IEEE Journal of Quantum Electronics*, vol. 54, no. 6, pp. 1–16, 2018.
- [5] S. Fathpour, A. Honardoost, and S. Khan, “Thin-film integration compatible with silicon photonics foundry production,” *US Patent App. 15/932,800*, 2018.

APPENDIX A: COPYRIGHT PERMISSIONS



RightsLink®



Home



Help



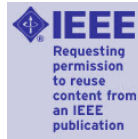
Email Support



Sign in



Create Account



High-Speed Modeling of Ultracompact Electrooptic Modulators

Author: Amirmahdi Honardoost

Publication: Lightwave Technology, IEEE/OSA Journal of

Publisher: IEEE

Date: 15 Dec.15, 2018

Copyright © 2018, IEEE

Thesis / Dissertation Reuse

The IEEE does not require individuals working on a thesis to obtain a formal reuse license, however, you may print out this statement to be used as a permission grant:

Requirements to be followed when using any portion (e.g., figure, graph, table, or textual material) of an IEEE copyrighted paper in a thesis:

- 1) In the case of textual material (e.g., using short quotes or referring to the work within these papers) users must give full credit to the original source (author, paper, publication) followed by the IEEE copyright line © 2011 IEEE.
- 2) In the case of illustrations or tabular material, we require that the copyright line © [Year of original publication] IEEE appear prominently with each reprinted figure and/or table.
- 3) If a substantial portion of the original paper is to be used, and if you are not the senior author, also obtain the senior author's approval.

Requirements to be followed when using an entire IEEE copyrighted paper in a thesis:

- 1) The following IEEE copyright/ credit notice should be placed prominently in the references: © [year of original publication] IEEE. Reprinted, with permission, from [author names, paper title, IEEE publication title, and month/year of publication]
- 2) Only the accepted version of an IEEE copyrighted paper can be used when posting the paper or your thesis online.
- 3) In placing the thesis on the author's university website, please display the following message in a prominent place on the website: In reference to IEEE copyrighted material which is used with permission in this thesis, the IEEE does not endorse any of [university/educational entity's name goes here]'s products or services. Internal or personal use of this material is permitted. If interested in reprinting/republishing IEEE copyrighted material for advertising or promotional purposes or for creating new collective works for resale or redistribution, please go to http://www.ieee.org/publications_standards/publications/rights/rights_link.html to learn how to obtain a License from RightsLink.

If applicable, University Microfilms and/or ProQuest Library, or the Archives of Canada may supply single copies of the dissertation.

BACK

CLOSE



RightsLink®



Home



Help



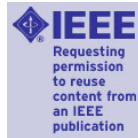
Email Support



Sign in



Create Account



Cascaded Integration of Optical Waveguides With Third-Order Nonlinearity With Lithium Niobate Waveguides on Silicon Substrates

Author: Amirmahdi Honardoost

Publication: IEEE Photonics Journal

Publisher: IEEE

Date: June 2018

Copyright © 2018, IEEE

Thesis / Dissertation Reuse

The IEEE does not require individuals working on a thesis to obtain a formal reuse license, however, you may print out this statement to be used as a permission grant:

Requirements to be followed when using any portion (e.g., figure, graph, table, or textual material) of an IEEE copyrighted paper in a thesis:

- 1) In the case of textual material (e.g., using short quotes or referring to the work within these papers) users must give full credit to the original source (author, paper, publication) followed by the IEEE copyright line © 2011 IEEE.
- 2) In the case of illustrations or tabular material, we require that the copyright line © [Year of original publication] IEEE appear prominently with each reprinted figure and/or table.
- 3) If a substantial portion of the original paper is to be used, and if you are not the senior author, also obtain the senior author's approval.

Requirements to be followed when using an entire IEEE copyrighted paper in a thesis:

- 1) The following IEEE copyright/ credit notice should be placed prominently in the references: © [year of original publication] IEEE. Reprinted, with permission, from [author names, paper title, IEEE publication title, and month/year of publication]
- 2) Only the accepted version of an IEEE copyrighted paper can be used when posting the paper or your thesis online.
- 3) In placing the thesis on the author's university website, please display the following message in a prominent place on the website: In reference to IEEE copyrighted material which is used with permission in this thesis, the IEEE does not endorse any of [university/educational entity's name goes here]'s products or services. Internal or personal use of this material is permitted. If interested in reprinting/republishing IEEE copyrighted material for advertising or promotional purposes or for creating new collective works for resale or redistribution, please go to http://www.ieee.org/publications_standards/publications/rights/rights_link.html to learn how to obtain a License from RightsLink.

If applicable, University Microfilms and/or ProQuest Library, or the Archives of Canada may supply single copies of the dissertation.

BACK

CLOSE

RE: Reprint permission for PhD dissertation

pubscopyright <copyright@osa.org>

Thu 4/16/2020 3:31 PM

To: Amirmahdi Honardoost <honardoost@Knights.ucf.edu>; pubscopyright <copyright@osa.org>

Dear Amirmahdi Honardoost,

Thank you for contacting The Optical Society.

For the use of material from [1] Amirmahdi Honardoost, Farzaneh Arab Juneghani, Reza Safian, and Sasan Fathpour, "Towards subterahertz bandwidth ultracompact lithium niobate electrooptic modulators," Opt. Express 27, 6495-6501 (2019):

Because you are the author of the source paper from which you wish to reproduce material, OSA considers your requested use of its copyrighted materials to be permissible within the author rights granted in the Copyright Transfer Agreement submitted by the requester on acceptance for publication of his/her manuscript. It is requested that a complete citation of the original material be included in any publication. This permission assumes that the material was not reproduced from another source when published in the original publication.

For the use of material from [2] Guillermo Fernando Camacho Gonzalez, Marcin Malinowski, Amirmahdi Honardoost, and Sasan Fathpour, "Design of a hybrid chalcogenide-glass on lithium-niobate waveguide structure for high-performance cascaded third- and second-order optical nonlinearities," Appl. Opt. 58, D1-D6 (2019):

Because you are the author of the source paper from which you wish to reproduce material, OSA considers your requested use of its copyrighted materials to be permissible within the author rights granted in the Copyright Transfer Agreement submitted by the requester on acceptance for publication of his/her manuscript. If the entire article is being included, it is requested that the **Author Accepted Manuscript** (or preprint) version be the version included within the thesis and that a complete citation of the original material be included in any publication. This permission assumes that the material was not reproduced from another source when published in the original publication.

The **Author Accepted Manuscript** version is the preprint version of the article that was accepted for publication but not yet prepared and/or formatted by The Optical Society or its vendors.

While your publisher should be able to provide additional guidance, OSA prefers the below citation formats:

For citations in figure captions:

[Reprinted/Adapted] with permission from [ref #] © The Optical Society. (Please include the full citation in your reference list)

For images without captions:

Journal Vol. #, first page (year published) An example: Appl. Opt. 58, D1 (2019)

Please let me know if you have any questions.

Kind Regards,

Rebecca Robinson

Rebecca Robinson
April 16, 2020
Authorized Agent, The Optical Society

The Optical Society (OSA)

2010 Massachusetts Ave., NW
Washington, DC 20036 USA
www.osa.org

Reflecting a Century of Innovation

